

PhD thesis

In Vivo Optical Imaging of Fluorescent Markers for
Detection and Guided Resection of Cancer

Arjen Bogaards

Printing of this thesis was financially supported by:

- Steba Biotech N.V., The Hague, The Netherlands
- Medlight S.A., Ecublens, Switzerland
- Biolitec AG, Jena, Germany
- Photonamic GmbH & Co. KG, Wedel, Germany
- ART Advanced Research Technologies Inc., Saint-Laurent, PQ, Canada

Copyright: © 2006

All rights reserved. No part of this thesis may be reproduced, stored in a retrieval system of any nature, or transmitted in any form by any means, electronic, mechanical, photocopying, recording or otherwise, included a complete or partial transcription, without the permission of the copyright owners.

In vivo Optical Imaging of Fluorescent Markers for Detection and Guided Resection of Cancer

Proefschrift

ter verkrijging van de graad van doctor aan de
Erasmus Universiteit Rotterdam
op gezag van de rector magnificus

Prof.dr. S.W.J. Lamberts

en volgens besluit van het College voor Promoties.

De openbare verdediging zal plaatsvinden op
donderdag 7 september 2006 om 11:00 uur

door

Arjen Bogaards

geboren te Goes

Promotiecommissie

Promotores:

Prof.dr. P.C. Levendag

Prof.dr. B.C. Wilson

Overige leden:

Prof.dr. B.J.M. Heijmen

Prof.dr. A.G.J.M. van Leeuwen

Dr.ir. G.W. Puppels

Dr. L. Lilge

Dr.ing. G.C. van Rhoon

Copromotor:

Dr.ir. H.J.C.M. Sterenberg

Paranimfen

M.C.M. Grimbergen
E.H. Bogaards

Voor Tim en Eva

Table of Contents

Chapter 1 Introduction	11
Chapter 2 Double ratio fluorescence imaging for the detection of early superficial cancers: design, construction and performance of a clinical prototype <i>Rev Sci Instrum.</i> (2001) 72: 3956-3961	19
Chapter 3 Localization and staging of cervical intraepithelial neoplasia using double ratio fluorescence imaging <i>J Biomed Opt.</i> (2002) 7:215-20.	31
Chapter 4 Increased brain tumor resection using fluorescence image guidance in a preclinical model <i>Lasers Surg Med.</i> (2004) 35:181-90	43
Chapter 5 Fluorescence image-guided brain tumour resection with adjuvant metronomic photodynamic therapy: pre-clinical model and technology development <i>Photochem Photobiol Sci.</i> (2004) 4: 438-42	59
Chapter 6 <i>In vivo</i> quantification of fluorescent molecular markers in real-time: a modeling study to evaluate the performance of five existing methods <i>J Biomed Opt.</i> , submitted 2006	69
Chapter 7 <i>In vivo</i> quantification of fluorescent molecular markers by ratio imaging for real-time diagnostic screening and image-guided surgery <i>Manuscript in progress</i>	85
Chapter 8 Summary / Samenvating	99
Chapter 9 General Discussion	107
Curriculum Vitae	111
Scientific Output	113
Acknowledgements / Dankwoord <i>This thesis is a compilation of published papers that were reformatted here; however their original content was not changed.</i>	117

Chapter 1

Introduction



Background

“Early detection (of cancer) is and will continue to be the single best way to significantly improve therapeutic outcomes” (1). This, however, is a major challenge. Many cancerous tissues and especially their early stages can be difficult to visualize for a physician because their appearance under white light illumination can be similar to that of normal tissues. Conversely, advanced cancers which are visible under white light illumination can have margins that are invisible due to tumor cells that invade into the surrounding normal tissues. This can hamper detection and complete surgical resection, both affecting therapeutic outcomes. Hence, there is a need to better visualize cancers and their extent.

In vivo optical imaging of fluorescence

One approach that can enhance the capability of the physician to visualize early cancers is the administration of a tumor-selective fluorescent marker. The tissue can then be illuminated with light of an appropriate wavelength to excite the marker and the resulting fluorescence can be detected using a sensitive camera.

Fluorescent markers, on a molecular level (as shown in the energy level diagram in Fig. 1), can absorb certain wavelengths of light and thereby excite one of two electrons that are ‘paired’ (i.e. electrons with opposite spin orientation) from the ground singlet electronic state (S_0) to the first or second singlet electronic state (S_1 , S_2) (2). Generally, following excitation the electron non-radiatively decays to the lowest vibrational energy level ($v = 0, 1, 2$, etc.) of the first singlet electronic state, a process that is called internal conversion. In tissues, most commonly, fluorescence is the emission of light when the excited electron in the first singlet state, returns to the ground singlet state.

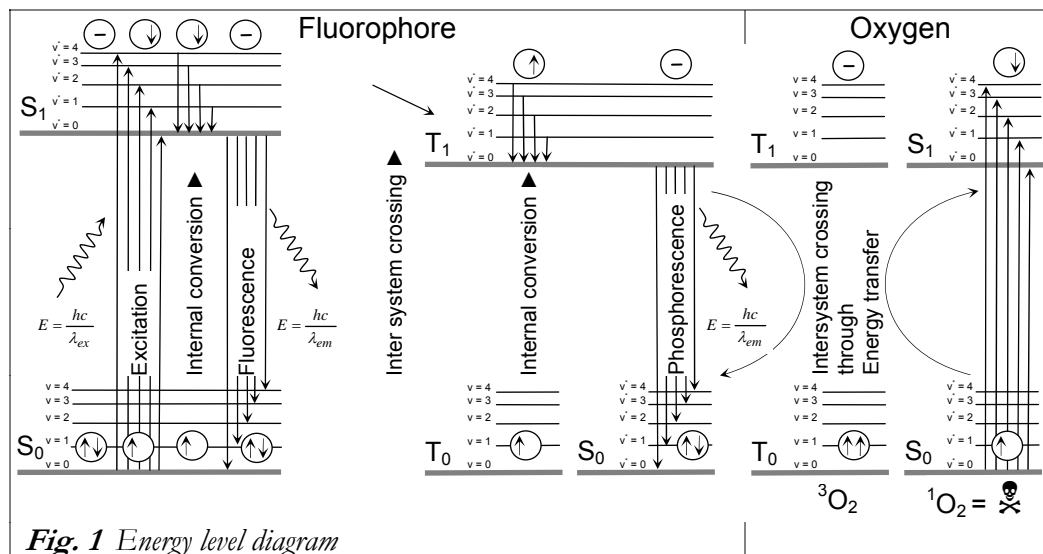


Fig. 1 Energy level diagram

Absorption takes place in the order of 10^{-15} s, internal conversion takes in the order of 10^{-12} s and the average period of time an electron remains in the excited state before it decays and emits fluorescence, i.e. the fluorescence lifetime, is around 10^{-8} s. As a result of these time scales absorption takes place from a single equilibrated ground electronic and

vibrational state to various excited electronic and vibrational states. On the other hand fluorescence takes place from a single equilibrated excited electronic and vibrational state to the various vibrational states of the ground singlet electronic state. Hence, the absorption spectra is indicative of the vibrational levels of the excited electronic state and the fluorescence emission is indicative of the vibrational levels in the ground electronic singlet state, as illustrated in Fig. 2 that shows both absorption and emission spectra for the fluorescent marker Protoporphyrin IX.

Fluorescence is not the only de-excitation mechanism for a molecule in the excited singlet state. Instead, it may decay non-radiatively, or may undergo intersystem crossing. In the latter case, the spin orientation of the excited electron in the first singlet state flips to the same orientation as the paired electron in the ground state so that the molecule undergoes conversion to the first triplet electronic state, T_1 . Emission of light due to transition from T_1 to the ground singlet state S_0 is called phosphorescence. This has a longer wavelength compared to fluorescence due to a loss of energy associated with intersystem crossing. Because transition from T_1 to the ground singlet state S_0 is quantum-mechanically forbidden, the decay rate of this state is orders of magnitude smaller than fluorescence. Thus, the phosphorescence signal is small compared to fluorescence and hence detection of fluorescence is often preferred.

Alternatively, the electron in the first triplet state may interchange energy through collisions with ground state oxygen that has two 'unpaired' electrons with the same spin orientation and thus a triplet ground state (3O_2). Here, the electron of the fluorescent marker returns to the ground state and transfers energy with oxygen that causes a spin flip and hence intersystem crossing to singlet state oxygen or (1O_2). This molecule is cytotoxic and in an aqueous environment very short lived ($\ll 1\mu s$). Singlet state oxygen is believed to be the main cytotoxic agent responsible for cell death in Photodynamic therapy (PDT), which is an experimental therapy for malignancies and other indications (3). If fluorescent markers are used in PDT they are generally called photosensitizers, although not all fluorescent markers are photosensitizers and *vice versa*.

Due to these photophysical and photochemical properties some fluorescent markers can thus be used for fluorescence diagnostics of malignancies, which is the primary focus of this thesis. However, they can also be used for the treatment of malignancies, which is only briefly touched upon within the here presented work.

Optical imaging of fluorescence has been under investigation for the detection of various malignancies using either exogenous fluorescent markers or endogenous autofluorescence, for over 2 decades (4-6). In most applications the diagnostic accuracy obtained has been quite variable. This was mainly due to low fluorescence contrast between normal and tumor tissue, caused by non-specific uptake of more traditional fluorescent markers as fluorescein (7) and PhotofrinTM (8). These relied on rather passive targeting strategies and generally depended on differences in the vasculature or pharmacokinetics of tumor *vs.* normal tissues.

Currently, there are several efforts underway to develop fluorescent markers with improved properties. An 'ideal' fluorescent marker for *in vivo* diagnostics should have a tumor selective uptake with a high tumor-to-normal ratio. It should retain in tumor tissues long enough so that imaging is possible over a relatively flat portion of the pharmacokinetic window. However, it should be cleared from the vasculature fast enough to avoid unspecific leakage during surgical resection. The marker should be biocompatible and non-toxic so that

it can be administered systemically without side effects. To induce a strong fluorescence signal a high probability to absorb excitation photons (i.e. molar absorption coefficient), a high fluorescence quantum yield and a low triplet state yield are preferred. To be able to image multiple fluorescent markers simultaneously one should be able to tune the excitation-emission wavelength, and emission should take place with a high spectral intensity.

A fluorescent marker that has several, but not all, of the above properties is 5-aminolevulinic acid (ALA) induced protoporphyrin IX (PpIX). For this reason it has been investigated extensively in the literature as well as in this thesis. PpIX is produced inside cells that are involved in the heme biosynthesis. ALA is naturally present in all mammalian cells and through various intermediate steps induces mitochondrial production of PpIX. Subsequently, an iron atom is inserted into the PpIX molecule under control of the enzyme ferrochelatase to produce heme. When ALA is exogenously administered selective PpIX accumulation has been observed in various cancers and its earlier stages. Theories have tried to explain this tumor selectivity, contributing factors may be; an increased ALA uptake, a reduction of ferrochelatase, and reduction of iron in cancerous *vs.* normal tissues. But it has been suggested that these theories could be oversimplified and that the reasons for selective PpIX uptake may be more complex (9). The excitation and emission spectra of PpIX are shown in Fig. 2. ALA-PpIX fluorescence imaging has had various degrees of success experimentally and clinically. It has been used for detection of basal cell carcinomas, bladder cancer and cervical intraepithelial neoplasia. Currently, the most promising oncological application of ALA-PpIX, is fluorescence image-guided resection of malignant gliomas. Recent results of a multi-centre Phase III clinical trial in 270 patients demonstrated that patients allocated to fluorescence guidance had double the 6-month progression free survival rates as compared to those allocated to white light (41.0% [32.8-49.2] *vs.* 21.1% [14.0-28.2]; difference between groups 19.9% [9.1-30.7], $p=0.0003$, Z test) (10). These impressive results may be strong enough to soon warrant the first regulatory approval of *in vivo* fluorescence imaging in oncology.

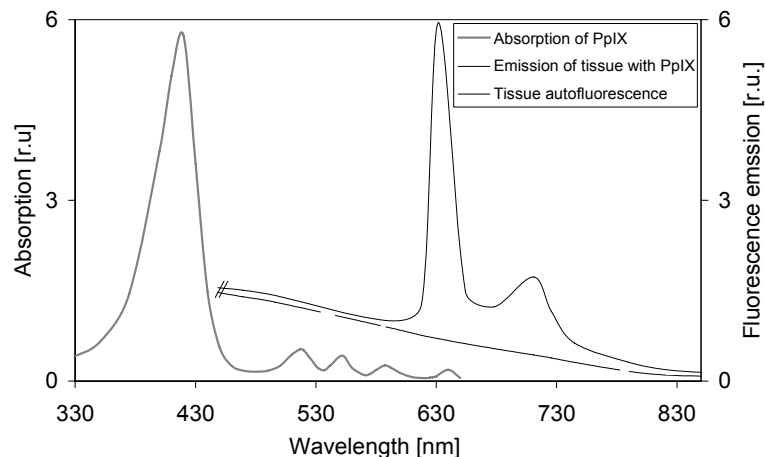


Fig. 2 Illustration of excitation (grey line) and emission (black line) spectra of tissues containing the target fluorophore protoporphyrin IX which has an absorption peak at 410 nm and characteristic emission peaks at 635 and 705nm. The dashed line shows the tissue auto fluorescence.

More recent research is shifting the focus towards novel fluorescent markers that use active targeting strategies. Recent advances in nanotechnology and increasing knowledge of genes and proteins associated with cancer has enabled the engineering of nanoparticles that comprise a targeting moiety (e.g. antibodies, antibody fragments, peptides) conjugated to a fluorescent marker (1, 11-13). These particles hold promise to have an increased, more stable spectral intensity and improved tumor specificity compared with passive-targeting fluorescent markers.

In addition to providing information about the presence or absence of disease, as was typically the case for passive-targeting markers, active-targeting markers can also yield functional information about physiological and molecular processes that relate to the invasiveness, progression and treatment response of the disease (13, 14).

This complementary information, directly available to the clinician during ‘molecular diagnostic screening’ or ‘molecular image-guided surgery’, has the potential to improve clinical decision making and hence could ultimately improve diagnostic accuracy and outcome. To illustrate this, in breast cancer over expression of the human epidermal growth factor receptor 2 (HER-2) was shown to be associated with (a) the presence of disease, (b) involvement of auxiliary lymph nodes (c) grade 3 tumors (d) resistance or benefit of specific adjuvant treatments and (e) poor prognosis (15). Hence, if it were possible to visualize and quantify HER-2 during surgical resection, this information may then be used (a) to enable more complete surgical resection, (b) as a decision criterion for lymph node resection, as direct assessment of (c) tumor grade and (d) for the rational selection of adjuvant treatments, to improve overall prognosis (e).

For both passive- and active-targeting fluorescent markers the ability to accurately quantify the *in vivo* measured fluorescence is critical (12). This, however, is a major challenge as the optically detected signal is influenced by numerous factors other than the concentration of the marker (16, 17-19). The fluorescence signal originates not only from the marker, but also from various other fluorescent molecules naturally present in the tissue such as elastin, collagen and porphyrins and can cause an unknown and variable amount of background autofluorescence (20). The excitation irradiance can vary due to variations in the light output of the excitation source and due to variations in the excitation optics, which both degrade over time. Geometric factors, such as the topography of the tissue, the distance and the angle of the excitation and detection source relative to the tissue surface can change the excitation irradiance and thus the fluorescence emission. Tissue optics, i.e. the scattering and absorption of both the excitation and the fluorescent light also alter the fluorescence signal. For example, visually darker tissues, due to high melanin or blood content, can decrease the propagation of both the excitation and fluorescence emission light. This is further complicated by the fact that the absorption spectrum of blood depends on the oxygenation.

All these factors can contribute to quantification errors. These errors may compromise diagnostic accuracy when using markers as PpIX. Using active-targeting markers such errors may result in suboptimal functional disease information about the disease stage, mechanisms and response to treatment.

Methods that accurately quantify the fluorescence signal, *in vivo*, are thus much needed since these will likely improve diagnostic accuracy and will greatly enhance our ability to extricate functional information. However, methods and procedures for fluorescence quantification are scarcely available in the literature. Instruments that can perform methods

for quantification, so that they can be experimentally tested and validated, are largely unavailable. This leads us to the objectives of this thesis.

Objectives

Primary, investigation of existing and novel methods that allow accurate *in vivo* quantification of both passive- as well as active-targeting fluorescent markers in real-time. These should in particular be applicable to, *i*) diagnostic screening for detection of early cancers or, *ii*) image-guided surgery for the resection of cancer margins.

Secondary, validation of such methods through modeling studies and experiments in tissue equivalent phantoms and via *in vivo* studies in preclinical models.

Tertiary, investigation of the clinical feasibility of using fluorescence quantification methods in patients during clinical pilot studies.

Outline of this thesis

Chapter 2 describes the optical design and construction of a prototype quantitative fluorescence imaging system. The dependence on optical properties was evaluated in phantoms. The dependency of tissue color was assessed using pigmented moles of human volunteers that received topical ALA administration on the skin.

Chapter 3 describes the use of this prototype in a clinical trial with patients whom had Cervical Intraepithelial Neoplasia (CIN) using topically applied ALA. The purpose of this experiment was 1) to investigate the feasibility of CIN detection, and 2) differentiating between the different CIN grades.

Chapter 4 describes the use of fluorescence imaging to guide the surgical resection of brain tumors in a preclinical model. Resection of the tumor under white light was compared to resection under fluorescence guidance.

Chapter 5 discusses the limitations of fluorescence guided resection and describes a possible solution that comprises the combination of fluorescence guided resection followed by low dose photodynamic therapy over prolonged periods of time. An approach to prolonged light delivery was developed and the feasibility of such treatment strategy was verified in a preclinical model.

In **Chapter 6** we mathematically evaluated quantitative fluorescence imaging methods available in the literature with the purpose to identify methods with optimum capability to quantify active-targeting fluorescent markers.

In **Chapter 7** a ratiometric quantification method is introduced. Through mathematical modeling the performance was evaluated. Experimentally the performance was evaluated in optical phantoms employing a prototype imaging system. The clinical feasibility of real-time, image-guided surgery was demonstrated in patients undergoing prostatectomy.

In **Chapter 8** we present the summary and **Chapter 9** is a general discussion of the current status of of *in vivo* fluorescence imaging, how this thesis has contributed to this field and where the field is moving to.

References

1. D. C. Sullivan, M. Ferrari, "Nanotechnology and tumor imaging: seizing an opportunity," *Mol Imaging* **3**(4), 364-9 (2004).
2. J. R. Lakowitz. Principles of fluorescence spectroscopy. New York: Plenum Press; (1983).
3. M. J. Niedre, C. S. Yu, M. S. Patterson, B. C. Wilson, "Singlet oxygen luminescence as an in vivo photodynamic therapy dose metric: validation in normal mouse skin with topical aminolevulinic acid," *Br J Cancer* **92**(2), 298-304 (2005).
4. G. Wagnieres, "Lung cancer imaging with fluorescence endoscopy," In: *Handbook of biomedical fluorescence*, M. Mycek, B. W. Pogue, Eds., pp. 361-396, Marcel Dekker Inc., New York, (2003).
5. R. S. DaCosta, B. C. Wilson, N. E. Marcon, "Light-induced fluorescence endoscopy of the gastrointestinal tract," *Gastrointestinal Endoscopy* **10**(1), 1-33 (2000).
6. D. C. de Veld, M. J. Witjes, H. J. Sterenborg, J. L. Roodenburg, "The status of in vivo autofluorescence spectroscopy and imaging for oral oncology," *Oral Oncol* **41**(2), 117-31 (2005).
7. M. C. Aalders, H. J. C. M. Sterenborg, N. van der Vange, "Fluorescein angiography for the detection of metastases of ovarian tumor in the abdominal cavity, a feasibility pilot," *Lasers Surg Med* **35**(5), 349-53 (2004).
8. W. Stummer, C. Gotz, A. Hassan, A. Heimann, O. Kempfski, "Kinetics of Photofrin II in perifocal brain edema," *Neurosurg* **33**(6), 1075-81; discussion 1081-2. (1993).
9. J. T. H. M. van den Akker, S. B. Brown, "Photodynamic therapy based on 5-aminolevulinic acid: applications in dermatology," In: *Photobiology for the 21st century*, T. P. Coohill, D. P. Valenzeno, Eds., pp. 165-181, Valdenmar Publishing Company, Kansas, (2001).
10. W. Stummer, U. Pichlmeier, T. Meinel, O. D. Wiestler, F. Zanella, H. J. Reulen, F. t. A.-G. s. group, "Fluorescence-guided surgery with 5-aminolevulinic acid for resection of malignant glioma: a randomised controlled multicentre phase III trial," *Lancet Oncol* **7**(5), 392-401 (2006).
11. V. Ntziachristos, J. Ripoll, L. V. Wang, R. Weissleder, "Looking and listening to light: the evolution of whole-body photonic imaging," *Nat Biotechnol* **23**(3), 313-20 (2005).
12. S. R. Cherry, "In vivo molecular and genomic imaging: new challenges for imaging physics," *Phys Med Biol* **49**(3), R13-48 (2004).
13. G. Choy, P. Choyke, S. K. Libutti, "Current advances in molecular imaging: noninvasive in vivo bioluminescent and fluorescent optical imaging in cancer research," *Mol Imaging* **2**(4), 303-12 (2003).
14. K. Sokolov, J. Aaron, B. Hsu, D. Nida, A. Gillenwater, M. Follen, C. MacAulay, K. Adler-Storthz, B. Korgel, M. Descour and others, "Optical systems for in vivo molecular imaging of cancer," *Technol Cancer Res Treat* **2**(6), 491-504 (2003).
15. D. J. Brenton, L. A. Carey, A. A. Ahmed, C. Caldas, "Molecular classification and molecular forecasting of breast cancer: ready for clinical application?," *J Clin Oncol* **23**(29), 7350-7360 (2005).
16. Y. T. Lim, S. Kim, A. Nakayama, N. E. Stott, M. G. Bawendi, J. V. Frangioni, "Selection of quantum dot wavelengths for biomedical assays and imaging," *Mol Imaging* **2**(1), 50-64 (2003).
17. T. Troy, D. Jekic-McMullen, L. Sambucetti, B. Rice, "Quantitative comparison of the sensitivity of detection of fluorescent and bioluminescent reporters in animal models," *Mol Imaging* **3**(1), 9-23 (2004).
18. J. R. Mansfield, K. W. Gossage, C. C. Hoyt, R. M. Levenson, "Autofluorescence removal, multiplexing, and automated analysis methods for in-vivo fluorescence imaging," *J Biomed Opt* **10**(4), 41207 (2005).
19. A. Bogaards, M. C. Aalders, C. C. Zeyl, S. de Blok, C. Dannecker, P. Hillemanns, H. Stepp, H. J. Sterenborg, "Localization and staging of cervical intraepithelial neoplasia using double ratio fluorescence imaging," *J Biomed Opt* **7**(2), 215-20 (2002).
20. R. S. DaCosta, H. Andersson, B. C. Wilson, "Molecular fluorescence excitation-emission matrices relevant to tissue spectroscopy," *Photochem Photobiol* **78**(4), 384-92 (2003).

Chapter 2

Double Ratio fluorescence imaging for the detection of early superficial cancers:

Design, construction and performance of a clinical prototype

A Bogaards¹
MCG Aalders²
AJL Jongen²
E Dekker²
HJCM Sterenborg¹

¹Photodynamic Therapy and Optical Spectroscopy Programme, Subdivision of Clinical Physics, Department of Radiation and Oncology, Daniel den Hoed Cancer Centre/University Hospital, Rotterdam, the Netherlands

²Laser Centre, Academic medical centre Amsterdam, the Netherlands

Abstract

We developed a fluorescence imaging device for the detection of superficial cancer based on the Double Ratio technique. In practical use this device resembles an operation microscope and can be used in a clinical environment. This device acquires 4 different fluorescence images excited at two wavelengths and detected at two wavelengths. From these images it calculates, displays and stores Double Ratio images at a maximum speed of 1Hz. The Double Ratio image gives the distribution of the fluorophore amount present in tissue and is not affected by local variations in tissue optics, i.e. tissue absorption and tissue scattering. The validity of the technique was confirmed here by *ex vivo* tissue equivalent phantom experiments using hematoporphyrin and *in vivo* experiments on normal pigmented moles on Caucasian human skin using δ -aminolevulinic acid induced protoporphyrin IX.

Introduction

Early (pre)cancerous lesions are often hard to find under white light illumination. The medical community is searching for new non-invasive methods to detect these lesions, which often start in the epithelial layer up to a few hundred micrometers below the tissue surface. Fluorescence imaging is an upcoming non-invasive optical technique that produces *in vivo* images with information of these first few hundred micrometers. The interest of research groups (1;2), the investments of various companies like Karl Storz GmbH. & Co. and Xillix Technologies Corp., in combination with recent promising clinical trials (3-8), demonstrate the potential of this technique. In this paper we introduce a new fluorescence imaging device, which may provide diagnostic information about tissue in addition to that offered by currently available fluorescence imaging techniques.

Various approaches are currently under investigation for *in vivo* fluorescence imaging. Some techniques use fluorophores which are naturally present in the tissue, assuming differences in fluorophore content in normal and cancerous tissue (9). Other techniques are based on administration of tumor localising fluorescent drugs to enhance fluorescence contrast (10). Here background fluorescence of natural tissue fluorophores biases the measurement and can be considered an artefact. Using two excitation wavelengths allows subtraction of this background fluorescence (11). Detecting the fluorescence at two wavelengths allows a fluorescence measurement relative to a background (12). Algorithms that are based on multiple excitation and detection wavelengths are also used to optimise contrast between normal and cancerous tissue (13). Some of these methods are successful in specific medical fields, nevertheless, the measured fluorescence signal is influenced by factors which may not be directly related to (pre)malignancy. Factors like spatial variation in natural tissue fluorescence, geometry, variations in excitation fluence, tissue colour and tissue scattering may seriously limit the reliability of fluorescence diagnosis (14).

Attempting to avoid these limitations Sinaasappel and Sterenborg developed the Double Ratio fluorescence imaging technique (15). This technique aims to detect a tumor localising fluorophore, where the Double Ratio image gives the distribution of the fluorophore amount present in tissue. In theory, this technique corrects for variations in natural tissue fluorescence, geometry and excitation fluence. Most important, the Double Ratio technique also corrects for spatial variations in tissue optics, i.e. tissue absorption and tissue scattering. This was confirmed earlier by *in vitro* and *in vivo* point measurement experiments (15;16).

With these unique and useful correcting properties Double Ratio imaging may provide diagnostic information in addition to currently available fluorescence imaging methods.

In this paper we describe a Double Ratio fluorescence imaging device. First we briefly explain the fundamentals on which the imaging technique is based, followed by a description of the prototype design and construction. Finally the dependence on tissue optics was investigated by *ex vivo* experiments on tissue equivalent phantoms and *in vivo* experiments on human moles.

Materials and Methods

The measurement principle

The Double Ratio technique is based on the acquisition of 4 fluorescence signals. Sinaasappel and Sterenberg defined the Double Ratio as (15):

$$\text{Double Ratio} \propto \frac{F_{i,t} F_{j,r}}{F_{j,t} F_{i,r}} \quad \text{Eq. 1}$$

Where F stands for the 4 fluorescence signals, the indices i and j refer to different excitation wavelengths and the indices t and r to different detection wavelengths. $F_{i,t}/F_{j,t}$ is the ‘target ratio’ of the ‘target fluorophore’, i.e. the tumor localising fluorescent drug and $F_{i,r}/F_{j,r}$ is the ‘reference ratio’ of the ‘reference fluorophore’, i.e. the natural tissue fluorescence. The reference ratio is assumed independent of the ‘target fluorophore’, while the target ratio is assumed to increase with increasing presence of target fluorophore. Mathematically the Double Ratio can be expressed as (15):

$$\text{Double Ratio} \propto \frac{1 + \frac{H_{i,t}}{C_r A_{i,t}} C_t}{1 + \frac{H_{j,t}}{C_r A_{j,t}} C_t} = \frac{1 + a C_t}{1 + b C_t} \quad \text{Eq. 2}$$

Where the constants A and H stand for the fluorescence yield of the reference- and target fluorophore, respectively, and the parameters C_r and C_t stand, for the concentration of the reference- and the target fluorophore, respectively.

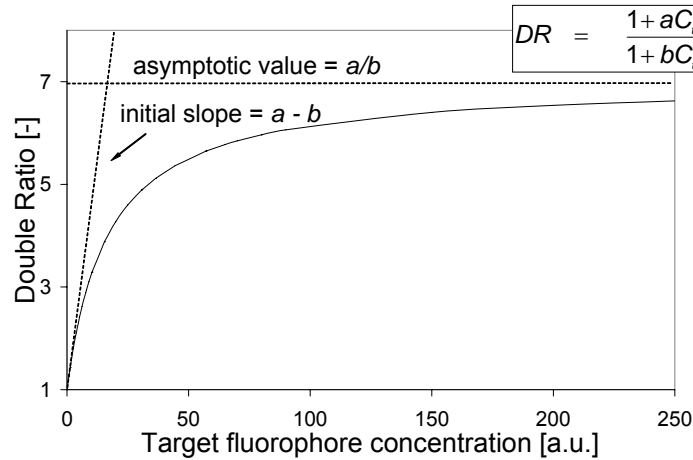


Fig. 1: The relation between the Double Ratio and target fluorophore concentration (C_t).

The parameters a and b are material constants and thus the Double Ratio varies with target fluorophore amount only. Artefacts caused by absorption, scattering, variations in natural tissue fluorescence, excitation fluence and geometry are all cancelled out (15). Later work revealed that the Double Ratio, besides ‘target fluorophore’ concentration, also has a dependency on the fluorescent layer thickness. (17). The relation between the Double Ratio and target fluorophore concentration C_t is described by eq. 2 and plotted in fig. 1. The initial slope of the curve equals a minus b and the curve approaches the asymptotic value of a/b for high target fluorophore concentrations. For maximum sensitivity to changes in fluorophore amount the difference between a and b is preferably as large as possible. This can be obtained by choosing both excitation wavelengths to have a: 1.) maximum difference in fluorescence yield for the target fluorophore and, 2.) a minimum difference in fluorescence yield for the reference fluorophore, see Eq. 2. The Double Ratio measurement technique can be adapted for any kind of ‘target fluorophore’. In principle the approach can also be employed for other types of spectroscopic techniques such as Raman scattering. Prerequisites are sufficiently different excitation spectra for the target and reference fluorophore, and the selection of appropriate excitation and detection wavelengths. The derivation of Eq. 2 and the underlying assumptions are summarised in the appendix.

Imaging system

A novel fluorescence imaging system has been developed and built, according to the Double Ratio technique. A diagram of the system is shown in fig.2. The output beam of a lamp (Ushio, 200W, XeHg) is split in two by a beam splitter.

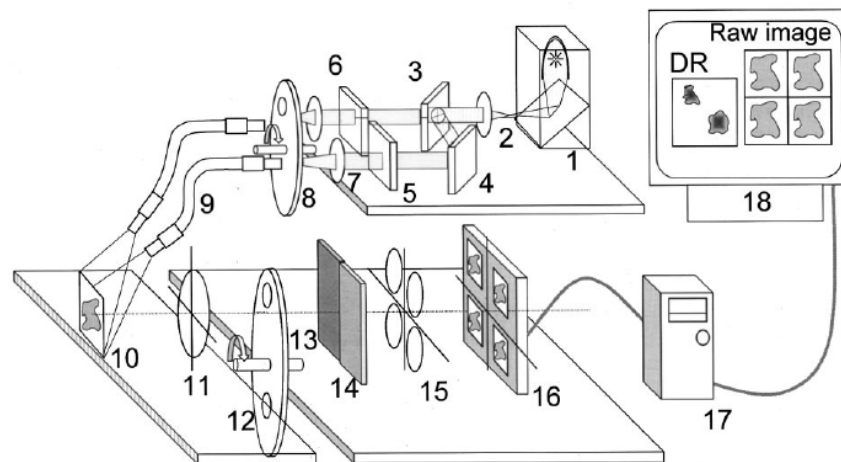


Fig. 2 Overview of the Double Ratio imaging system which can acquire 4 fluorescence images excited at 2 wavelengths and detected at 2 wavelengths. Four images are focused on one CCD chip. Two wavelength detection is then realised by covering each half of the CCD with a filter. Two wavelength excitation is accomplished with an alternating light source. Excitation and image acquisition is synchronised with choppers. Excitation unit: 1.) 200W XeHg lamp, 2. Lens, 3. Beam splitter, 4. Mirror, 5. Excitation filter i , 6. Excitation filter j , 7. Lenses, 8. Chopper (master), 9. Liquid light guides. Detection unit: 10. Tissue, 11. First lens, 12. Chopper (slave), 13. Detection filter t , 14. Detection filter r , 15. Second lens, 16. CCD chip. Processing unit: 17. PC, 18. Display

The two beams are separately guided through excitation filters, a chopper (EG&G, 651-1E) and focussed into two meter long liquid light guides with a core diameter of 8 mm for illumination of the target area. Fluorescence light from the target area is collected by a first

lens. By exchanging the first lenses the camera magnification can be changed, with a focal distance of 10cm or 30cm the detection area is either 1x1cm or 3x3cm. For the longest focal length the excitation power is in the range of a few hundred micro Watts per square centimetre. Excitation and detection filters as well as cameras can be changed easily. Fluorescence emitted from the tissue is detected through two detection filters, covering the vertical halves of the CCD chip. Dedicated optics focus four equal images on this single chip. A slave chopper (EG&G, 651-1E) in the camera unit is synchronised with the chopper in the lamp unit. The slave chopper alternates between the horizontal halves of the CCD. A figure of the illumination phases is shown in fig. 3.

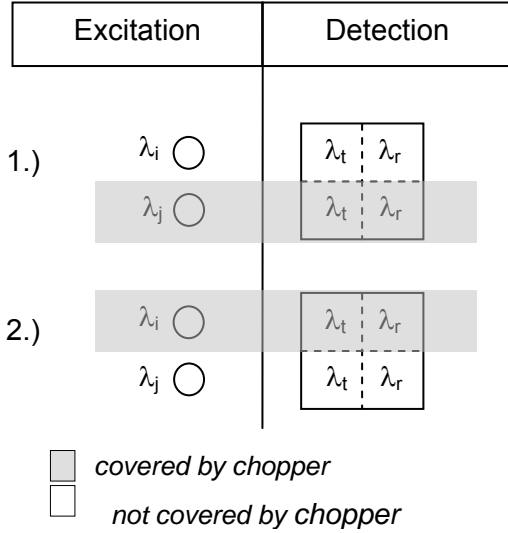


Fig. 3 Acquisition of four equal images with two wavelength excitation and two wavelength detection is performed within 2 illumination phases of the CCD chip: 1) A detection phase with excitation wavelength λ_i . Here two wavelength detection of $F_{i,t}$ and $F_{i,r}$ takes place on the upper half of the CCD through the reference (λ_r) and target detection filter (λ_t). 2) A detection phase with excitation wavelength λ_j . Here a two wavelength detection of $F_{j,r}$ and $F_{j,t}$ takes place on the lower half of the CCD through the reference (λ_r) and target (λ_t) detection filter.

This prototype allows us to acquire four equal images excited at two wavelengths and detected at two wavelengths. The chopping frequency is chosen to be much higher than the frame rate of the camera i.e. a rate of 1200 Hz. This enables the camera to run with a frequency independent of the chopping procedure. In this way we are able to use a wide range of cameras. In our experiments two different types of cameras are used. A high speed slow scan 14 bit cooled monochrome CCD camera, Proscan HSS 1024, with 1024x1024 pixels and a PCI interface. The second camera is a Philips IP 800, a two step intensified video camera. At maximum gain this camera has a sensitivity of 5 μ lux. Interface is a Data translation DT3152 frame grabber. With dedicated software, Interactive Data Language (IDL), the four separate spectral images are extracted and Double Ratio images are calculated, exactly overlaying and dividing the 4 images pixel by pixel according to Eq. 2. Finally, Double Ratio images are displayed at a maximum speed of 1Hz. This system allows to image a wide variety of fluorophores and different tissue types. In practical use the system resembles an operating microscope and can be used in a clinical environment.

Experiments

In theory Double Ratio values are independent on tissue optics, i.e. the scattering coefficient (μ_s) and absorption coefficient (μ_a). To check whether our prototype functions accordingly we performed two experiments: 1.) An *ex vivo* tissue equivalent phantom study and, 2.) an *in vivo* study of normal human pigmented moles on normal Caucasian skin. For these 2 experiments we used porphyrins as ‘target’ fluorophore. The chosen excitation wavelengths band pass filters are: λ_i : 405nm, (Oriel 56541) and λ_j : 435nm, (Oriel 56551). Detection band pass filters for the ‘reference fluorophore’ are: λ_r : 550nm, (Omega optical

550RDF42) and for the ‘target fluorophore’ λ_r : 675nm , (Omega optical 675DF110), see fig. 2. To eliminate any excitation light to enter the camera a long pass filter is positioned in front of the first lens (Schott KV500), not in fig. 2. A figure of the Double Ratio calculation with these filters is shown in fig. 4.

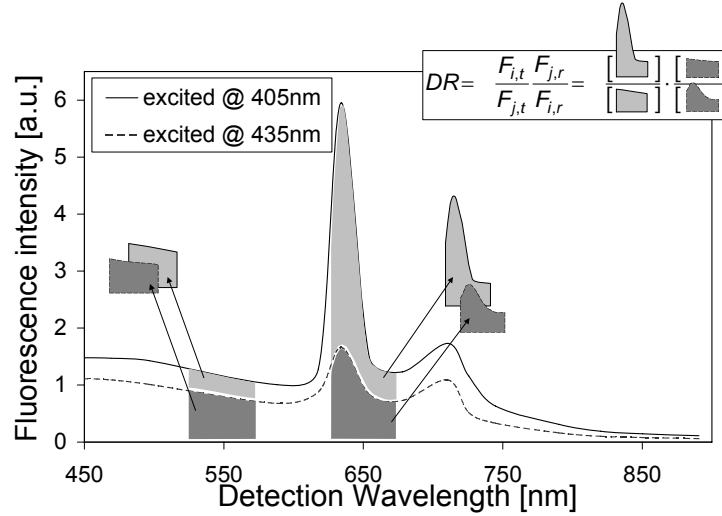


Fig. 4 Graphic presentation of the fluorescence signals needed to calculate a Double ratio. Shown are two schematic fluorescence spectra of tissue with porphyrin. One spectrum is excited at 405nm and the other is excited at 435nm. The grey areas indicate the fluorescence signals in the appropriate wavelength bands needed to calculate a Double Ratio.

Tissue equivalent phantom study

Tissue equivalent phantom studies have been performed to investigate the sensitivity of the Double Ratio images to changes in the absorption coefficient μ_a and scattering coefficient μ_s . Aqueous solutions were prepared with varying concentrations Intralipid10% as a scattering component and Evans Blue as the absorbing component. To simulate natural tissue fluorescence we used fluorescein as ‘reference fluorophore’. Hematoporphyrin (Hp) was used as ‘target fluorophore’. Before adding Hp to the phantom it was pre-diluted in a small amount of acetone to enhance solubility in water. Five different phantoms were made in total. The range of optical properties that was used is listed in table 1. Double Ratio imaging took place for each phantom while varying the Hp concentration.

Table 1 The optical properties of the tissue equivalent phantoms at 635nm. Phantom 4 aims to simulate human skin, while phantom 5 aims to simulates human liver (18).

Phantom	μ'_s [cm^{-1}]	μ_a [cm^{-1}]
1	4	2.8
2	30	2.8
3	4	4.2
4	49	1.8
5	62	2.3

Human mole study

Previous studies have shown that high absorption of dark coloured lesions on a less absorbing light coloured skin can cause biased fluorescence measurements (14). To study

how our prototype deals with these absorption artefacts *in vivo* we studied normal pigmented moles on Caucasian skin, comparing the Single Ratio introduced by Profio to correct for background fluorescence (12) with Double Ratios. Here, the Single Ratio is the protoporphyrin IX fluorescence detected in the red, divided by the natural tissue fluorescence, detected in the green, both excited at 405nm. The measurements were performed on two volunteers on which we selected two pigmented moles each. Topical administration with a solution of 20% δ -ALA in Instillagel took place. The gel was applied on the pigmented mole and surrounding light coloured skin and was held into position with Tegaderm. Through metabolic reactions in the tissue δ -ALA is converted to the ‘target fluorophore’ Protoporphyrin IX. After half an hour the Tegaderm was removed and the skin was cleaned with a gauze. Two hours later Double Ratio images were taken.

Results

Tissue equivalent phantom study

Fig. 5 shows the Double Ratio values versus Hp concentration for the five phantoms. The graph shows five similar measured curves close to curve predicted by Eq. 2. There is a good correlation between the measured values and the theoretically predicted curve given by Eq. 2, which is plotted in the graph as well. A correlation coefficient of 0.98 was found.

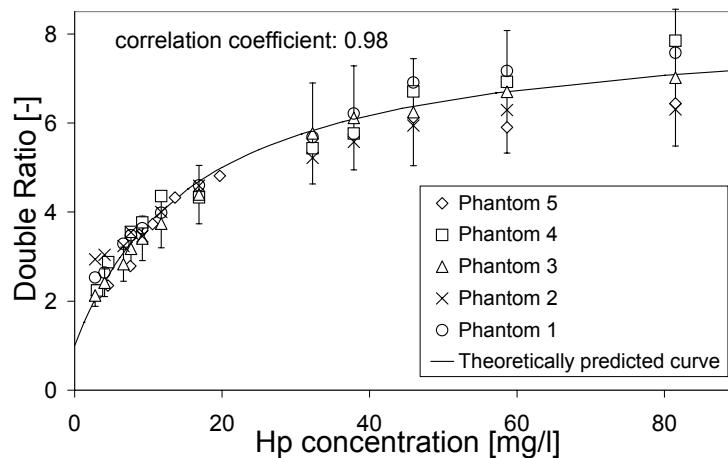


Fig. 5 Hp concentration versus Double Ratio for five different phantoms (see Table 1.). Although these phantoms have different absorbing and scattering properties similar Double Ratio values were found close to the curve predicted by Eq. 2. A correlation coefficient of 0.98 was calculated between theory and measurement.

Human mole study

Fig. 6a shows natural tissue fluorescence image of a clinically benign pigmented mole on normal light coloured skin at 550nm. Throughout the whole image hairs are visible and a v-mark was drawn on the skin for easy recognition of the lesion. Obvious are the higher absorption at the location of the mole and the marking. Figure 6b shows the protoporphyrin IX fluorescence divided by the natural tissue fluorescence ratio of this mole. The normal lesion and v-mark show a clearly higher ratio in comparison with the normal

surrounding tissue, illustrating the fact that green light is absorbed stronger than red light in these mole and v-mark, which biases this ratio. Fig. 6c shows the Double Ratio image. Both the normal mole and v-mark have nearly disappeared which is an indication that they have similar porphyrin concentrations in comparison with the surrounding tissue. The v-mark and hairs have not completely disappeared but are still slightly visible. This is caused by non exact overlay of the four images. We found similar results in all 4 moles.

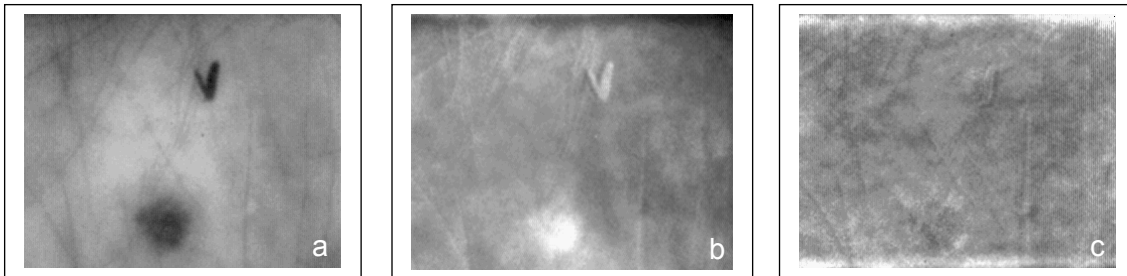


Fig. 6 Fluorescence images of a normal dark coloured mole on a normal light coloured skin after application of 5-ALA. We drew a v-mark on the skin for easy recognition. (a) Natural tissue fluorescence image (550nm). (b) protoporphyrinIX fluorescence image (675nm) divided by the natural fluorescence ratio image (550nm) here we see biased elevated values at the position of the v-mark and mole due to a stronger absorption in the green in comparison with the red. (c) Double ratio image with similar values for mole, v-mark and skin, indicating similar protoporphyrinIX levels for mole, v-mark and surrounding skin.

Acknowledgements

This work was funded by “The Dutch Technology Foundation”, grant no. AGN 44.3413, and the European Commission, BIOMED, grant no. BMH4 CT172260. We also acknowledge the mechanical engineering efforts of Arie Steenbeek.

References

1. Wagnieres GA, Star WM, Wilson BC. In vivo fluorescence spectroscopy and imaging for oncological applications. *Photochem Photobiol* 1998; 68:603-632.
2. Andersson-Engels S, Johansson J, Svanberg K, Svanberg S. Fluorescence imaging and point measurements of tissue: applications to the demarcation of malignant tumors and atherosclerotic lesions from normal tissue. *Photochem Photobiol* 1991; 53:807-814.
3. Kriegmair M, Zaak D, Stepp H, Stepp H, Baumgartner R, Knuechel R et al. Transurethral resection and surveillance of bladder cancer supported by 5-aminolevulinic acid-induced fluorescence endoscopy. *Eur Urol* 1999; 36(5):386-392.
4. Stummer W, Novotny A, CA ND, Stepp H, Goetz C, Bise K et al. Fluorescence-guided resection of glioblastoma multiforme by using 5-aminolevulinic acid-induced porphyrins: a prospective study in 52 consecutive patients. *J Neurosurg* 2000; 93(6):1003-1013.
5. Hillemanns P, Weingandt H, Baumgartner R, Diebold J, Xiang W, Stepp H. Photodetection of cervical intraepithelial neoplasia using 5-aminolevulinic acid-induced porphyrin fluorescence. *Cancer* 2000; 88(10):2275-2282.
6. Lam S, Palcic B. Autofluorescence bronchoscopy in the detection of squamous metaplasia and dysplasia in current and former smokers. *J Nat Cancer Inst* 1999; 91:561-563.

7. DaCosta RS, Wilson BC, Marcon NE. Light-induced fluorescence endoscopy of the gastrointestinal tract. *Gastrointest Endosc Clin N Am* 2000; 10(1):37-69, vi.
8. Zargi M, Fajdiga I, Smid L. Autofluorescence imaging in the diagnosis of laryngeal cancer. *Eur Arch Otorhinolaryngol* 2000; 257(1):17-23.
9. Lam S, MacAulay C, Hung J, Leriche JC, Profio AE, Palcic B. Detection of dysplasia and carcinoma in situ with a lung imaging fluorescence endoscope device. *J Thor Cardiovasc Surg* 1993;1035-1040.
10. Baumgartner R, Stepp H. Photodynamic diagnosis using 5-aminolevulinic acid (5-ALA) for minimally-invasive treatment of cancer. *Min Invas Ther & Allied Technol* 1998; 7(6):495-501.
11. Baumgartner R, Fisslinger H, Jocham D, Lenz H, Ruprecht L, Stepp H et al. A fluorescence imaging device for endoscopic detection of early stage cancer - instrumental and experimental studies. *Photochem Photobiol* 1987; 46:759-763.
12. Profio AE, Balchum OJ, Carstens F. Digital background subtraction for fluorescence imaging. *Med Phys* 1986; 13:717-721.
13. Andersson-Engels S, Ankerst J, Johansson J, Svanberg K, Svanberg S. Laser-induced fluorescence in malignant and normal tissue of rats injected with benzoporphyrin derivative. *Photochem Photobiol* 1993; 57(6):978-983.
14. Sterenborg HJCM, Saarnak AE, Frank RGJ, Motamedi M. Evaluation of spectroscopic correction techniques for *in vivo* fluorescence measurements on pigmented lesions. *J Photochem Photobiol* 1996; B35:159-165.
15. Sinaasappel M, Sterenborg HJCM. Quantification of hematoporphyrin derivative by fluorescence measurement using dual wavelength excitation and dual wavelength detection. *Appl Opt* 1993; 32:541-548.
16. Sterenborg HJ, Saarnak AE, Frank R, Motamedi M. Evaluation of spectral correction techniques for fluorescence measurements on pigmented lesions *in vivo*. *J Photochem Photobiol B* 1996; 35(3):159-165.
17. Saarnak AE, Rodrigues T, Schwartz J, Moore AL, van Gemert MJC, Thomsen S et al. Influence of tumour depth, blood absorption and autofluorescence on measurement of exogenous fluorophores in tissue. *Lasers Med Sci* 1998; 13:22-31.
18. Cheong W-F, Prah A, Welch AJ. A review of the Optical Properties of Biological Tissues. *IEEE J Quant Electr* 1990; 26(12):2166-2185.

Appendix: Derivation of the Double Ratio

Fluorescence emerging at the surface of a semi-infinite medium is described by:

$$F_{i,m}(\vec{x}) = \iiint_{\text{wholebody}} \varphi_i(\vec{r})(C_a(\vec{r})A_{i,m} + C_t(\vec{r})B_{i,m})\xi_m(\vec{r}, \vec{x})d\vec{r} \quad \text{eq. A.1}$$

where :

the indices i and m refer to the excitation and emission wavelengths, respectively,

$F_{i,m}(\vec{x})$ = the fluorescence signal on surface location \vec{x} ,

$C_a(\vec{r}), C_t(\vec{r})$ = concentrations of auto - and target - fluorophores,

$A_{i,m}, B_{i,m}$ = fluorescence yields, (quantum yields in case in case concentrations are in

numbers of molecules per volume and fluorescence and excitation fluence rate is in photons per second)

$\varphi_i(\vec{r})$ = excitation light distribution,

$\xi_m(\vec{r}, \vec{x})$ = escape function.

When attempting to quantify target fluorophore C_t we encounter the problem

that $\varphi_i(\vec{r})$ and $\xi_m(\vec{r}, \vec{x})$ are strongly dependent on absorption and scattering

The Double Ratio is defined as:

$$DR(\vec{x}) = \frac{F_{i,m}(\vec{x})F_{j,n}(\vec{x})}{F_{i,n}(\vec{x})F_{j,m}(\vec{x})} \quad \text{eq. A.2}$$

$$= \frac{\iiint_{\text{wholebody}} \varphi_i(\vec{r})(C_a(\vec{r})A_{i,m} + C_t(\vec{r})B_{i,m})\xi_m(\vec{r}, \vec{x})d\vec{r} \quad \iiint_{\text{wholebody}} \varphi_j(\vec{r})(C_a(\vec{r})A_{j,n} + C_t(\vec{r})B_{j,n})\xi_n(\vec{r}, \vec{x})d\vec{r}}{\iiint_{\text{wholebody}} \varphi_i(\vec{r})(C_a(\vec{r})A_{i,n} + C_t(\vec{r})B_{i,n})\xi_n(\vec{r}, \vec{x})d\vec{r} \quad \iiint_{\text{wholebody}} \varphi_j(\vec{r})(C_a(\vec{r})A_{j,m} + C_t(\vec{r})B_{j,m})\xi_m(\vec{r}, \vec{x})d\vec{r}}$$

To simplify this expression we make a number of reasonable assumptions. First we assume (sufficiently) very shallow penetration of the excitation light. As a consequence, lateral diffusion of excitation light can be ignored and only the superficial concentration of the fluorophore plays a role. Hence we can write:

$$\begin{aligned} \varphi(\vec{r}) &= I(\vec{s})\rho(z) \\ C(\vec{r}) &\rightarrow C(\vec{s}) \\ F(\vec{x}) &= \iint_{\text{surface}} \int_{\text{depth}} I(\vec{s})\rho(z)(C_a(\vec{s})A + C_t(\vec{s})B)\xi(\vec{s}, \vec{x})d\vec{s}dz \\ &= \int_{\text{depth}} \rho(z)dz \iint_{\text{surface}} I(\vec{s})(C_a(\vec{s})A + C_t(\vec{s})B)\xi(\vec{s}, \vec{x})d\vec{s} \end{aligned} \quad \text{eq. A.3}$$

where \vec{s} is a vector on the surface

Note that the escape function now contains two surface vectors; it has become equal to the point spread function.

Second, we assume that it is not useful to consider variations in fluorophore distribution on a scale smaller than what the imaging system can resolve. As the point spread function defines the limit for the sharpness of the fluorescence image we assume:

$$I(\vec{s})C(\vec{s})\xi(\vec{s}, \vec{x}) = I(\vec{x})C(\vec{x})\xi(\vec{s}, \vec{x}) \text{ for } \vec{s} \text{ around } \vec{x} \quad \text{eq. A.4}$$

$$= 0 \quad \text{elsewhere}$$

Now we can write:

$$F(\vec{x}) = I(\vec{x}) \left(C_a(\vec{x})A + C_t(\vec{x})B \right) \int_{\text{depth}} \rho(z) dz \iint_{\text{surface}} \xi(\vec{s}, \vec{x}) d\vec{s} \quad \text{eq.A.5}$$

Putting this back into the Double Ratio we obtain:

$$DR(\vec{x}) = \frac{I_m(\vec{x}) \left(C_a(\vec{x})A_{i,m} + C_t(\vec{x})B_{i,m} \right) \int_{\text{depth}} \rho_i(z) dz \iint_{\text{surface}} \xi_m(\vec{s}, \vec{x}) d\vec{s} I_n(\vec{x}) \left(C_a(\vec{x})A_{j,n} + C_t(\vec{x})B_{j,n} \right) \int_{\text{depth}} \rho_j(z) dz \iint_{\text{surface}} \xi_n(\vec{s}, \vec{x}) d\vec{s}}{I_n(\vec{x}) \left(C_a(\vec{x})A_{i,n} + C_t(\vec{x})B_{i,n} \right) \int_{\text{depth}} \rho_i(z) dz \iint_{\text{surface}} \xi_n(\vec{s}, \vec{x}) d\vec{s} I_m(\vec{x}) \left(C_a(\vec{x})A_{j,m} + C_t(\vec{x})B_{j,m} \right) \int_{\text{depth}} \rho_j(z) dz \iint_{\text{surface}} \xi_m(\vec{s}, \vec{x}) d\vec{s}}$$

$$= \frac{\left(C_a(\vec{x})A_{i,m} + C_t(\vec{x})B_{i,m} \right) \left(C_a(\vec{x})A_{j,n} + C_t(\vec{x})B_{j,n} \right)}{\left(C_a(\vec{x})A_{i,n} + C_t(\vec{x})B_{i,n} \right) \left(C_a(\vec{x})A_{j,m} + C_t(\vec{x})B_{j,m} \right)} \quad \text{eq. A.6}$$

$$\text{Defining: } a = \frac{B_{i,m}}{C_a A_{i,m}}, \quad b = \frac{B_{j,m}}{C_a A_{j,m}}, \quad d = \frac{A_{i,m} A_{j,n}}{A_{j,m} A_{i,n}} \approx 1, \quad \frac{a}{b} = \frac{A_{j,m}}{A_{i,m}} \frac{B_{i,m}}{B_{j,m}} \approx \frac{B_{i,m}}{B_{j,m}} \quad \text{eq. A.7}$$

Gives us a simple expression for the Double Ratio as function of the target fluorophore:

$$DR(\vec{x}) = \frac{1 + aC_t(\vec{x})}{1 + bC_t(\vec{x})} \quad \text{eq. A.8}$$

$$\text{Note that } \frac{a}{b} = \frac{A_{j,m}}{A_{i,m}} \frac{B_{i,m}}{B_{j,m}} \approx \frac{B_{i,m}}{B_{j,m}}$$

i.e. the maximum double ratio that can be obtained is roughly equal to the ratio of the excitation coefficients of the target fluorophore.

Note that the DR is not proportional to the concentration. It is sometimes convenient to present a quantity that is proportional to the concentration of the target fluorophore. This can be done in case good estimates of d and a/b are available:

$$C^* = \frac{\left(1 - DR(\vec{x})/d \right)}{\left(DR(\vec{x})/d - a/b \right)} = bC_t(\vec{x}) \quad \text{eq. A.9}$$

Chapter 3

Localization and staging of cervical intraepithelial neoplasia using Double Ratio fluorescence imaging

A Bogaards¹
MCG Aalders²
CC Zeyl³
S de Blok³
C Dannecker⁴
P Hillemanns⁴
H Stepp⁴
HJCM Sterenborg¹

¹Photodynamic Therapy and Optical Spectroscopy Program, Department of Radiation Oncology, University Hospital Rotterdam, The Netherlands

²Laser Center, Academic Medical Center, Amsterdam, The Netherlands

³Department of Obstetrics and Gynecology, Onze Lieve Vrouwe Gasthuis, Amsterdam, The Netherlands

⁴Laser-Forschungslabor an der Urologischen Klinik, Ludwig maximillians Universitaet, Munchen, Germany.

Abstract

A clinical pilot study was performed to evaluate a new fluorescence imaging technique for diagnosing cervical intraepithelial neoplasia. The fluorescence imaging prototype performed quantitative imaging of PpIX induced by topically applied ALA using Double Ratio (DR) fluorescence imaging technique developed in our group. In total 38 patients entered the protocol, 16 were colposcopically selected for biopsy. Of these 16 patients fluorescence images were taken and 19 sites were biopsied and the disease was staged histopathologically. DR fluorescence imaging of the cervix using our general purpose prototype appeared to be cumbersome but feasible. In 4 cases strongly localised fluorescent hotspots were observed at the location where the disease was colposcopically visible. In the other cases the fluorescence showed a more diffuse multifocal image. The value of the DR determined at the site of biopsy correlated in a statistically significant way with the histopathologically determined stage of the disease (Spearman rank correlation, $r = 0.881$, $p < 0.001$ (confidence interval 0.7044 - 0.9552)). This suggests that non-invasive staging of CIN using this technique is feasible. We believe that the results of this study justify the development of a dedicated device that combines regular white light colposcopy with DR fluorescence imaging.

Introduction

Cervical cancer is the leading cause of mortality in female cancer and the second most common cancer in females worldwide (1). The introduction of new screening and treatment modalities led to a decrease in mortality of cervical cancer over the last 50 years (2,3) However, in the last two decades nation wide screening programs revealed an increase in the incidence of cervical cancer. Hornung *et al.* (4) estimated that the mortality of cervical cancer will rise by 20% in the next decade unless improvements are made in the current screening and detection techniques.

Colposcopy has proved to be a useful diagnostic tool in identifying the most atypical site for biopsy on the cervix (5, 6). When women with an abnormal Pap-smear are referred for colposcopy, diagnosis and treatment of cervical intra-epithelial neoplasia (CIN) requires several visits to the doctor. With conventional colposcopy, using acetic-acid staining to select the most atypical site for taking a biopsy, only 53.6% of the removed biopsies contain histological evidence of a dysplastic process(6). In an overview of fourteen papers, by Hopman *et al.*, the positive predictive value of colposcopically directed biopsy was poor for 'no CIN' and increased with increasing stage of the disease (7). Also a considerable inter-observer variability regarding diagnosing CIN is reported in the literature, for colposcopists as well as for histopathologists (8-11).

Fluorescence imaging and spectroscopy are relatively new experimental techniques for the detection of superficial epithelial changes. Fluorescence diagnostics is based on detecting *in vivo* differences in fluorescence between normal and cancerous tissues. Fluorescence is induced by excitation of fluorophores in the tissue, usually with blue or UV light. The area of interest is then imaged with a sensitive camera or a point measurement is performed with a spectrograph. The shallow penetration of the excitation light makes this tool particularly suitable for superficial lesions. Differences in fluorescence between normal and cancerous tissue can be naturally present due to different fluorescent molecules in normal and cancerous tissue or may lay in different absorption or scattering in tissue (7,8,14,15). The use of natural tissue fluorescence spectroscopy for CIN screening was extensively evaluated and reviewed by Mitchell *et al.* They concluded that fluorescence spectroscopy performs better than colposcopy (16).

Differences in fluorescence between normal and cancerous tissue can also be enhanced by administration of a tumor localizing fluorescent drug, preferentially accumulating in cancerous cells. Several fluorescent tumor localizers are currently under study. 5-Aminolevulinic acid (5ALA) is currently a popular drug for photodynamic therapy. When administered topically it diffuses into the cells and converts to the fluorescent Protoporphyrin IX (PpIX). Selective accumulation in certain cell types may be caused either by differences in cellular enzyme levels, or by differences in the accessibility to ALA (17-20). Hillemanns et al used this approach for CIN screening based on fluorescence imaging. He showed that fluorescence imaging for CIN screening has similar results compared to colposcopy. However by using a more quantitative method, fluorescence spectroscopy with a fiber-optic probe at a fixed distance, he found a significant improvement over colposcopy (21).

Sinaasappel and Sterenberg described a more quantitative method for fluorescence measurements, the Double Ratio (DR) measurement technique (22). Two excitation wavelengths (λ_i and λ_j) and two detection fluorescence wavelength ranges (λ_m and λ_n) are used to generate four different fluorescence images from which a DR image is calculated. The DR algorithm is designed to compensate for tissue color and tissue light scattering and produces an image that is dependent on the amount of the fluorescent tumor localizer only (23):

$$DR = \frac{F_{i,m} F_{j,n}}{F_{i,n} F_{j,m}} = \frac{1 + \alpha \frac{C}{C_0}}{1 + \frac{C}{C_0}} \quad \text{eq.1.}$$

where $F_{x,y}$ stands for the fluorescence obtained with excitation wavelength λ_x detected at wavelength λ_y and C stands for the concentration of the photosensitizer. The parameters α and C_0 are unknown constants that are related to the fluorescence quantum yields of the autofluorophores and of PpIX. It can be shown (23) that α for PpIX in tissue has a value of approximately 8. DR is a smooth function of C/C_0 . At low values of C/C_0 it is proportional to C/C_0 and at higher values it saturates at a value of α . DR images therefore have a direct relation to the PpIX distribution of the imaged area, unbiased by the usual optical artifacts.

The aim of this clinical pilot study is threefold. First, we will test our general purpose fluorescence imaging prototype in a clinical setting. Second, we will evaluate the feasibility of using the ALA-DR approach as fluorescence guide for taking biopsies. Third, we will test whether this quantitative fluorescence imaging approach is capable of non-invasive staging of CIN.

Materials & Methods

Patient selection

Women with an abnormal Pap smear, routinely referred to the clinic for colposcopic examination, were asked to participate in this study. Pregnant or lactating women were excluded. A total of 30 volunteers enrolled in this study. Ages varied between 19 and 45 years with a mean age of 30 years. We excluded 6 volunteers with a history of previous surgery, causing unknown changes to the epithelium. Another 8 volunteers were

colposcopically unsuspect for CIN and consequently no biopsies could be taken. Finally, 19 biopsies from 16 volunteers were available for our analysis.

Application of ALA

The ALA was purchased from Medac GmbH (Hamburg Germany) in crystallized form. On the day of use it was dissolved in a concentration of 1% (weight/weight) in sterile saline solution with the pH adjusted to 5.5 using sodium hydrogen carbonate (21). Sterile gauzes drenched with 10ml of this solution were applied to the cervix. The application time aimed for was 60 minutes, but in practice ranged from 60-120 minutes.

DR fluorescence imaging prototype

The DR fluorescence camera is a general purpose prototype developed by our group. In practical use it resembles an operating microscope. Preliminary clinical experiments have been performed for neurosurgery and dermatology. The device uses two violet wavelengths for excitation of the cervix, 405nm and 435nm at intensities of about 100 and 200 $\mu\text{W}/\text{cm}^2$, respectively. These are not the optimum wavelengths for DR imaging of PpIX, but a compromise between contrast and signal to noise ratio. The excitation light is generated with a 200 Watt Hg-Xe lamp, two line filters and a chopper alternating the 2 excitation wavelengths. Fluorescence of the cervix is detected with an image intensified camera (Philips IP 800) through a red and green filter (550nm, bandwidth 42 nm and 675nm, bandwidth 110 nm). In this manner 4 different fluorescence images are acquired. These are processed into DR images by ratioing the two red and green images and subsequently ratioing the two ratio images. A detailed description of this imaging device and the theory behind it can be found elsewhere (22-24). For focusing and positioning a simple white light (monochrome) imaging mode is available.

Procedure

At the time of colposcopy the moist gauze containing the ALA is removed. Then a regular colposcopic procedure is performed, including acetic acid staining and photographic documentation of the cervix. In case the decision is made to take a biopsy, the position where the biopsy will be taken is marked on the photograph (Polaroid) that was taken to document the colposcopy procedure. Subsequently, the colposcope is removed and the fluorescence imaging device is positioned and focused. Positioning the device took 1-5 minutes, acquiring the fluorescence images approximately 60 seconds. The resulting DR image was not available to the clinician during the procedure. Next, the fluorescence imaging device is removed and the colposcope is used to take the biopsy. The biopsy is then subjected to standard histopathological evaluation.

Data analysis

There were 2 blind steps in the procedure to avoid bias. First, as mentioned above, the clinician has not seen any fluorescence image before the biopsy is taken. Second, the results of the histopathologic evaluation of the biopsies were not available to us at the time of dataprocessing. Defining the location of the biopsy site in the DR image was not simple as it involved matching two different images taken with different devices (i.e. the colposcope and the fluorescence imaging device). The outcome of this procedure might be biased.

Results

General

Although the prototype functioned properly in the technical sense, its use in this particular clinical field proved to be very cumbersome. Especially positioning and focusing the device was difficult and time consuming. A typical example of a set of images is given in figure 1b. The speculum, visible on the right side of the white light image, often caused severe artifacts in the fluorescence image that were not easy to avoid. These artifacts were related to reflections of excitation and fluorescence light on the stainless steel surface that were not completely blocked by the detection filters. In addition, the wall of the vagina (as far as it was not covered by the speculum) was out-of-focus and usually fluoresced intensely. In the fluorescence image this area is painted black, so only the fluorescence on the cervix remains visible. DR fluorescence images were taken in 16 patients, on whom a total number of 19 biopsies were obtained resulting in various different stages of CIN (Table 1).

Table 1 *The number of biopsies and corresponding CIN stage, as determined by histopathology*

Stage	Number
No CIN	3
CIN I	7
CIN II	3
CIN III	6

DR fluorescence images of no CIN

Figure 1a shows the white light image and the corresponding DR image of the cervix of a patient that was colposcopically diagnosed as no CIN. Although some speckles are visible, DR values close to 1 are found throughout the cervix, suggesting a very minimal PpIX production. A similar situation is depicted in figure 1b, the main difference being that this cervix is severely inflamed. Nevertheless, the DR image shows a uniform low value, suggesting low PpIX levels throughout the cervix.

Localization of CIN with DR fluorescence imaging

In 4 cases a region with clear boundaries could be recognised in the DR image. In all 4 cases this region matched the location where the biopsy was taken. The 4 lesions that showed localised fluorescence were all classified as CIN III. An example of this is shown in figure 2a. In the other 15 cases larger areas with unclear boundaries showed elevated DR values. An example of a more diffuse fluorescence image is given in figure 2b. In these cases the location with the highest DR never coincided with the location where a biopsy was taken.

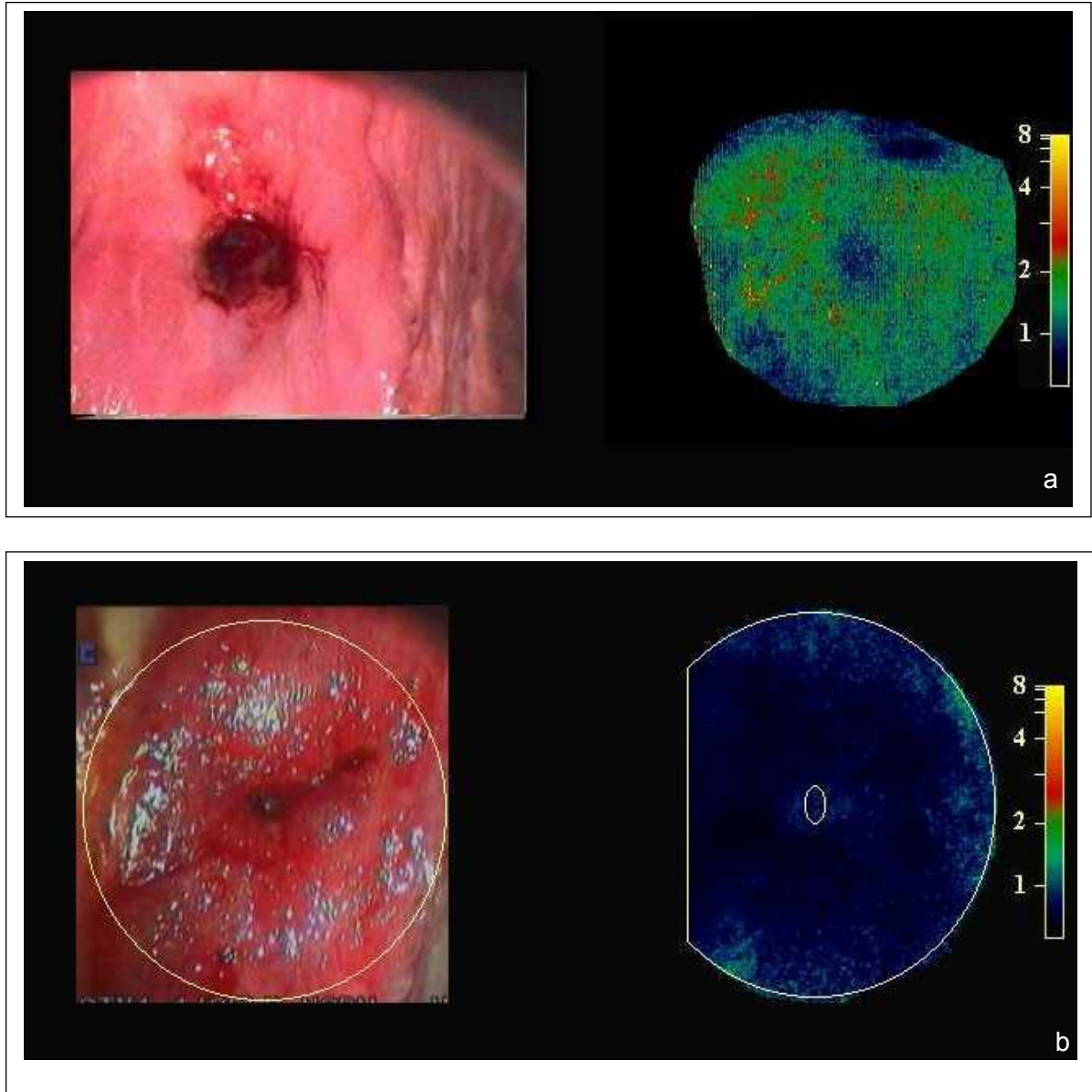


Fig. 1 White light image and DR fluorescence images for two cases where clinically no CIN was detected and consequently no biopsy was taken. (a) normal cervix, fluorescence intensity is low, although some speckles are present. (b) inflamed cervix. The DR values are close to 1, indicating relatively low PpIX levels.

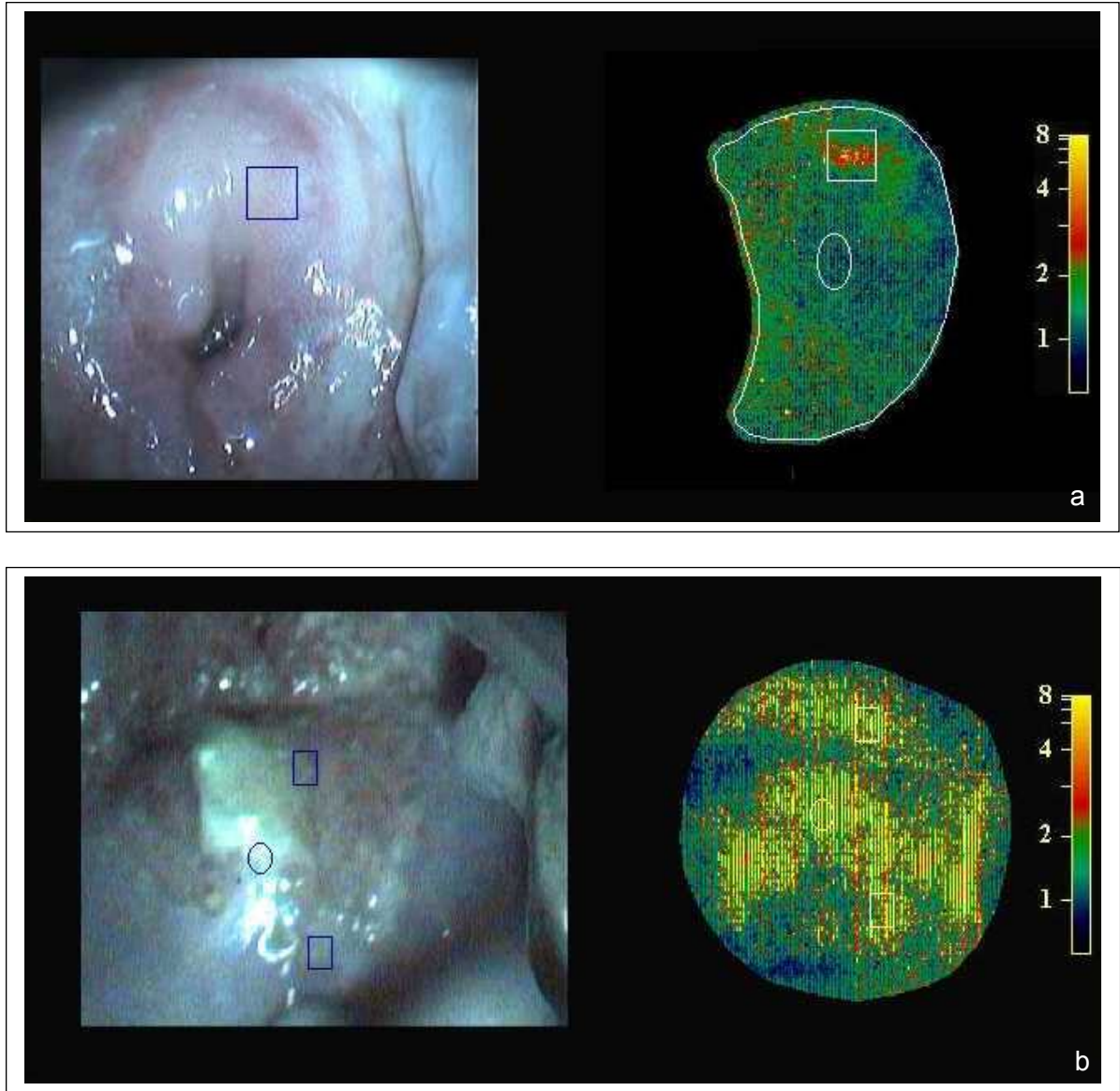


Fig. 2 White light images and corresponding fluorescence images of two cases histopathologically confirmed as CIN III. The locations where the biopsies were taken are indicated with a square, the ellipse indicates the position of the portio in the fluorescence image. In the first case (a) a clearly localised spot is visible in the fluorescence image and corresponds to the location where the biopsy was taken. In the second case (b) a more diffuse increase in the DR is observed.

Staging of CIN with DR fluorescence imaging

Figure 3 shows the DR value averaged over a 16 by 16 pixel square located at the position where the biopsy was taken versus the histopathological stage. Although some outliers are clearly present, there appears to be a significant correlation between DR value and histopathology (Spearman rank correlation, $r = 0.881$, $p < 0.001$ (confidence interval 0.7044 - 0.9552))

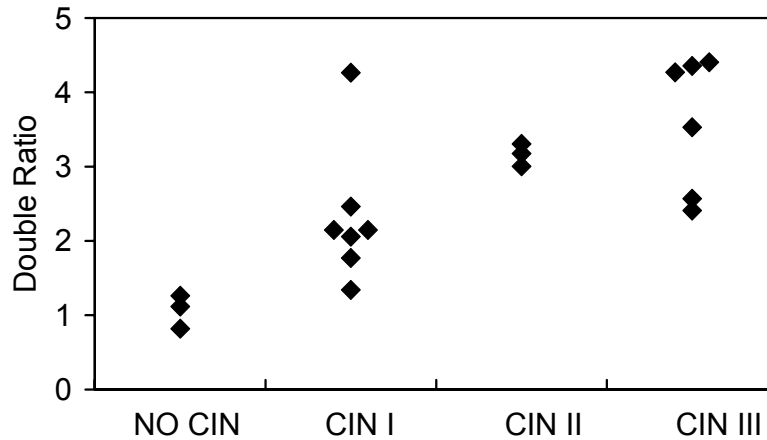


Fig. 3 DR value calculated on the location where the biopsy was taken versus the histopathological staging performed on the biopsy. Data from 19 biopsies.

Discussion

Localization

Fluorescence images were obtained of a total number of 16 cervixes. In 13 of these we have histopathological confirmation of intraepithelial neoplasia. In 4 (of these 13) a clearly localised lesion was visible in the fluorescence image on a location coinciding with the (previously determined) biopsy location. The biopsies from these sites were all classified as CIN III. In the other 9 cervixes the fluorescence images showed multiple hotspots of variable intensity or a more diffuse elevation of the fluorescence DR. This suggests a more multifocal nature of the disease in these cases.

Staging

The strong correlation between the DR value and the histopathological classification as shown in figure 3 is quite striking. This might suggest that there is a relation between the amount of PpIX accumulating and the stage of the disease. However, we believe that a different mechanism is behind this phenomenon. In the derivation of eq.1 a semi-infinite homogenous medium with a homogenous PpIX distribution is assumed. The clinical situation is obviously a lot more complex; In the case of topically applied ALA on a mucosal surface a PpIX containing layer may have a thickness of up to a few hundred micrometer; of the order of, or less than the penetration depth of the violet excitation light. Furthermore, an epithelial tumor originates from the boundary between the stromal and epithelial layer and then progresses towards the top surface, into the monitored tissue volume. This will increase

the average porphyrin concentration in this volume. As a consequence, we must seriously doubt the validity of the assumption of a semi-infinite homogenous distribution of PpIX. To gain more insight in the dependency of the DR on the layered clinical situation, we performed Monte Carlo simulations for which we defined a two-layered structure representing the epithelial layer and an underlying stromal layer. Both layers were assumed to autofluoresce, only the epithelial layer was assumed to produce PpIX fluorescence. Fluorescence emerging from the surface was calculated for both excitation and detection wavelengths and a DR value was calculated. By performing different simulations with various layer thicknesses we could assess the dependency of the DR on layer thickness. The input parameters for the calculations were obtained from literature and personal measurements. The technique and the methods are described more in detail in appendix I. The results of the simulations are depicted in figure 4.

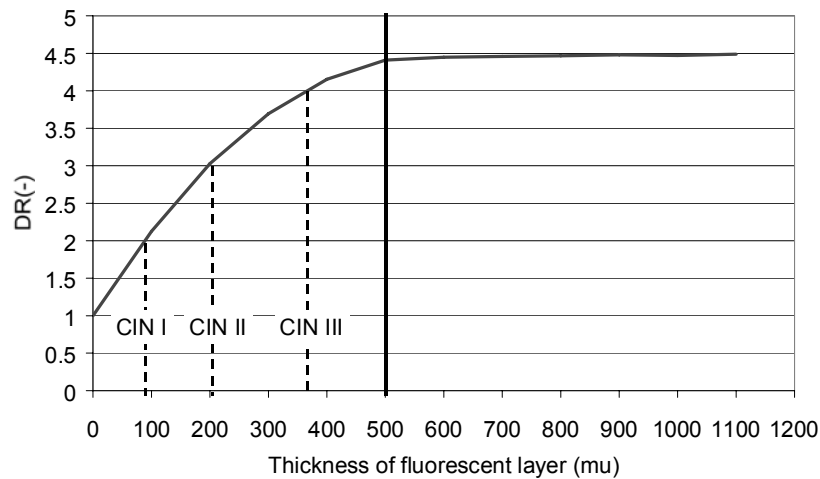


Fig. 4 Interrelationships of DR value, CIN grade and layer thickness as predicted by the Monte Carlo simulations.

Comparing these results to figure 3 is highly suggestive of linking the stage of the disease to the thickness of the tumour. However, the representation of the tumor progression by a perfect smooth walled cube is far from the realistic situation. Moreover, the optical properties of cervical tissue are not known and the values used in the Monte Carlo simulation were a best guess. However, the values and geometrical assumption used for the Monte Carlo simulation were used to investigate a concept that may give insight in the correlation between DR and stage of the disease. The validity of this concept does not depend on the exact values of the input parameters as long as the relative relations are reasonable.

Methodology

Tracing the location where the biopsy was taken on the fluorescence image was done by hand. Two different imaging devices were used and a topographical match between the two images was made based on visual cues and landmarks, like the portio and the edge of the cervix. Although a ‘double blind’ approach was used in this procedure, it remains the Achillesheel of the study. This problem could very simply be avoided by using an integrated device; performing both the photographic documentation and the DR imaging through the

same optics. Technically this should not be a major problem, and the preliminary results obtained in this study certainly warrant such a development.

Conclusions

DR fluorescence imaging of ALA induced PpIX of the cervix using our general purpose prototype appeared to be feasible. In 4 cases strongly localised fluorescent hotspots were observed at the location where clinically the disease was colposcopically visible. In the other cases the fluorescence showed a more diffuse multifocal image. The value of the DR determined at the site of biopsy correlated in a statistically significant way with the histopathologically determined stage of the disease. This suggests that non-invasive staging of CIN using this technique is feasible. We believe that the results of this study justify the development of a dedicated device that combines regular white light colposcopy with DR fluorescence imaging.

Acknowledgements

This work was funded by the Dutch Technology Foundation, grant no. AGN 443413 and the European Commission contract no. BMH4-CT 97-2260

References

1. Mitchell MF, Hittelman WN, Hong WK, Lotan R, Schottenfeld D. "The natural history of cervical intraepithelial neoplasia: an argument for intermediate endpoint biomarkers" *Cancer Epidemiol. Biomarkers Prev.* 1994; 3: 619-26
2. Koss LG. "The Papanicolaou test for cervical cancer detection. A triumph and a tragedy" *JAMA* 1989; 261: 737-43
3. Kurman RJ, Henson DE, Herbst AL, Noller KL, Schiffman MH. "Interim guidelines for management of abnormal cervical cytology. The 1992 National Cancer Institute Workshop" *JAMA* 1994; 271: 1866-9
4. Hornung R, Pham TH, Keefe KA, Berns MW, Tadir Y, Tromberg BJ. "Quantitative near-infrared spectroscopy of cervical dysplasia *in vivo*". *Human Reproduction* 1999; 14: 2908-2916.
5. DiSaia, Creasman. "Clinical Gynecologic Oncology" Mosby Year Book 1993, St. Louis, Missouri. 4th edition. Chapter 1.
6. Coppleson "Gynecologic Oncology. Fundamental Principles and Clinical Practice" Churchill Livingstone, Longman Group Limited New York 1981, volume 1; chapter 32-33.
7. Hopman E, Kenemans P, Helmerhorst Th. "Positive Predictive Rate of Colposcopic Examination of the Cervix Uteri: An Overview of Literature" *Obstet Gynecol Survey* 1998; 53: 97-106
8. Sellors J, Nieminen P, Vesterinen E, Paavonen J. "Observer Variability in the Scoring of Colpophotographs" *Obstet Gynecol* 1990; 76: 1006-1008
9. Ismail SM, Colclough AB, Dinnen JS, Eakins D, Evans DM, Gradwell E, O'Sullivan JP, Summerell JM, Newcombe RG. "Observer variation in histopathological diagnosis and grading of cervical intraepithelial neoplasia" *Br Med J* 1989; 298: 707-710
10. Buxton E, Luesley D, Shafi M, Rollason M. "Colposcopically directed punch biopsy: a potentially misleading investigation" *Br J Obstet Gynecol* 1991; 98: 1273-1276

11. Hopman E, Voorhorst F, Kenemans P, Meyer C, Helmerhorst Th. "Observer agreement on interpreting colposcopic images of CIN" *Gynecol Oncol* 1995; 58: 206-9
12. Mourant JR, Hielscher AH, Eick AA, Johnson TM, Freyer, J.P. "Evidence of intrinsic differences in the light scattering properties of tumorigenic and nontumorigenic cells" *Cancer* 1998; 84: 366-374
13. Perlemand LT, Backman V, Wallace M, Zonios G, Manoharan R, Nusrat A, Shields S, Seiler M, Lima C, Hamato T, Itzkan I, van Dam J, Crawford JM, Feld MS. "Observation of Periodic Fine Structure in Reflectance from Biological Tissue: A New Technique for Measuring Nuclear Size Distribution" *Phys Rev Letters* 1998; 80: 627-630.
14. Zonios G, Cothren R, Crawford JM, Fitzmaurice M, Manoharan R, van Dam J, Fels MS. "Spectral Pathology" *Ann N Y Acad Sci* 1998; 838: 108-115
15. Zonios G, Cothren R, Arendt JT, Wu HC, Van Dam J, Crawford JM, Manoharan R, Feld MS. "Morphological model of human colon tissue fluorescence" *IEEE Trans Biomed Eng* 1996 43: 113-22
16. Mitchell MF, Cantor SB, Ramanujam N, Tortolero-Luna G, Richards-Kortum R. "Fluorescence spectroscopy for diagnosis of squamous intraepithelial lesions of the cervix" *Obstet. Gynecol.* 1999; 93 462-70
17. Major A, Scott Rose G, Chapman C, Hiserath J, Tromberg BJ, Krasieva TB., Tadir Y, Haller U, DiSaia PJ, Berns MW. "In vivo fluorescence detection of ovarian cancer in the NuTu-19 epithelial ovarian cancer animal model using 5-aminolevulinic acid (ALA)" *Gyn Onc* 1996; 66: 122-32
18. Fehr MK, Wyss P, Tromberg BJ, Krasieva T, DiSaia PJ, Lin F, Tadir Y. "Selective photosensitizer localization in the human endometrium after intrauterine application of 5-aminolevulinic acid" *Am J Obstet Gynecol* 1996; 175: 1253-1259
19. Bedwell J, MacRobert AJ, Phillips P, Boan SG. "Fluorescence distribution and photodynamic effect of ALA- induced PpIX in the DMH rat colonic tumour model" *Br J Cancer* 1992; 65: 818-24
20. Pahernik SA, Botzlar A, Hillemanns P, Dellian M, Kirchstein M, Abels C, Korell M, Mueller-Hoecker J, Untch M, Goetz A E, "Pharmacokinetics and selectivity of aminolevulinic acid-induced porphyrin synthesis in patients with cervical intra-epithelial neoplasia", *Int. J. Cancer* 1998; 78: 310-314
21. Hillemans M, Weingandt H, Baumgartner R, Diebold J, Xiang W, Stepp H. "Photodetection of cervical intraepithelial neoplasia using 5 aminolevulinic acid induced porphyrin fluorescence" *Cancer* 2000 88: 2275-2282
22. Sinaasappel M, Sterenberg HJCM, "Quantification of the hematoporphyrin derivative by fluorescence measurement using dual-wavelength excitation and dual-wavelength detection", *Applied Optics* 1993; 32: 541-548
23. Sterenberg HJCM, Saarnak AE, Frank RGJ, Motamedi M. "Evaluation of spectroscopic correction techniques for in vivo fluorescence measurements on pigmented lesions". *J Photochem Photobiol* 1996; B35: 159-165
24. Bogaards A, Aalders MCG, Jongen AJL, Dekker E, Sterenberg HJCM. "Double Ratio fluorescence imaging for the detection of early superficial cancers" *Rev.Sci.Instr.* In press 2001
25. Keijzer M, Pickering JW, Prah SA, Welch AJ. "Light distributions in artery tissue: Monte Carlo simulations for finite-diameter laser beams" *Lasers Surg.Med.* 1989; 9: 148-154
26. Lucassen GW, Verkruysse W, Keijzer M, van Gemert MJ. "Light distributions in a port wine stain model containing multiple cylindrical and curved blood vessels" *Lasers Surg.Med.* 1996; 18: 345-357
27. Abdul-Karim FW, Fu YS, Reagan JW, Wentz WB. "Morphometric study of intraepithelial neoplasia of the uterine cervix", *Obstetrics & Gynecology.* 1982; 60: 210-214
28. M Keijzer, RR Richards-Kortum, SL Jacques, MS Feld. Fluorescence spectroscopy of turbid media: autofluorescence of the human aorta. *Appl. Opt.* 1989; 28: 4286-4292

Appendix I

For the calculations, we adjusted a Monte Carlo program, based on the code of Keijzer et al. (25) adapted by Lucassen et al. (26). The program uses a variance reduction method that is called survival weighting. The photons are transported through the medium with a certain weight. At each interaction, a fraction $\mu_a/(\mu_a+\mu_s)$ of the weight is deposited while the remaining fraction continues. The program was adjusted to enable fluorescence imaging simulation. First, the distribution of the excitation light is calculated using the source type and dimensions and the optical properties of the medium as input parameters. Light that is absorbed in the medium is scored in a (z, r) matrix that is used to assign weight to the fluorescence sources. A separate input file that contains the distribution of the fluorophores is used as source file for calculation of the fluorescent light distribution. The fraction of photons that escapes the medium from the top layer within a certain escape angle is scored in a matrix.

Relative fluorescence levels are determined for semi-infinite double layer geometries (representing the epithelial layer and the stromal layer) with embedded square geometries representing neoplastic areas. For the simulations, the thickness of the neoplastic area that originates at the boundary of the two layers was varied. The epithelial layer is first set to 0.5 mm (4). The 'tumor' progresses from the boundary between the two layers into the top layer (figures 5a-d) Some simulations were also performed with increasing thickness of the total epithelial layer from 0.5 to 1.3 mm (figures 5d to 5f) according to the findings of Abdul-Karim et al (27).

To our knowledge, the optical properties of cervical tissue in the blue light range are not known. For the simulations of the excitation light we have chosen an absorption coefficient and a scattering coefficient in the range as found by Keijzer et al. (28) of aorta tissue.

Excitation optical properties: μ_a : 15 cm⁻¹, μ_s 400 cm⁻¹.

Fluorescence optical properties were chosen to be in the range as found by Hornung et al.(4):

Layer 1 : μ_a : 0.15 cm⁻¹, μ_s 90 cm⁻¹, g: 0.9, n: 1.37, thickness: 500-1300 μ m.

Layer 2 : μ_a : 1 cm⁻¹, μ_s 150 cm⁻¹, g: 0.9, n:1.37 thickness: >5 cm.

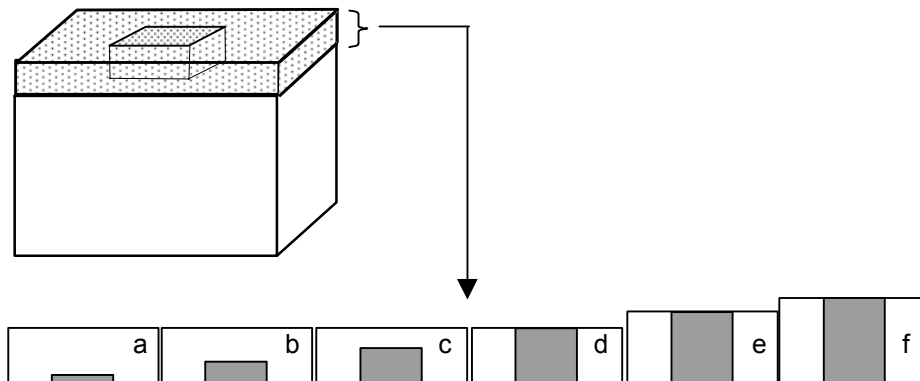


Fig. 5 The different configurations of the top layer with a progressing 'tumor' embedded.

Chapter 4

Increased Brain Tumor Resection Using Fluorescence Image Guidance in a Preclinical Model

A Bogaards^{1,2}

A Varma²

SP Collens¹

A Lin¹

A Giles¹

YX Yang¹

JM Bilbao³

L Lilge¹

PJ Muller²

BC Wilson¹

¹ Department of Medical Biophysics, Ontario Cancer Institute/University Health Network and University of Toronto, Toronto, Ontario, M5G 2M9, Canada

Division of ²Neurosurgery and ³Pathology, St. Michael's Hospital, Toronto, Ontario, M5B 1W8, Canada

Abstract

Background and Objectives: Fluorescence image-guided brain tumor resection is thought to assist neurosurgeons by visualizing those tumor margins that merge imperceptibly into normal brain tissue and, hence, are difficult to identify. We compared resection completeness and residual tumor, determined by histopathology, after white light resection (WLR) using an operating microscope versus additional fluorescence guided resection (FGR). **Study Design/Material and Methods:** We employed an intracranial VX2 tumor in a preclinical rabbit model and a fluorescence imaging/spectroscopy system, exciting and detecting the fluorescence of protoporphyrin IX induced endogenously by administering 5-aminolevulinic acid (ALA) at 4 h before surgery.

Results: Using FGR in addition to WLR significantly increased resection completeness by a factor 1.4 from 68% \pm 38% to 98% \pm 3.5%, and decreased the amount of residual tumor post resection by a factor 16 from 32% \pm 38% to 2.0% \pm 3.5% of the initial tumor volume.

Conclusions: Additional FGR increased completeness of resection and enabled more consistent resections between cases.

Introduction

The treatment of patients with high-grade gliomas remains a major challenge. The prognosis for these patients is poor, with a median survival time after diagnosis and treatment of less than 1 year (1,2). It has been suggested that the prognosis for these patients is linked to the completeness of tumor removal (3-6). A recent (7) study of 416 patients with glioblastoma multiforme indicated that resection of 89% of the tumor volume is necessary to improve survival, while resection of 98% or more resulted in a significant survival advantage of 4.2 months compared with a resection of less than 98%. However, such a high degree of tumor resection is often limited by the surgeon's ability to distinguish residual tumor tissue from surrounding brain tissue under conventional white light microscope illumination (8). Hence, methods enabling better intraoperative discrimination of viable tumor borders should be valuable.

Fluorescence imaging and spectroscopy using 5-aminolevulinic acid (ALA)-induced protoporphyrin IX (PpIX) is a potential technique to enhance contrast of viable tumor borders. Although administration of fluorescent markers to enhance contrast of malignant gliomas is not new (9-13), marking tumors with ALA is conceptually different from previous investigations, since ALA is not itself fluorescent but is metabolized into fluorescent PpIX by a number of malignant tumors *in situ* through enzymes of the heme-biosynthesis pathway (14). ALA-PpIX has been used widely, both for fluorescence diagnostics and photodynamic therapy (15). It may avoid problems that arise when a fluorescent marker is administered directly, such as leakage from the tumor into surrounding normal brain tissue (16). We have shown previously (17-20) that ALA-induced PpIX levels in normal brain tissue, especially white matter, are very low. Clinical and preclinical studies suggest that the resulting selectivity of ALA-PpIX in certain brain tumors (14,18-25) is a result of various factors. The low permeability of ALA at the blood-brain barrier (BBB) (26) reduces uptake in normal brain, whereas the compromised BBB in certain brain tumors is thought to permit selective ALA transport. Different activities of enzymes in the heme pathway have also been observed between tumor and normal tissues, which subsequently enable selective production of PpIX (27,28).

Stummer *et al.* recently introduced ALA-PpIX fluorescence imaging for intra-operative detection and resection of residual malignant glioma in 52 patients using an operating microscope adapted for fluorescence imaging (8,23). ALA was administered orally at a dose of 20 mg/kg at 3 h before induction of anesthesia and subsequent surgery. They observed that leaving “solidly fluorescing” tissue unresected had a negative influence on survival, whereas the prognosis of patients with residual “vague fluorescence” was not significantly different from that of patients in whom all solid fluorescent tissue was completely removed. Histologically, solidly fluorescing tissue was characterized mostly by coalescent tumor cells, whereas vaguely fluorescing tissue usually represented infiltrating tumor of intermediate or low cellular density. However, analysis of tumor biopsy specimens revealed infiltrating tumor also to be present beyond vaguely fluorescing tissue portions. This is an important study in demonstrating the potential of ALA-PpIX FGR, but is limited by the facts that only a single ALA dose and time interval were used and that the assessment of the tissue fluorescence was qualitative and subjective. We hypothesize that more quantitative fluorescence-based detection will further improve this technique and, therefore, we have developed a system for quantitative fluorescence imaging and image-guided point fluorescence spectroscopy. We have previously described this instrument and its initial demonstration for brain tumor fluorescence imaging in a pilot study in patients undergoing Photofrin-photodynamic therapy (12).

In the present study we have used this system for FGR in an intracranial tumor-bearing rabbit model, with the primary objective to compare completeness of tumor resection and residual tumor volume after white light resection *versus* additional ALA-PpIX fluorescence-guided resection. These values were quantified by histology of resected tissues and of the whole brain after resection. As a secondary objective, we determined the tumor-to-normal ratio in tissues resected under white light as well as in tissues resected under fluorescence guidance. These experiments were done using a fixed ALA dose and time interval, as a precursor to planned clinical and preclinical glioma resection studies to optimize these two factors.

Materials and Methods

Optical design of co-axial fluorescence imaging and spectroscopy system

The fluorescence imaging/spectroscopy system (12) is an optical illumination and detection platform specifically designed for open-field surgical procedures (Figure 1). Mounted on a suspension arm, this system illuminates the surgical field uniformly across the field of view with 405 nm light at 6 mWcm⁻², matching the main absorption peak of PpIX. The illumination light is integral to the camera and coaxial with the imaging pathway i.e. it is a “point and shoot” device. The fluorescence emitted from the tissue is imaged onto a CCD camera with 755×484 pixels at 10-bit dynamic range, that is mounted behind a filter wheel containing 5 different band pass filters (20nm FWHM) within the spectral range of 480-720 (Omega, Brattleboro, NJ). These have an OD of > 7 in the blue/UV range to reject the excitation light. The total acquisition time for 5 spectral images and a full fluorescence emission spectrum is approximately 30 s. To obtain a quantitative fluorescence image various image processing algorithms can be performed on these 5 spectral images, which also requires approximately 30 s. Also, the system is capable of white-light imaging using the normal operating room lighting, by combining the red, green and blue channels. The

working distance is 50 cm, which allows the camera head to be positioned while not impeding surgical access. The field of view is 3.3 cm×2.5 cm and the depth of focus is 2 cm, adequate for the geometry of open-field neurosurgery. The spatial resolution is 0.15 mm. A spectrograph, integrated with the fluorescence imaging system, performs non-contact fluorescence spectroscopy over a small area (diameter ~ 0.6 mm) within the surgical field, at locations selected in the image field-of-view by the operator. The positioning of the system is similar to that of conventional operating microscopes with manual suspension arms, although more time consuming in the present prototype configuration.

Tumor propagation and induction

This study was approved by the Animal Care Committee of St. Michael's Hospital, Toronto (ACC512). We elected to use rabbits in this first animal study, since this allows fairly large tumors (5-10mm diameter), which simplifies the surgical procedures compared to smaller animal models. Since there is no glioma model in the rabbit, we used the VX2 carcinoma, which has similarities in its growth characteristics to primary brain tumors, such as microinvasion, pseudo

palisading, growth along the blood vessels and in perivascular spaces, and breakdown of the blood-brain barrier within the tumor and in brain adjacent to tumor (19). We have reported the use of this model previously for studies of ALA-PpIX distribution and photodynamic therapy response (18-20). Male SPF New Zealand white rabbits (3.3-3.8 kg) (Charles River, Montreal, PQ, Canada) were used to propagate the tumor cell line by injecting a suspension of 10^6 VX2 cells in 1 ml at 3 locations into the left adductor magnus muscle. These animals were euthanized 14–25 days post induction by *i.v.* injection of T61 (Intervet, Whitby, ON, Canada). The tumors were approximately 1 cm diameter when harvested and the VX2 cells were extracted using a strainer. Subsequently, the cells were counted in phosphate buffered saline (PBS) with a haemocytometer and used within 2 h. For intracranial induction the animals were anaesthetized with a mixture of 5mg/kg Xylazine (Bayer, Germany) and 50mg/kg Ketamine (de Wyet-Ayerst, Guelph, ON, Canada) and the site was shaved and swabbed with betadine (Purdue Frederick, Pickering, ON, Canada). A 2-3 cm midline incision was made, the scalp reflected and the cranium exposed. Using a 1.5 mm diameter drill, a burr hole was performed over the right hemisphere, anterior to the coronal suture and 5 mm to the right of the bregma, leaving the dura intact. A 100µl Hamilton syringe was introduced to a depth of 3 mm beneath the dura and 10^5 VX2 cells in 50µl PBS were

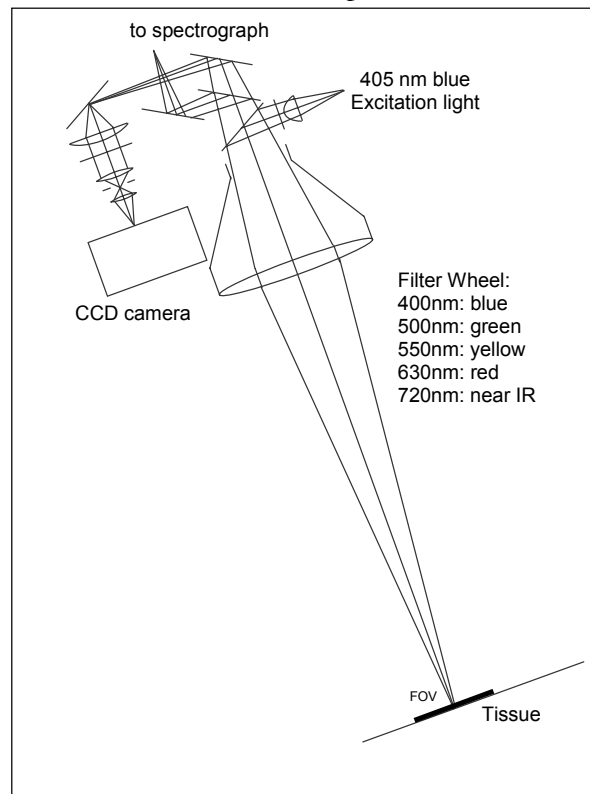


Fig. 1 Optical design of the co-axial multi-spectral fluorescence imaging and spectroscopy system, the bar indicates the field of view (FOV) of the camera: details are found in reference 12.

inoculated intracerebrally, over a period of 2-3 minutes with low pressure to avoid trauma. Bone wax was used to close the burr hole and the incision was then closed with sutures. Buprenex (Reckitt & Colman Ltd., Hull, England) was administered subcutaneous for analgesia every 8 h for the first 24 h post implantation. Fourteen animals received VX2 cells and 3 animals were injected with saline and used as controls. From previous studies, this induction procedure results in tumors of 5-10 mm diameter in 2 weeks.

Resection procedure

Surgery was performed 14 days post VX2 induction and 4 h post *i.v.* injection of 20 mg/kg ALA in hydrochloride form (Levulan, DUSA Pharmaceuticals, Valhalla, NY, USA) as a solution in PBS buffered to pH 6.2-6.8. For surgery the animals were brought under general anesthesia by subcutaneous Xylazine/Ketamine injection with Buprenex used for systemic analgesia. The eyes were lubricated with Lacri-Lube (Allergan Inc., Markham, ON, Canada) and closed with tape to prevent exposure to the operating and blue excitation light. The heart rate and oxygen saturation were monitored with a pulse oximeter (Model 8500V; Nonin Medical, Plymouth, MN, USA). The head was fixed in position in a stereotaxic frame with a rabbit adapter (Model 900; David Kopf Instr., Tujunga, CA, USA). The scalp was shaved, betadine was applied to the surgical site, which was covered with a sterile keyhole drape, and the incision site was injected with 1-2 cc of 2% Xylocaine (Astra Zeneca, Mississauga, ON, Canada). A 2-4 cm incision was made in the scalp along the mid-line and held open with a self-retaining retractor. A craniotomy was performed using a small hand-held orthopedic drill of 1.5mm diameter, which was continuously cooled with sterile betadine saline solution. Gentle suction was used to remove irrigating fluid and bone dust. The bone flap was gently elevated with a periosteal elevator, aiming to keep the entire dura intact. Once the bone flap was removed, both left and right hemispheres were exposed and the dura was cut using microsurgery scissors and forceps.



Fig. 2 *Surgical experimental setup showing 1) the fluorescence imaging system, 2) the operating microscope and 3) the rabbit covered with a sterile keyhole drape.*

White light resection

The tumor was located and removed under white light illumination using an operating microscope. Bipolar coagulation was used as required. Saline irrigation and suction were used to keep the surgical site clean and a micro pituitary forceps with a 2 mm tip to was used to remove the tumor tissue. Care was taken to minimize removal of normal brain. WLR

was considered complete once no tumor tissue was visible to the neurosurgeon using the operating microscope under white light illumination.

Fluorescence guided resection

Once WLR was completed, point fluorescence spectra and images were acquired in the surgical cavity (Figure 2). Since the fluorescence signal is weak, FGR was performed with the operating light switched off and the ambient light was subdued. We aimed to resect (and save) all fluorescing tissues. FGR was considered complete once the fluorescence intensity throughout the surgical cavity had decreased to the background level of the surrounding brain. Since all resected tissues were saved for histology, care was taken to remove tissues only by biopsy forceps and not by suction. Immediately following completion of tumor resection the animals were euthanized by *i.v.* T61 injection and the whole brain was removed intact. White light resected tissues, fluorescence guided resected tissues and whole brain were saved in separate, light-tight containers and immediately snap frozen in liquid nitrogen and stored until further use at -70°C .

Fluorescence quantification

In the present study, the full quantitative capabilities of the fluorescence imaging system could not be exploited, since the acquisition time and image processing time of approximately 60 s allowed the surgical cavity to fill with blood, obstructing the blue excitation and red fluorescence light. Hence, we were forced to obtain fluorescence images in real-time (30 frames per s), by using only the red fluorescence channel (640nm, 20nm FWHM), combined with suction to clear the surgical site of blood. As a result, we obtained relatively poor anatomical definition. Also, although the camera gain, integration time, excitation power and focal distance were held constant, the fluorescence signal was only partially quantitative, since other factors, such as the tissue optical properties, autofluorescence and background light, were not determined.

Histopathology and volume calculations

Serial sections of 5 μm thickness were prepared at 0.5 mm intervals and stained with Hematoxylin & Eosin (H&E). Slides were digitized using a stereomicroscope (Model MZFLIII; Leica, Germany) with a digital camera (DC300F), using 1-10X objectives. For consistency, areas of normal and tumor tissue were delineated by a single investigator (SPC) on these low magnification images using Image Pro-Plus software (Media Cybernetics, Silver Spring, MD, USA), while observing the original slide under a microscope (Optiphot; Nikon, Japan) at higher magnifications using 10-40X objectives. This investigator was trained by a neuro histopathologist (GMB), who verified the delineated region of tumor and normal tissue on every 7th slide. Both investigators were blinded to the resections. Pixel size calibration allowed calculation of the cross-sectional area of each region, and the separation between sections then enabled the volumes of tumor and normal tissues to be calculated. The percentage of residual tumor after white light resection, RT_w , after fluorescence resection, RT_f , and after white light *plus* fluorescence guided resection, RT_{w+f} , were defined as,

$$RT_w = \frac{T_f + T_{wb}}{T_w + T_f + T_{wb}} * 100\%, \quad RT_f = \frac{T_f}{T_w + T_f + T_{wb}} * 100\%, \quad RT_{w+f} = \frac{T_{wb}}{T_w + T_f + T_{wb}} * 100\%$$

, where T_w , T_f and T_{wb} are, respectively, the tumor volume in the white light resected tissues, in the fluorescence resected tissues and in the whole brain at the end of the procedure. We

note that, using blue excitation light and given the known camera sensitivity, the effective depth for fluorescence detection below the tissue surface is likely less than 0.5mm (12). Hence, in the calculation of T_{wb} we did not include tumor located at a distance more than 0.5mm away from the surgical cavity. The percentage of tumor resection completeness in the whole brain after white light resection, TRC_w , fluorescence resection, TRC_f , and white light plus fluorescence resection, TRC_{w+f} were defined here as, $TRC_{sub} = 100\% - RT_{sub}$. In order to compare the completeness of tumor resection completeness after *WLR* and *WLR+FGR*, we performed 1-sample t-tests on the groups RT_w vs. RT_{w+f} and TRC_w vs TRC_{w+f}

Results

White light resection

Under white light, the tumor appeared greyish white, that was distinct from surrounding white matter, often with areas of hemorrhage and cystic necrosis. All the abnormal appearing tissue was removed until only normal white matter was observed in the tumor bed. In 11 of 14 animals the tumor was visible under white light illumination, whereas in 3 animals the tumor was not visible under white light but a small region of fluorescence was found and resected.

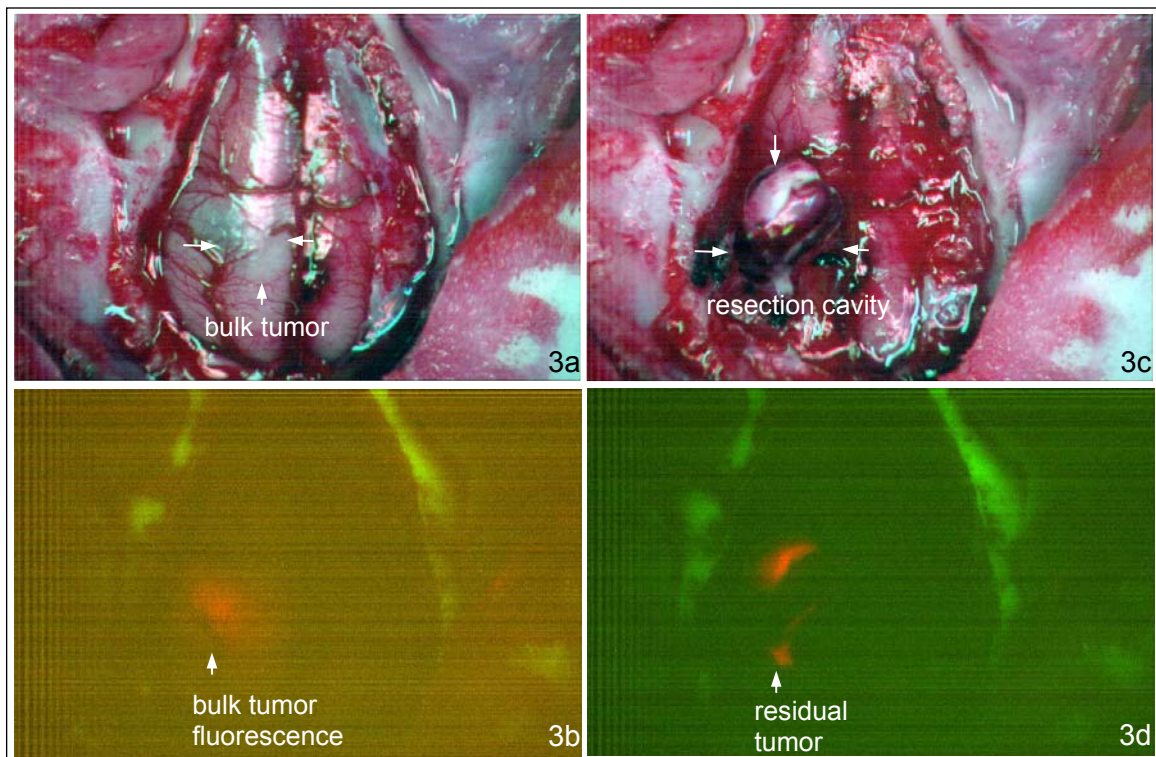


Figure 3. Example of white light (a, c) and fluorescence (b, d) imaging in VX2 rabbit brain. (a) shows the brain surface before resection, with visible, white-appearing VX2 tumor. (b) shows the corresponding fluorescence image, where the bulk tumor fluoresces in red. (c) and (d) show the the surgical cavity after WLR. The bone fluoresces in the green, which was used as overlay to provide image orientation.

Fluorescence guided resection

No fluorescence was detected in the 3 non-tumor bearing control animals while resecting up to 7 mm beneath the dura, which was deeper than in the tumor-bearing animals. False positive fluorescence was consistently observed in choroids plexus and optical nerves. PpIX fluorescence was present in all 14 tumor-bearing animals, verified by point spectroscopy that showed the characteristic PpIX peaks at 635 and 704 nm. A typical fluorescence image is illustrated in Figure 3. In 2 animals fluorescence resection was not completed, since the tumor invaded deeply into the brain and complete resection would have been fatal.

Histopathology and volume calculations

Typical H&E stained sections are illustrated in Figures 4-8. The morphology of the VX2 tumor is seen in Figure 4, showing the invasive characteristics, with the proliferating tumor margin showing protrusions, and distant tumor nests extending in the normal brain. Figure 5 shows a section of WLR tissue, which is mostly characterized by a high density of tumor cell and a region of normal brain adjacent to tumor. Figure 6 illustrates a section of FGR tissue, with a small area of infiltrative tumor cells and a larger area of brain adjacent to tumor. In 2 of the 14 animals where FGR was incomplete, relatively large volumes of residual tumor were present. In 7 other animals, only small volumes of residual tumor were found inside the surgical cavity (Figure 7). In the remaining 5 animals no residual tumor could be found post FGR. In several animals, sections of the whole brain post FGR revealed tumor cells more than 0.5mm away from the surgical cavity and, therefore, beyond the detection depth of this device (12) (Figure 8); in some cases tumor invaded the ventricles and choroid plexus and extended to the opposite hemisphere.

Volumes of resected tumor tissue and resected brain adjacent to tumor were calculated and the averages and range of values are listed in Table 1. The tumor-to-normal ratio of white light resected tissues was calculated for each animal, and gave a mean of $47\% \pm 31\%$, i.e. almost half of the resected tissue was tumor. The corresponding value for FGR tissue was $12\% \pm 15\%$. The percentage of tumor resection completeness and residual tumor were then calculated and are listed in Table 2 and a scatter plot of the residual tumor is shown in figure 9. Using FGR in addition to WLR significantly increased completeness of tumor resection by an average factor 1.4, from $68\% \pm 38\%$ to $98\% \pm 3.5\%$ ($p=0.010$), while the residual tumor in the whole brain decreased by an average factor of 16-fold from $32\% \pm 38\%$ to $2.0\% \pm 3.5\%$ of the total tumor volume ($p=0.010$). These values include 3 animals where the tumor was not visible using white light but had a small region of fluorescence. It could be argued that this situation will not occur in patients, and that these animals should be excluded. Doing so, gave an increase in completeness of tumor resection by a factor of 1.1 from $86\% \pm 12\%$ to $98\% \pm 3.8\%$ ($p=0.008$), and a decrease in residual tumor in whole brain by an average factor of 7 from $14\% \pm 12\%$ to $2.0\% \pm 3.8\%$ ($p=0.008$). However, including these 3 animals in the also supports the hypothesis that more tumor can be resected under fluorescence guidance compared with white light visualization alone.

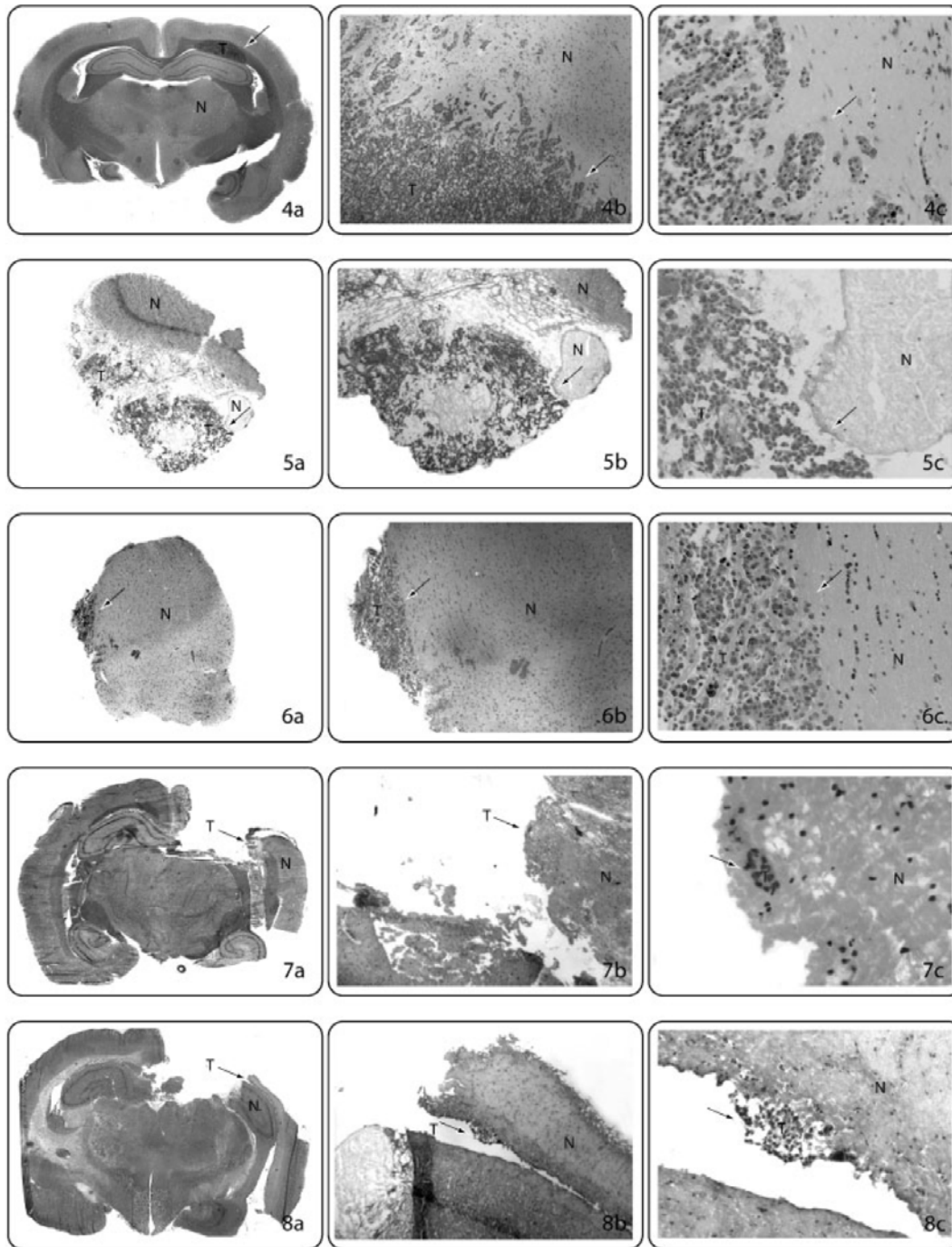


Fig. 4-8 (4) Coronal section showing VX2 tumor (T) in the left hemisphere proliferating into the normal (N) brain, and distant tumor cell nests. The arrow indicates the same point in each image using a) 1X, b) 2.5X and c) 20X objectives. The same convention is used also in Figures 5-8. (5) Section of WLR tissue with areas of tumor and normal tissue. (6) Section of FGR tissue with a small area of tumor and a larger area of normal brain. (7) the resection cavity after WLR and additional FGR. Small amounts of residual tumor were found at the surface of the cavity. These can be considered False Negative for fluorescence detection. (8) The resection cavity after WLR and FGR. Here, small amounts of residual tumor were found beyond the surface of the resection cavity, not be detectable by fluorescence imaging, since the effective depth of the blue-light excitation below the exposed tissue surface is likely less than 0.5 mm. (12)

Discussion

Increased brain tumor resection

The above results show that fluorescence image-guided resection using ALA-induced PpIX enables identification and resection of significantly more tumor than can be achieved by white-light resection alone. The high degree of tumor resection completeness achieved with WLR + FGR ($98\% \pm 3.5\%$) is close to the value of $>98\%$ that has been associated clinically with improved survival. (7) The very large variance in tumor resection completeness by white light, as evidenced in the standard deviation around the mean ($68 \pm 38\%$), is markedly reduced using additional fluorescence guidance ($98\% \pm 3.5\%$), even although there was a large range of initial tumor sizes and residual tumor after WLR. This suggests that fluorescence guidance not only increases completeness of resection, but also enables more consistent resections between cases.

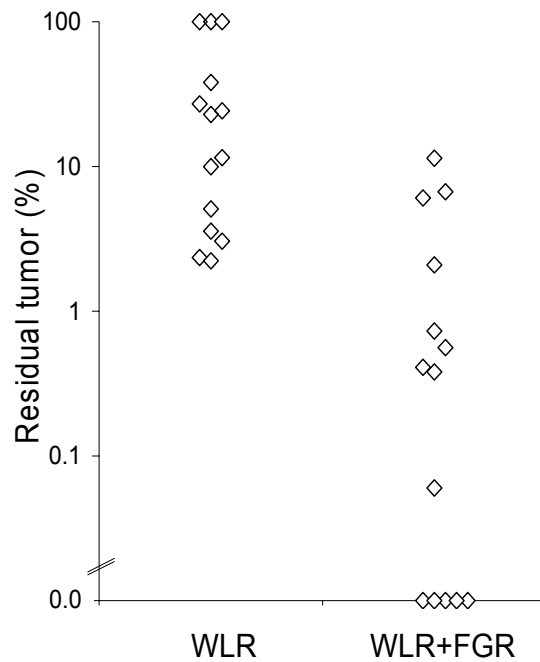


Fig. 9 Scatter plot of the percentage of residual tumor using WLR only versus WLR + FGR. In 5 animals no residual tumor was found histologically after WLR + FGR.

Resection of normal brain

This study differs from other published reports of FGR, in that we saved all resected tissues for histology to determine whether normal brain tissue is also removed during FGR. We found a significant amount of normal brain adjacent to tumor was also resected. There are two main potential explanations for this. The first is that there is detectable ALA-PpIX fluorescing normal tissue. This is unlikely, based on previous studies that have shown very low ALA-PpIX levels in normal brain tissues with intact blood-brain barrier (17-20,25), even at high ALA administered doses. A more likely cause is a scaling artifact as a result of the

resection technique, where a micro pituitary forceps with a 2 mm tip was used to resect tissues. This is fairly large relative to the tumor size and the rabbit brain, and may have resulted in over resection. This should be much less of a problem in patients, where the resection instruments are relatively small compared to the tumor size. Clinically, more accurate resection techniques could also be used, such as gentle suction and ultrasonic aspiration, which could not be used here because all resected tissues had to be saved for histology. Nevertheless, resecting normal brain tissue adjacent to tumor may be hard to avoid completely due to tumor infiltration.

Table 1. Mean \pm standard deviation and range of resected tissue volumes, the fraction of tumor, and the tumor-to-normal ratio for WLR and FGR tissues, based on H&E stained serial sections.

	White light resected tissues			Fluorescence resected tissues			Whole Brain
	Resected Volume (mm ³)	T _w Tumor Volume (mm ³)	T/N Ratio (%)	Resected Volume (mm ³)	T _f Tumor Volume (mm ³)	T/N Ratio (%)	T _{wb} Residual Tumor Volume (mm ³)
Mean	72.0 \pm 58.6	47.8 \pm 45.4	47 \pm 31	104.7 \pm 101	8.4 \pm 12.1	12 \pm 15	2.2 \pm 6.4
Range	0.0-176	0.0-162	0-92	5.6-395	1.0-41.6	1-14	0.0-24.4

Table 2. Mean \pm standard deviation and range of Tumor Resection Completeness (TRC) and Residual Tumor (RT) for respectively white light resection, fluorescence resection and the combination.

	Tumor Resection Completeness (%)			Residual Tumor (%)		
	TRC _w	TRC _f	TRC _{w+f}	RT _w	RT _f	RT _{w+f}
Mean	67.9 \pm 38.4	30.1 \pm 38.1	98.0 \pm 3.5	32.1 \pm 38.4	69.9 \pm 38.1	2.0 \pm 3.5
Range	0.0-97.8	1.8-99.3	88.6-100.0	2.2-100.0	0.0-98.2	0.0-11.4

Fluorescence quantification

Based on this study, translating FGR to the clinic will require further investigation into the extent of PpIX fluorescence in normal brain tissue (both in absolute terms and relative to tissue autofluorescence at the excitation and emission wavelengths) and, hence, the extent of normal tissue removal (False Positives). It will be critical to quantify the fluorescence signal in order to minimize 1.) subjective fluorescence image interpretation, which could result in inter-observer variations, and, 2.) artifacts due to variations in tissue optical properties (e.g. local blood absorption) that may not be related to malignancy (29). In the present study, the full quantitative capabilities of the imaging system could not be exploited, as explained above, so that we obtained relatively poor anatomical definition and the fluorescence signal was only partially quantitative. This is less of a problem in clinical use because of the larger resection cavity and more complete hemostasis (12).

Limitations of the FGR technique

In the majority of animals complete tumor resection was not achieved due to small tumor cell nests (2% \pm 3.5% of the total tumor volume) in the the surgical cavity that were undetectable by fluorescence. These could be considered as False Negatives for this particular device, ALA dose and administration time. Also, in some cases where tumor invaded beyond the surgical cavity, this would not be detectable by fluorescence imaging of

the cavity, since the effective tissue sampling depth of the blue-light excitation below the exposed tissue surface is less than 0.5 mm (12). This suggests that 1.) more sensitive fluorescence detection could be advantageous, and, 2.) an adjuvant therapy applied post resection capable of targeting small tumor nests and invasive tumor, such as photodynamic therapy, may be of further benefit, which is the focus of ongoing studies (30,31).

Limitations of the present preclinical study

Similar to the ALA doses and time interval used in clinical work by Stummer *et al* (8,23), this preclinical study was performed at fixed ALA dose (20mg/kg) and fixed time interval (4h) between ALA administration and surgery, which are not necessarily optimal. These parameters will likely affect the sensitivity and specificity of the fluorescence detection in tumor tissue. High sensitivity is required in order to minimize the residual tumor post resection, while high specificity will allow the surgeon to avoid removing excessive amounts of normal brain tissue. However, the latter may be less critical, since clinical judgment will always prevail in determining if tissue, whether fluorescent or not, can be removed safely. Residual tumor was determined accurately in this study since the whole brain was removed, cut in serial sections and examined by histology. Clinically, post operative MR images are normally used to determine residual tumor. Hence, it will be important to investigate the relationship between the fluorescence signal and MR contrast of residual tumor. We will address these issues in future clinical trials by optimizing the ALA dose and administration time and investigating the correlation between the fluorescence signal and MR contrast in glioma patients.

Future technology development

In effort to address the above limitations several technological improvements are being considered as part of our ongoing work. More sensitive ccd detectors with higher dynamic range have recently become available that use on the chip amplification. Multiple detectors could allow simultaneous acquisition of multiple spectral windows, avoiding the long acquisition times as is the case with our current filter wheel and a single detector. The used excitation irradiance in this study was low (6 mWcm^{-2}). With existing Xenon arc lamps and improved optics this can be increased by a factor 10 or more. An other option to increase excitation irradiance is using raster scanning with a relatively high power pencil beam (32). Depth resolution could be improved by utilizing longer excitation wavelengths and raster scanning, considering both single and multi photon excitation (33), which could then allow depth tomography. The fluorescence signal may be further increased by utilizing fluorophores and/or nanocrystals selected for high fluorescence yield, which might then be labeled to antibodies for tumor selective targeting (34,35). In terms of quantitation it would be advantageous to obtain fluorescence signal that depends only on the local fluorophore concentration. Several spectroscopic methods suggested in the literature have been evaluated by Sterenberg *et al*, (29) using multiple excitation and/or detection wavelengths, which could also be utilized for imaging. Currently, we are developing fluorescence imaging systems considering the above.

Acknowledgements

This investigation was supported by grant NIH grant CA 43892. Instrument development was supported by Photonics Research Ontario. Statistical advice of Dr. Judith Abrahams is gratefully acknowledged. DUSA Pharmaceuticals NY kindly provided the ALA. Microscopes, image processing software and support were available through the Advanced Optical Microscope Facility (AOMF) at the Ontario Cancer Institute, supported by the Canadian Foundation for Innovation.

References

1. Shapiro WR, Green SB, Burger PC, Mahaley MS, Jr., Selker RG, VanGilder JC, Robertson JT, Ransohoff J, Mealey J, Jr., Strike TA, et al. Randomized trial of three chemotherapy regimens and two radiotherapy regimens and two radiotherapy regimens in postoperative treatment of malignant glioma. Brain Tumor Cooperative Group Trial 8001. *J Neurosurg* 1989; 71(1):1-9.
2. Walker MD, Green SB, Byar DP, Alexander E, Jr., Batzdorf U, Brooks WH, Hunt WE, MacCarty CS, Mahaley MS, Jr., Mealey J, Jr., Owens G, Ransohoff J, 2nd, Robertson JT, Shapiro WR, Smith KR, Jr., Wilson CB, Strike TA. Randomized comparisons of radiotherapy and nitrosoureas for the treatment of malignant glioma after surgery. *N Engl J Med* 1980; 303(23):1323-1329.
3. Rostomily RC, Spence AM, Duong D, McCormick K, Bland M, Berger MS. Multimodality management of recurrent adult malignant gliomas: results of a phase II multiagent chemotherapy study and analysis of cytoreductive surgery. *Neurosurg* 1994; 35(3):378-388; discussion 388.
4. Nitta T, Sato K. Prognostic implications of the extent of surgical resection in patients with intracranial malignant gliomas. *Cancer* 1995; 75(11):2727-2731.
5. Devaux BC, O'Fallon JR, Kelly PJ. Resection, biopsy, and survival in malignant glial neoplasms. A retrospective study of clinical parameters, therapy, and outcome. *J Neurosurg* 1993; 78(5):767-775.
6. Yoshida J, Kajita Y, Wakabayashi T, Sugita K. Long-term follow-up results of 175 patients with malignant glioma: importance of radical tumour resection and postoperative adjuvant therapy with interferon, ACNU and radiation. *Acta Neurochir* 1994; 127(1-2):55-59.
7. Lacroix M, Abi-Said D, Fourney DR, Gokaslan ZL, Shi W, DeMonte F, Lang FF, McCutcheon IE, Hassenbush SJ, Holland E, Hess KM, C. , D. M, Sawaya R. A multivariate analysis of 416 patients with glioblastoma multiforme: prognosis, extend of resection and survival. *J Neurosurg* 2001; 95(August):190-198.
8. Stummer W, Stepp H, Moller G, Ehrhardt A, Leonhard M, Reulen HJ. Technical principles for protoporphyrin-IX-fluorescence guided microsurgical resection of malignant glioma tissue. *Acta Neurochir* 1998; 140(10):995-1000.
9. Murray KJ. Improved surgical resection of human brain tumors: Part I. A preliminary study. *Surg Neurol* 1982; 17(5):316-319.
10. Kremer P, Wunder A, Sinn H, Haase T, Rheinwald M, Zillmann U, Albert FK, Kunze S. Laser-induced fluorescence detection of malignant gliomas using fluorescein-labeled serum albumin: experimental and preliminary clinical results. *Neurolog Res* 2000; 22(5):481-489.
11. Poon WS, Schomacker KT, Deutsch TF, Martuza RL. Laser-induced fluorescence: experimental intraoperative delineation of tumor resection margins. *J Neurosurg* 1992; 76(4):679-686.

12. Yang VX, Muller PJ, Herman P, Wilson BC. A multispectral fluorescence imaging system: design and initial clinical tests in intra-operative Photofrin-photodynamic therapy of brain tumors. *Lasers Surg Med* 2003; 32(3):224-232.
13. Shinoda J, Yano H, Yoshimura S, Okumura A, Kaku Y, Iwama T, Sakai N. Fluorescence-guided resection of glioblastoma multiforme by using high-dose fluorescein sodium. Technical note. *J Neurosurg* 2003; 99(3):597-603.
14. Hebeda KM, Saarnak AE, Olivo M, Sterenborg HJ, Wolbers JG. 5-Aminolevulinic acid induced endogenous porphyrin fluorescence in 9L and C6 brain tumours and in the normal rat brain. *Acta Neurochir* 1998; 140(5):503-512.
15. Kely CJ, Brown NJ, Reed MWR, Ackroyd R. The use of 5-aminolaevulinic acid as a photosensitiser in photodynamic therapy and photodiagnosis. *Photochem Photobiol Sci* 2002; 3:149-224.
16. Stummer W, Gotz C, Hassan A, Heimann A, Kempfski O. Kinetics of Photofrin II in perifocal brain edema. *Neurosurg* 1993; 33(6):1075-1081; discussion 1081-1072.
17. Olivo M, Wilson BC. Mapping ALA-induced PPIX fluorescence in normal brain and brain tumour using confocal fluorescence microscopy. submitted to *Int J Cancer* 2004.
18. Lilge L, Olivo MC, Schatz SW, MaGuire JA, Patterson MS, Wilson BC. The sensitivity of normal brain and intracranially implanted VX2 tumour to interstitial photodynamic therapy. *Br J Cancer* 1996; 73(3):332-343.
19. Lilge L, Portnoy M, Wilson BC. Apoptosis induced in vivo by photodynamic therapy in normal brain and intracranial tumour tissue. *Br J Cancer* 2000; 83(8):1110-1117.
20. Lilge L, Wilson BC. Photodynamic therapy of intracranial tissues: a preclinical comparative study of four different photosensitizers. *J Clin Laser Med Surg* 1998; 16(2):81-91.
21. Olzowy B, Hundt CS, Stocker S, Bise K, Reulen HJ, Stummer W. Photoirradiation therapy of experimental malignant glioma with 5-aminolevulinic acid. *J Neurosurg* 2002; 97(4):970-976.
22. Stummer W, Ennis SR, Betz AL, Keep RF. In vitro and in vivo porphyrin accumulation by C6 glioma cells after exposure to 5-aminolevulinic acid. *Cerebral Blood Flow Metab* 1999; 19(1):79-86.
23. Stummer W, Novotny A, Med CN, Stepp H, Goetz C, Bise K, Reulen HJ. Fluorescence-guided resection of glioblastoma multiforme by using 5-aminolevulinic acid-induced porphyrins: a prospective study in 52 consecutive patients. *J Neurosurg* 2000; 93(6):1003-1013.
24. Moan J, Ma LW, Juzeniene A, Iani V, Juzenas P, Apricena F, Peng Q. Pharmacology of protoporphyrin IX in nude mice after application of ALA and ALA esters. *Int J Cancer* 2003; 103(1):132-135.
25. Wu SM, Ren QG, Zhou MO, Peng Q, Chen JY. Protoporphyrin IX production and its photodynamic effects on glioma cells, neuroblastoma cells and normal cerebellar granule cells in vitro with 5-aminolevulinic acid and its hexylester. *Cancer Lett* 2003; 200(2):123-131.
26. Ennis SR, Novotny A, Xiang J, Shaku P, Masada T, Stummer W, Smith DE, Keep RF. Transport of 5-aminolevulinic acid between blood and brain. *Brain Res* 2003; 959(2):226-234.
27. Peng Q, Warloe T, Berg K, Moan J, Kongshaug M, Giercksky KE, Nesland JM. 5-Aminolevulinic acid-based photodynamic therapy. Clinical research and future challenges. *Cancer* 1997; 79(12):2282-2308.
28. Peng Q, Berg K, Moan J, Kongshaug M, Nesland JM. 5-Aminolevulinic acid-based photodynamic therapy: principles and experimental research. *Photochem Photobiol* 1996; 65(2):235-251.
29. Sterenborg HJ, Saarnak AE, Frank R, Motamedi M. Evaluation of spectral correction techniques for fluorescence measurements on pigmented lesions in vivo. *J Photochem Photobiol B* 1996; 35(3):159-165.

30. Bisland SL, Lilge LD, Lin A, C. WB. Metronomic photodynamic therapy (mPDT) for intracranial neoplasm: physiological, biological, and dosimetry considerations. *Proc SPIE* 2003; 5142:9-17.
31. Wilson BC, Bisland SK, Bogaards A, Lin A, Moriyama EH, Zhang K, Lilge LD. Metronomic photodynamic therapy (mPDT): concepts and technical feasibility in brain tumor. *Proc SPIE* 2003; 4952:23-31.
32. Pogue BW, Gibbs SL, Chen B, Savellano M. Fluorescence imaging in vivo: raster scanned point-source imaging provides more accurate quantification than broad beam geometries. *Technol Cancer Res Treat* 2004; 3(1):15-21.
33. Zipfel WR, Williams RM, Webb WW. Nonlinear magic: multiphoton microscopy in the biosciences. *Nat Biotechnol* 2003; 21(11):1369-1377.
34. Akerman ME, Chan WC, Laakkonen P, Bhatia SN, Ruoslahti E. Nanocrystal targeting in vivo. *Proc Natl Acad Sci U S A* 2002; 99(20):12617-12621.
35. Chan WC, Maxwell DJ, Gao X, Bailey RE, Han M, Nie S. Luminescent quantum dots for multiplexed biological detection and imaging. *Curr Opin Biotechnol* 2002; 13(1):40-46.

Chapter 5

Fluorescence image-guided brain tumour resection with adjuvant metronomic photodynamic therapy: pre-clinical model and technology development

A Bogaards¹
A Varma³
K Zhang²
D Zach²
L Lilge¹
PJ Muller³
BC Wilson^{1,2}

*Department of Medical Biophysics¹, and Laboratory of Applied Biophotonics², Ontario Cancer Institute/University Health Network and University of Toronto, Toronto, Ontario, M5G 2M9, Canada
Division of Neurosurgery³ St. Michael's Hospital, Toronto, Ontario, M5B 1W8, Canada*

Abstract

Fluorescence-guided resection (FGR) and photodynamic therapy (PDT) have previously been investigated separately with the objectives, respectively, of increasing the extent of tumour resection and of selectively destroying residual tumour post resection. Both techniques have demonstrated trends towards improved survival, pre-clinically and clinically. We hypothesize that combining these techniques will further delay tumour re-growth. In order to demonstrate technical feasibility, we here evaluate fluorescence imaging and PDT treatment techniques in a specific intracranial tumour model.

The model was the VX2 carcinoma grown by injection of tumour cells into the normal rabbit brain. An operating microscope was used for white light imaging and a custom-built fluorescence imaging system with co-axial excitation and detection was used for FGR. PDT treatment light was applied by intracranially-implanted light emitting diodes (LED). The fluorescent photosensitizer used for both FGR and PDT was ALA-induced PpIX. For PDT, ALA (100mg/kg) and low light doses (15 and 30J) were administered over extended periods, which we refer to as metronomic PDT (mPDT).

18 tumour bearing rabbits were divided equally into 3 groups: controls (no resection); FGR; and FGR followed by mPDT. Histological whole brain sections (H&E stain) showed primary and recurrent tumours. No bacteriological infections were found by Gram staining. Selective tumour cell death through mPDT-induced apoptosis was demonstrated by TUNEL stain. These results demonstrate that the combined treatment is technically feasible and this model is a candidate to evaluate it. Further optimization of mPDT treatment parameters (drug/light dose rates) is required to improve survival.

Introduction

Protoporphyrin IX (PpIX) can be used as both contrast agent for fluorescence-guided resection (FGR) (1) and as a photosensitizer for photodynamic therapy (PDT) (2) of brain tumours. After systemic administration of 5-aminolevulinic acid (ALA) and suitable time interval (typically 2-6h) ALA is selectively metabolized into protoporphyrin IX (PpIX) by certain brain tumours (3-10). PpIX is fluorescent, with characteristic red emission peaks at 635 and 704 nm under UV/blue light excitation. When photoactivated it can also generate short-lived cytotoxic free oxygen radicals, namely singlet oxygen (11). Hence, ALA-induced PpIX is used for a variety of both photodiagnostic and phototherapeutic applications.

In particular, PpIX fluorescence has been investigated for detection and image-guided resection of brain tumours (1). In a preclinical model, we recently demonstrated that fluorescence guided resection (FGR) of brain tumours decreased residual tumour volume by a factor 16 compared to white light resection (12), while Stummer *et al* demonstrated that FGR decreased residual tumour in glioma patients and additionally influenced survival (13).

Extensive clinical (1, 2) and preclinical (5-7) studies with other PDT photosensitizers, including hematoporphyrin derivatives, show that PDT can kill brain tumours *in situ*, but at the cost of some damage to normal brain adjacent to tumour (6, 14). Using ALA-PpIX pre-clinically *in vitro* and *in vivo* we (6, 7) and others (5) suggest that tumour selective cytotoxicity is feasible. In particular tumour-cell apoptosis can be induced by low dose ALA-PDT without inducing a necrotic response in tumour or normal brain and with negligible apoptotic cell death in the latter (15). However, adequate and selective tumour kill likely cannot be achieved in a single treatment, so that it will be

necessary to apply the photosensitizer and light at low dose rates over an extended period, a regime that we have termed metronomic PDT (mPDT) (16, 17).

In summary, although both FGR and PDT have, individually, demonstrated potential benefit, it is likely that the combination will be more effective than either approach alone. It is the objective of the present work to develop and evaluate pre-clinical models and techniques required for this, for ultimate translation to clinical trials.

Hence, in this paper we demonstrate the technical feasibility of the combined treatment for the first time in a tumour-bearing animal model. This requires a relevant tumour model, a means of photosensitizer delivery and a light source/delivery system for low dose-rate photoactivation. This work is an extension of preliminary observations reported previously (18, 19).

Materials and Methods

Tumour induction and study groups

This study was approved by the Animal Care Committee of St. Michael's Hospital, Toronto. Rabbits with intracranially-induced VX2 carcinoma were used as the model. We recently demonstrated this is a reasonable first model for assessing FGR (12), since it provides tumours of reasonable size (5-8mm), which simplifies the technique compared to intracranial rat tumour models (18). The VX2 tumour has similarities in growth characteristics compared to human malignant gliomas, including microinvasion, pseudo palisading, growth along the blood vessels and in perivascular spaces and break down of the blood-brain barrier within the tumour and in brain adjacent to tumour (15). However, since the VX2 is not a glioma, it may not be the optimal model in terms of the biological responses to mPDT, as discussed in more detail below.

Table 1. Study groups, light delivery devices, light/ALA dose, administration time and mPDT frequency.

Group	n	FGR	mPDT Device	Light Dose (J)*	FGR/mPDT ALA dose (mg/kg)*	Illum./Admin. time (min/h)	mPDT Freq.
A	6	-	None	0	0/0	0	0
B	6	+	Dummy	0	0/0	0	0
C _{1,2}	2	+	Manual	15	20/100	42 / 5.5	Every other day
C _{3,4}	2	+	Sub-cut.	30	20/100	84 / 5	Daily
C _{5,6}	2	+	Backpack	30	20/100	84 / 5	Daily

*Light and ALA dose is given per treatment.

The techniques for tumour induction and FGR in this model have previously been described in detail (12). Briefly, tumours were induced in male New Zealand White rabbits (3.3-3.8kg, Charles River Canada, Montreal, QC). For this, 2.10^5 VX2 cells in 50µl phosphate buffered saline (PBS) were injected through a burr hole at a depth of 2 mm beneath the dura and allowed to grow. 18 of 22 animals survived without complications and were divided equally into 3 groups shown in table 1 as A, B and C. Group A did not undergo FGR nor mPDT. Group B underwent FGR followed by LED implant, but PDT was not applied. Group C underwent FGR followed by LED implant and received mPDT. All animals were

monitored twice daily and sacrificed by *i.v.* T61 injection (Intervet Canada, Whidby, ON) upon the first signs of neurological deficit, manifested as a pronounced head tilt that we estimate could not be missed more than once. Hence, the subjectivity in this observation was estimated to be 12 h.

Fluorescence-guided resection and surgical LED implant

FGR was performed as described previously (12). Briefly, 20mg/kg ALA (Levulan, DUSA Pharmaceuticals, Valhalla, NY, US) was diluted in PBS, buffered to pH 6.2-6.8 and injected *i.v.* within 15 min after preparation. Surgery was performed 7 days post VX2 induction and 4 h post ALA injection. Animals in groups B and C were anesthetized, a craniotomy was performed, the bone flap was removed, the dura was cut and subsequently the tumour was located with an operating microscope under white light illumination and resected by FGR. For this, the surgical cavity was illuminated with 405 nm (20 nm FWHM) light and red PpIX fluorescence was detected at 630 nm (20 nm FWHM, > OD 7 rejection of the blue/UV excitation light). The eyes were closed with tape during FGR, to prevent eye and skin photosensitive reactions. Biopsies were taken under FGR, fixed in formalin and saved for histopathology. Groups B and C received a permanent LED implant that was positioned inside the surgical cavity (L711SED/H, Kingbright, EMX Enterprises Ltd., Richmond Hill, ON, Canada). The LED was attached to the bone flap through an enlarged burr hole, as shown in Fig. 1a. To avoid irritation, the electric wires of the LED were isolated with medical grade silicone. To prevent light exposure to the skin, the rear side of the LED was covered with black medical grade epoxy. Electric wires were connected to a power supply in 3 different configurations, as described below. Hibitane antibiotic cream was applied topically on a daily basis to prevent irritation and infection. As described above, analgesic was administered. Steroids (Dexamethasone, Sabex, Boucherville, QC, Canada) were administered *i.m.* daily to all animals, starting 7 days after tumour induction, to decrease intracranial pressure and to mimic the clinical situation.

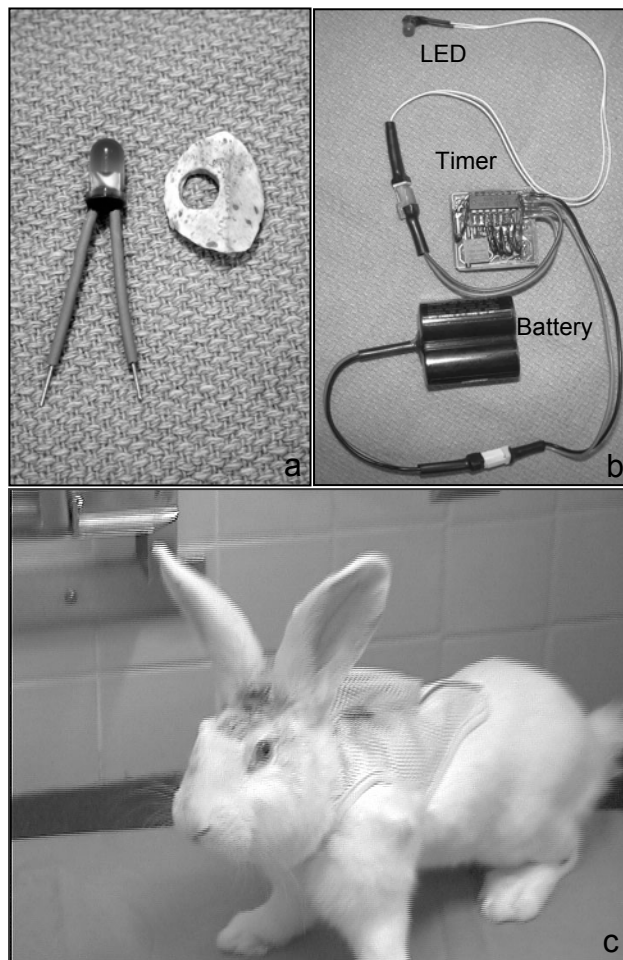


Fig. 1 (a) An LED placed into an enlarged burr hole in the bone flap. Electric wires were connected to a power supply in 3 different configurations. Manually, for this, the electric wires in (a) were connected to an external 6V DC power supply. (b) Subcutaneously, with an automatic timer switch and battery placed on the shoulders, or (c) held in a backpack.

Drug and light delivery for mPDT

For each mPDT treatment 100mg/kg ALA was prepared and injected as described above. mPDT was started the day following FGR. For this, the animals were not anaesthetized, but animals were kept under dim light levels for the entire period after tumour resection. The output power of the LED with 5mm diameter was 6 mW when supplying a 20mA driving current. We assumed the hemispherical diffuse LED surface to be in contact with brain tissue, which translated to an irradiance of approximately 6 mW.cm⁻². The center wavelength was 635nm (30nm FWHM), verified with a spectrometer. Because of the low power a relatively high ALA dose was used, significant bleaching of PpIX was not expected based on our previous FGR work where similar power levels were used for excitation of fluorescence and bleaching was not observed (12). The temperature of the LED did not exceed 37-39°C. For animals C_{1,2} the light was delivered every other day by manually connecting the LED wires exposed on the outside of the scalp to an external 6V DC power supply, delivering 15J over 42 min at 5.5h after ALA administration. With the intention to be less constraining, for animals C_{3,4} the light was delivered by a miniature automatic timer switch and 6V lithium battery (2CR5MPA/1B, 1400mAh, Panasonic) both embedded in medical grade silicone. This timer device was developed for this study and comprised a circuit board of three stages, 1.) a timer integrated circuit (IC) (LM556, Texas Instruments, TX, US) operating in mono stable mode and generating a square wave clock signal as input for the second stage, 2.) a 12 bit binary counter (CD4040, Texas Instruments, TX, US), the output of which was fed into 3.) a similar timer IC operating in monostable mode to provide the 20mA current for the LED. This device was able to switch on the LED daily for 84 min with the above battery.

In animals C_{3,4}, the timer and battery were placed subcutaneously on the shoulders with the electric wires of the LED passed subcutaneously from the skull, delivering 30J over 84 min once per day at 5h after daily ALA administration. The device shifted sideways causing discomfort, so that after two mPDT treatments the timer device and battery were surgically removed, but the LED remained in place. To avoid this problem in animals C_{5,6} a similar automatic timer switch and battery were held in a backpack (NP-620076, Harvard Apparatus, Saint-Laurent, QC, Canada) shown in Fig. 1c. These were well tolerated by the animals.

Histopathology

After sacrifice the brain was removed intact and fixed in 10% formalin for a minimum of 30 days. 5µm thick sections were prepared of the whole brain including the tumour regions and stained with hematoxylin and eosin (H&E). Gram stains were also performed to investigate the presence of any bacterial infection. Fluorimetric TUNEL (terminal deoxynucleotidyl transferase (TdT)-mediated dUTP nick-end labeling) staining was performed to investigate the presence of PDT-induced apoptotic cells. This stained the DNA of apoptotic cells with green fluorescein fluorescence (Promega, Madison, WI, US), while propidium iodine (Molecular probes, Eugene, OR, US) stained all cell nuclei with red fluorescence. These were examined simultaneously using a confocal laser-scanning microscope (LSM510, Zeiss, Germany) with 488nm excitation and 505-550nm detection for fluorescein and 543nm excitation and >585nm detection for propidium iodine.

Results

Surgical procedure and metronomic PDT

Tissue with positive PpIX fluorescence was detected and resected in animals in group B and C. Two rabbits did not recover from anesthesia, likely as a result of anesthetic overdose. One animal did not recover well from surgery, demonstrating unresponsive behavior and had to be sacrificed 4 days post resection. 1 animal scratched out the LED implant and was sacrificed, no other animal attempted to do so. The remaining 12 animals recovered well from tumour resection, showing normal responsive behavior, motor function, bowel output and food intake. *I.v.* ALA injections were performed within a ± 15 min window and the timer circuits worked successfully with an accuracy of ± 3 min.

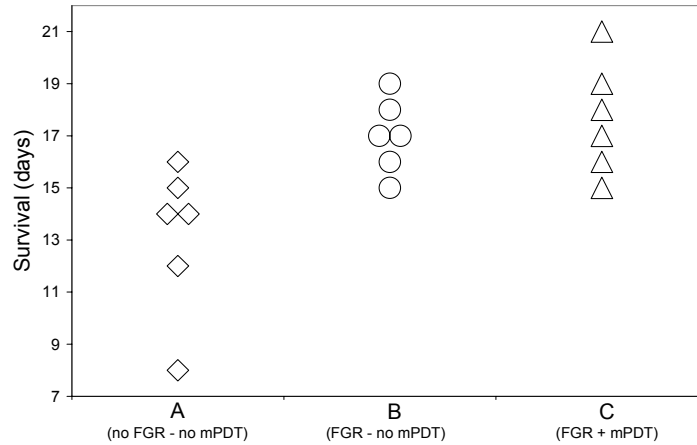


Figure. 2 Scatter plot with survival times for groups A, B and C. A significant difference ($p < 0.05$) was found between groups A and B, but not between B and C ($p > 0.05$).

Survival

All surviving animals were sacrificed between 8 and 21 days after tumour induction when demonstrating a head tilt. The average survival times were, group A: 13.3 ± 2.9 days, B: 17.0 ± 1.4 days and C: 17.7 ± 2.2 days, as shown in the scatter plot in Fig. 2. Rabbits C_{1,2}

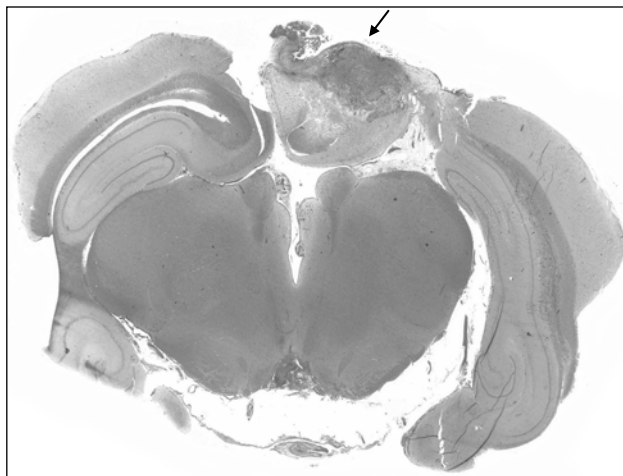


Fig. 3 H&E stained coronal section of the rabbit brain with the arrow pointing towards a recurrent VX2 tumour re-filling the resection cavity previously made by FGR.

were sacrificed at 15 and 16 days. Rabbits C_{3,4} were sacrificed at 17 and 19 days, where, as described above, the timer was removed as a result of discomfort after two mPDT treatments. Rabbits C_{5,6}, in which the backpack was used, were sacrificed at 18 and 21 days. An independent-sample t-test demonstrated a significant survival increase ($p < 0.05$) in group B compared to group A, indicating a benefit of tumour resection vs no resection. Group B and group C showed no significant difference ($p > 0.05$), indicating that daily mPDT of up to 30J and 100mg/kg ALA did not influence survival.

Histopathology

H&E stained sections of the biopsies taken during FGR revealed regions of infiltrative tumour under microscopy, similar to our previous findings (12). When removing the brain in groups A, B and C, the brains were swollen and tumour was visible with the naked eye. Coronal sections demonstrated large primary tumours in group A, and large recurrent tumours mostly refilling the surgical cavity made with FGR in groups B and C, as illustrated in Fig. 3. No necrosis was observed in proximity of the LED position. Gram stains were negative for all animals, demonstrating the sterility of the resection and LED implant surgical procedures. PDT-induced apoptosis is likely maximum in the 12-24h time interval after the last mPDT treatment (20), making it difficult to quantify apoptosis here, since most animals were sacrificed at different time points, according to neurological signs: C_{1,2} at 24-48h, C_{3,4} at > 48h, and C_{5,6} at 12 and 24h after the last mPDT treatment. TUNEL staining of group A (no mPDT) demonstrated only small percentages of apoptosis, in the range of 1-2% in the tumour, with no detectable apoptosis in the contra lateral normal brain. Similar results were found for animals C₁₋₄. By contrast, some sections of animals C_{5,6} demonstrated areas with a higher amounts of tumour-selective apoptosis, in particular the animal sacrificed at 12h post mPDT, as is shown in Fig. 4a. Note that the apoptosis is selectively present in the tumour and to a much lesser extent in the brain adjacent to tumour. The normal contra lateral brain shows no apoptosis as shown in Fig. 4b. H&E staining of adjacent sections demonstrated cell shrinkage and pyknosis, which are associated with apoptotic cells, at similar locations and rates of incidence (21).

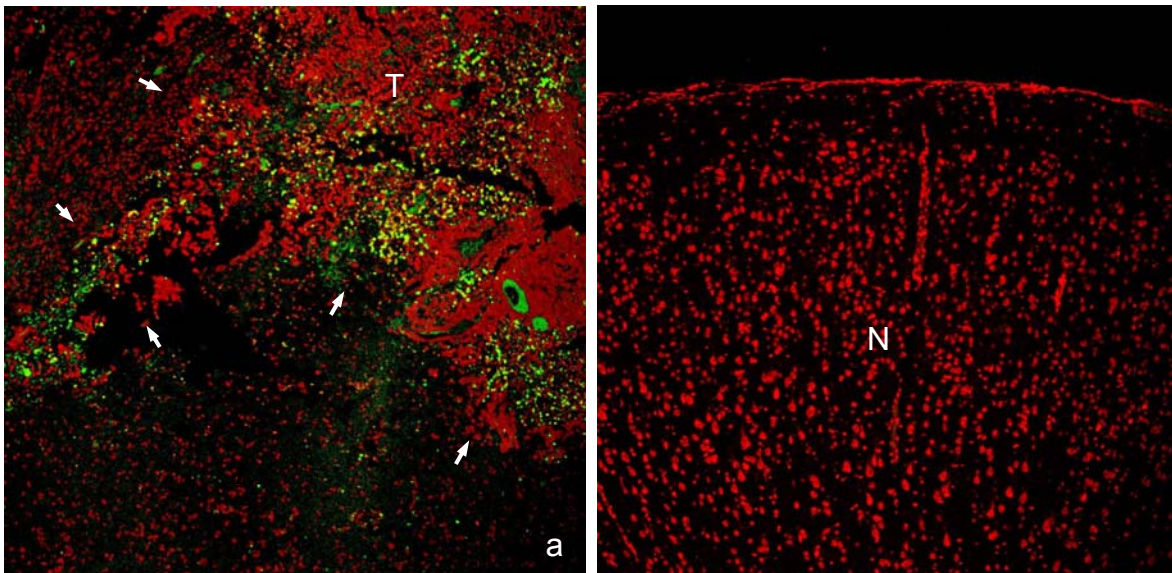


Fig. 4 Fluorescence confocal microscopy image (10x objective, NA 0.5) of fluorimetric TUNEL assay of rabbit brain sections. (a) The infiltrative tumour margin (T) and normal brain (N) 12h after 14 daily mPDT treatments. TUNEL positive (apoptotic) cells are stained green and all cells nuclei are labelled red (propidium iodine). The tumour margin can be identified, since the tumour has a larger nuclear density in comparison with the normal brain: arrows point towards the tumour margin (Permission for reproduction was obtained from the original publisher (17)). (b) Image of contra lateral normal brain.

Discussion

These results demonstrate that a new treatment strategy for malignant gliomas, comprising of fluorescence guided resection (FGR) with adjuvant metronomic PDT (mPDT) is technically feasible and the intracranial VX2 model in the rabbit is a candidate to evaluate this combined treatment.

Tissue morphology of group B demonstrated recurrent brain tumours approximately 10 days after FGR, refilling the entire surgical cavity. This is likely the result of small tumour nests that were undetected by FGR (12), but that can be detected using high sensitivity bioluminescence imaging with luciferase-transfected tumour cells (18). This is similar to gliomas, where recurrence is also often within close proximity of the resected margin (22, 23). This observation further validates the need to follow FGR by an adjuvant therapy such as mPDT.

The presence of apoptotic cell death with high tumour selectivity demonstrates that the concept of mPDT is valid in this model. However, FGR followed by mPDT with daily light and drug doses of up to 30J and 100mg/kg, for up to 14 days, did not influence survival compared to the FGR only group. This indicates further optimization of the mPDT treatment parameters (drug/light dose rates and application times) is required to improve survival, dose escalation studies are in progress.

Although the VX2 model has similarities in growth characteristics compared to gliomas, as discussed above, it is likely not the optimal tumour model in terms of the biological response to mPDT, since it is a carcinoma rather than a glioma. The murine 9L gliosarcoma, human U87 glioma or the rat CNS-1 glioma models are more relevant, so that we are extending this work to these rat models. Since the rat brain is smaller, this is substantially more challenging, both to achieve a high degree of tumour resection by FGR and to apply the mPDT light.

The methods used here to assess tumour response, namely the onset of neurological deficit and post mortem histopathology, provide information at only one time point and require sacrifice of the animal. It would be preferable to obtain tumour response data over multiple time points in single animals. This may be feasible with techniques as MR imaging, but this is costly and measures only gross tissue response. As mentioned above, an alternative is to use of bioluminescence imaging. We have recently demonstrated the feasibility of bioluminescence monitoring of (non-metronomic) PDT response *in vivo* (24). We plan, therefore, to use bioluminescence imaging to monitor completeness of FGR resection, tumour re-growth after resection and tumour response to mPDT (18).

Acknowledgements

This investigation was supported by grant CA 43892 DHHS/NIH/NCI and by the Canadian Institutes of Health Research. DUSA Pharmaceuticals NY kindly provided ALA. Microscopes and image processing software for histopathological analysis were provided by the Advanced Optical Microscope Facility (AOMF) at the Ontario Cancer Institute, Toronto, supported by the Canadian Foundation for Innovation.

References

1. Friesen, S. A., G. O. Hjortland, S. J. Madsen, H. Hirschberg, O. Engebraten, J. M. Nesland, and Q. Peng, 5-Aminolevulinic acid-based photodynamic detection and therapy of brain tumors (review), *Int. J. Oncol.*, 2002, 21, 577-582.
2. Kostron, H., A. Obwegeser, and R. Jakober, Photodynamic therapy in neurosurgery: a review, *J. Photochem. Photobiol. B: Biol.*, 1996, 36, 157-168.
3. Hebeda, K. M., A. E. Saarnak, M. Olivo, H. J. Sterenborg, and J. G. Wolbers, 5-Aminolevulinic acid induced endogenous porphyrin fluorescence in 9L and C6 brain tumours and in the normal rat brain, *Acta. Neurochir.*, 1998, 140, 503-512.
4. Olzowy, B., C. S. Hundt, S. Stocker, K. Bise, H. J. Reulen, and W. Stummer, Photoirradiation therapy of experimental malignant glioma with 5-aminolevulinic acid, *J. Neurosurg.*, 2002, 97, 970-976.
5. Stummer, W., S. R. Ennis, A. L. Betz, and R. F. Keep, In vitro and in vivo porphyrin accumulation by C6 glioma cells after exposure to 5-aminolevulinic acid, *Cereb. Blood Flow Metab.*, 1999, 19, 79-86.
6. Lilge, L., M. C. Olivo, S. W. Schatz, J. A. McGuire, M. S. Patterson, and B. C. Wilson, The sensitivity of normal brain and intracranially implanted VX2 tumour to interstitial photodynamic therapy, *Br. J. Cancer*, 1996, 73, 332-343.
7. Lilge, L., and B. C. Wilson, Photodynamic therapy of intracranial tissues: a preclinical comparative study of four different photosensitizers, *J. Clin. Laser Med. Surg.*, 1998, 16, 81-91.
8. Moan, J., L. W. Ma, A. Juzeniene, V. Iani, P. Juzenas, F. Apricena, and Q. Peng, Pharmacology of protoporphyrin IX in nude mice after application of ALA and ALA esters, *Int. J. Cancer*, 2003, 103, 132-135.
9. Ennis, S. R., A. Novotny, J. Xiang, P. Shakui, T. Masada, W. Stummer, D. E. Smith, and R. F. Keep, Transport of 5-aminolevulinic acid between blood and brain, *Brain Res.*, 2003, 959, 226-234.
10. Olivo, M., and B. C. Wilson, Mapping ALA-induced PPIX fluorescence in normal brain and brain tumour using confocal fluorescence microscopy, *Int. J. Oncol.*, 2004, 25, 37-45.
11. Niedre, M. J., A. J. Secord, M. S. Patterson, and B. C. Wilson, In vitro tests of the validity of singlet oxygen luminescence measurements as a dose metric in photodynamic therapy, *Cancer Res.*, 2003, 63, 7986-7994.
12. Bogaards, A., A. Varma, S. P. Collens, A. Lin, A. Giles, V. X. D. Yang, J. M. Bilbao, L. D. Lilge, P. J. Muller, and B. C. Wilson, Increased brain tumor resection using fluorescence guidance in a preclinical model, *Lasers Surg. Med.*, 2004, 35, 181-190.
13. Stummer, W., H. Stepp, G. Moller, A. Ehrhardt, M. Leonhard, and H. J. Reulen, Technical principles for protoporphyrin-IX-fluorescence guided microsurgical resection of malignant glioma tissue, *Acta Neurochir.*, 1998, 140, 995-1000.
14. Muller, P. J., and B. C. Wilson, Photodynamic therapy of malignant primary brain tumours: Clinical effects, post-operative ICP, and light penetration of the brain, *Photochem. Photobiol.*, 1987, 46, 929-935.
15. Lilge, L., M. Portnoy, and B. C. Wilson, Apoptosis induced in vivo by photodynamic therapy in normal brain and intracranial tumour tissue, *Br. J. Cancer*, 2000, 83, 1110-1117.
16. Wilson, B. C., S. K. Bisland, A. Bogaards, A. Lin, E. H. Moriyama, K. Zhang, and L. D. Lilge, Metronomic photodynamic therapy (mPDT): concepts and technical feasibility in brain tumor, *Proc. SPIE*, 2003, 4952, 23-31.
17. Bisland, S. K., L. Lilge, A. Lin, R. Rusnov, A. Bogaards, and B. C. Wilson, Metronomic Photodynamic Therapy as a New Paradigm for Photodynamic Therapy: Rationale and Preclinical Evaluation of Technical Feasibility for Treating Malignant Brain Tumors, *Photochem. Photobiol.*, 2004, 80, 22-30.
18. Bogaards, A., A. Varma, E. H. Moriyama, A. Lin, A. Giles, S. K. Bisland, L. D. Lilge, J. M. Bilbao, P. J. Muller, and B. C. Wilson, Fluorescence-guided resection of intracranial VX2

- tumor in a preclinical model using 5-aminolevulinic acid (ALA): preliminary results, *Proc. SPIE*, 2003, 4952, 91-96.
19. Bogaards, A., A. Varma, A. Lin, A. Giles, S. K. Bisland, L. Lilge, J. M. Bilbao, P. J. Muller, and B. C. Wilson, Preclinical feasibility of fluorescence-guided tumor resection followed by metronomic photodynamic therapy (mPDT) using 5-aminolevulinic acid induced protoporphyrin IX: Preliminary results, *SPIE Photonics North*, abstract, 2003,
 20. Lilge, L. D., K. Menzies, S. K. Bisland, A. Lin, and B. C. Wilson, PDT-induced apoptosis: investigations using two malignant brain tumor models, *Proc. SPIE*, 2002, 4612, 136-142.
 21. Darzynkiewics, Z., X. Li, and J. Gong, Discrimination of cells dying by apoptosis, *Meth. Cell Biol.*, 1194, 41, 15-38.
 22. Wallner, K. E., J. H. Galicich, G. Krol, E. Arbit, M. G. Malkin, and S. F. Wallner, Patterns of failure following treatment for glioblastoma multiforme and anaplastic astrocytoma Evidence that inhibition of erythropoiesis is important in the anemia of chronic renal failure, *Int. J. Rad. Oncol., Biol., Phys.*, 1989, 16, 1405-1409.
 23. Shapiro, W. R., L. S. Ashby, and E. A. Obbens, Current therapy for brain tumors: back to the future Brain tumors, *Arch. Neurol.*, 1999, 56, 429-432.
 24. Moriyama, E. H., S. K. Bisland, L. Lilge, and B. C. Wilson, Bioluminescence Imaging of the Response of Rat Gliosarcoma to ALA-PpIX Mediated Photodynamic Therapy, *Photochem. Photobiol.*, 2004, 80, 242-249.

Chapter 6

In vivo quantification of fluorescent molecular markers in real-time:

A modeling study to evaluate the performance of five existing methods

A Bogaards^{1,2}
HJCM Sterenborg²
BC Wilson¹

¹*University Health Network, Division of Biophysics and Bioimaging, Toronto, M5G2MG, Ontario, Canada*

²*Erasmus University Medical Center, Center for Optical Diagnostics and Therapy, Department of Radiotherapy, Rotterdam, POB 2040, 3000 CA Rotterdam, The Netherlands*

Manuscript submitted to J Biomed Opt. (2006)

Abstract

With the advent of molecular-targeted fluorescent markers there is a renewed interest in fluorescence quantification methods that are based on continuous wave excitation and multi-spectral image acquisition. However, little is known about their *in vivo* quantification performance. We evaluated the performance of five selected methods by, analytically describing these and varying the input parameters of, irradiance, excitation geometry, collection efficiency, autofluorescence, melanin content, blood volume, blood oxygenation and tissue scattering over relevant *in vivo* ranges, using optical properties resembling human skin. We identified one method that corrects for all of the above variations. This requires image acquisition before and after marker administration, under identical geometry. Hence, it is suited for applications where the site of interest can be relocated (e.g. anaesthetized animals and dermatology). For applications where relocation is not possible, we identified a second method where the uncertainty in the fluorescence signal was $\pm 20\%$. Hence, use of these methods can substantially aid *in vivo* fluorescence quantification over use of the raw fluorescence signal as this changed by more than 3 orders of magnitude. Since these methods can be computed in real-time, they are of particular interest for applications where direct feedback is critical, as diagnostic screening or image-guided surgery.

Introduction

“Early detection (of cancer) is and will continue to be, the single best way to significantly improve therapeutic outcomes.” (1). One approach that can enhance the capability of the physician to visualize early cancers is the administration of a tumor-selective fluorescent marker. The tissue can then be illuminated with light of an appropriate wavelength to excite the marker and the resulting fluorescence can be detected using a sensitive camera. This principle has been under investigation for the detection of various malignancies using either fluorescent markers or autofluorescence, for over 2 decades (2-4). In most applications the diagnostic accuracy obtained has been quite variable. This was mainly due to low fluorescence contrast between normal and tumor tissue, caused by non-specific uptake of more traditional fluorescent markers as fluorescein (5) and Photofrin™ (6). These relied on rather passive targeting strategies and generally depended on differences between the vasculature or pharmacokinetics of tumor *vs.* normal tissues.

More recent research is shifting the focus towards novel fluorescent markers that use active targeting strategies. Recent advances in nanotechnology and increasing knowledge of genes and proteins associated with cancers has enabled the engineering of nanoparticles that comprise a targeting moiety (e.g. antibodies, antibody fragments, peptides) conjugated to a fluorescent marker (1, 7-9). These particles hold promise to have an increased, more stable spectral intensity and improved tumor specificity compared with passively-targeting fluorescent markers.

In addition to providing information about the presence or absence of disease, as was typically the case for passively-targeted markers, actively-targeted markers can also yield functional information about physiological and molecular processes that relate to the invasiveness, progression and treatment response of the disease (9, 10). This complementary functional information directly available to the clinician *in vivo*, during diagnostic screening or surgery could improve clinical decision making may therefore ultimately improve therapeutic outcomes.

The ability to accurately quantify the *in vivo* measured marker fluorescence is critical to unravel functional disease information (1, 8). This is a major challenge since the fluorescence measured *in vivo* depends on many parameters other than the concentration of

the fluorescent marker, including the tissue autofluorescence, tissue-detector geometry and the absorbing and scattering properties of the tissue, which can contribute to quantification errors (11).

Several quantification techniques have been suggested employing either pulsed (12), modulated (13) or continuous wave (CW) excitation. Here we focus on the latter, as explained below.

Using CW excitation and tunable filters hyper spectral “data cubes” can be generated. With *a priori* knowledge of the fluorescent molecules that are present and using appropriate spectral unmixing algorithms the individual contribution of each can be determined (14, 15). Much progress has been made on the development of image reconstruction algorithms and instrumentation for fluorescence tomography using CW excitation(7). Fluorescent marker quantification by tomography has been validated in phantoms as well as *in vivo* in small animal models (16, 17).

However, the clinical utility of both hyper-spectral imaging and tomography is limited in applications where real-time feedback ($\sim \geq 30$ frames/sec) is required, as in endoscopic screening and image-guided surgery. Such high frame rates are currently difficult to achieve due to the complexity of image acquisition and processing (14, 18).

Tomographic 3-D information is not required *per se* for endoscopic applications nor, in most cases, for image-guided surgery, since early tumors arise, relatively superficially, in intra-epithelial layers at depths of a few hundred microns (19), while tumor surfaces are exposed during surgical resection. Hence, for these applications, 2-D quantification methods can be used. One approach is to employ multi spectral (rather than hyper-spectral) images, acquired in a few wavelength bands, combined with image processing algorithms that use combinations of subtractions and ratios. Due to their relative simplicity, real-time computation and display is feasible. Several of these approaches were first suggested in the literature around 20 years ago. With the advent of novel fluorescent molecular markers there is a renewed interest in these methods because of their apparent effectiveness and simplicity. For example, in 1984 Profio *et al.* calculated the ratio of marker signal over the reference autofluorescence signal (20). This approach was recently used by Nakayama *et al.* for quantification of blood perfusion in brown adipose tissues of mice, using the near-infrared marker indocyanine IR-786 (21), and was modified by Kircher *et al.* who instead of using the autofluorescence, used a second cyanine marker as reference, for quantification of enzyme activity (22, 23). Further, a subtraction method described in 1987 by Baumgartner *et al.* (24) is now commercially available on a widely used (25) small animal fluorescence imaging system (IVIS[®], Xenogen[®] Corp., Alameda, CA) to subtract the organ-specific autofluorescence (26). In addition to these several other methods have also been described (27-29).

Thus, although some of these methods are in active use today, little is known about their actual *in vivo* quantification performance. The objective of the present work was, to evaluate the performance of a selection of methods available in the literature through mathematical modeling. We described the fluorescence signals by closed-form, analytical solutions to the diffusion equation. The quantification performance was then evaluated by varying each of the input parameters of irradiance, excitation geometry, collection efficiency, autofluorescence, melanin content, blood content, blood oxygenation and tissue scattering over ranges that can be expected during *in vivo* imaging around a standard set of optical properties that resemble human skin.

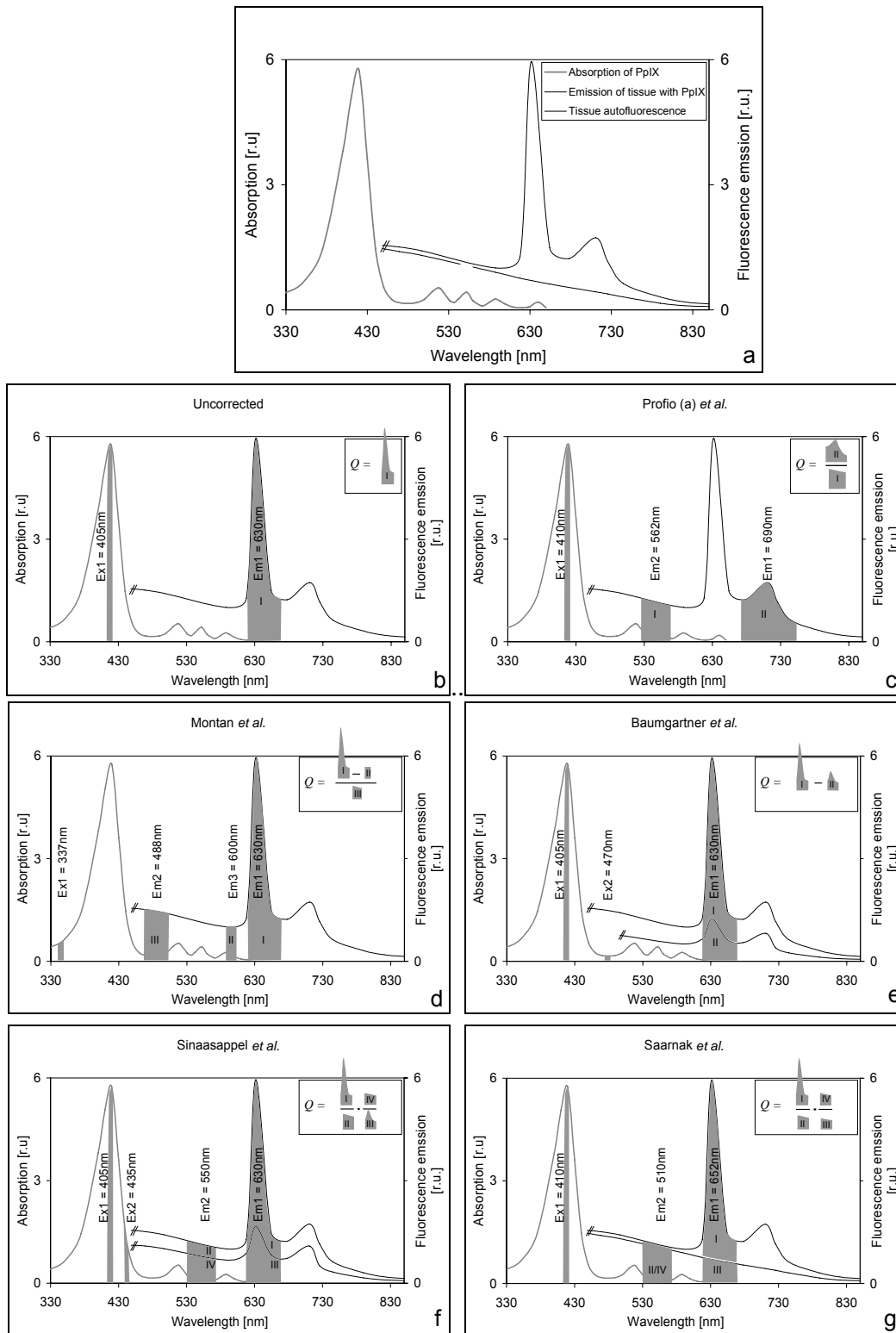


Figure 1. (a) Modeled excitation (grey) and emission (black) spectra of tissues containing the fluorescent marker protoporphyrin IX, which has an absorption peak at 410nm and characteristic emission peaks at 635 and 705nm. This is based on previous measurements in human subjects (38). The dashed line shows the tissue autofluorescence. Schematic representations of the uncorrected fluorescence signal and quantification methods are shown in (b-g).

Models and Methods

Correction Methods

Each method is depicted schematically in Fig.1. A porphyrin-like marker was selected as the model fluorophore, since the majority of these methods were developed for quantification of porphyrins. However, these methods can easily be adapted to other near-infrared markers by shifting the excitation and emission wavelengths. The signal output was referred to as Q_{method} and excitation and emission wavelengths are listed in Table 1.

Table 1. Excitation and emission wavelengths used in the different quantification methods

Correction Method	Excitation λ [nm]		Emission λ [nm]		
	<i>Ex1</i>	<i>Ex2</i>	<i>Em1</i>	<i>Em2</i>	<i>Em3</i>
Uncorrected	405		630		
Profio <i>et al.</i>	410		690	562	
Baumgartner <i>et al.</i>	405	470	630		
Montan <i>et al.</i>	337		630	488	600
Sinaasappel <i>et al.</i>	405	435	630	550	
Sarnak <i>et al.</i>	405		652	510	

The raw uncorrected fluorescence signal [$\text{mW}\cdot\text{cm}^{-2}$], as shown in Fig. 1b, employs a single excitation and emission wavelength and is described as,

$$Q_{Uncorrected} = F(\lambda_{ex1}, \lambda_{em1}) \quad 1$$

Profio *et al.* used a single excitation and two emission wavelengths, as shown in Fig. 1c. Here, the ratio was calculated of the red marker plus red autofluorescence over the autofluorescence in the green part of the spectrum where the fluorescence yield of the marker was negligible. The green autofluorescence was assumed constant and used as a reference (20), i.e.

$$Q_{Profio} = \frac{F(\lambda_{ex1}, \lambda_{em1})}{F(\lambda_{ex1}, \lambda_{em2})} \quad 2$$

This formalism is also valid for the work described by Nakayama *et al.* (21) and also that of Kircher *et al.* (23), where the autofluorescence in the denominator was replaced with fluorescence from a second marker, for which a second excitation wavelength was used.

Montan *et al.* (Fig.1d.) used one excitation and three emission wavelengths (27). The red background fluorescence was measured in a narrow spectral region in which there was minimal marker fluorescence. This was first subtracted from the red marker plus red autofluorescence and then divided by the autofluorescence in the blue-green spectral range,

$$Q_{Montan} = \frac{F(\lambda_{ex1}, \lambda_{em1}) - \kappa F(\lambda_{ex1}, \lambda_{em3})}{F(\lambda_{ex1}, \lambda_{em3})} \quad 4$$

After administration of the marker, the scaling factor κ was measured with a spectrograph in a normal tissue region with assumed negligible marker concentration ($C_m = 0$) and the magnitude of κ was chosen such that both red emission wavelengths yielded the same autofluorescence,

$$\kappa_{(C_m=0)} = \frac{F(\lambda_{ex1}, \lambda_{em1})}{F(\lambda_{ex1}, \lambda_{em3})} \quad 5$$

Baumgartner *et al.* used two excitation and one emission wavelengths (24). The first excitation wavelength was used to excite the marker plus autofluorescence and the second to excite mostly autofluorescence, so that this could be subtracted,

$$Q_{Baumgartner} = F(\lambda_{ex1}, \lambda_{em1}) - \beta F(\lambda_{ex2}, \lambda_{em1}) \quad 6$$

The excitation irradiances were scaled based on fluorescence imaging, before administration of the marker ($C_m = 0$), such that both excitation wavelengths yielded equal tissue autofluorescence,

$$\beta_{(C_m=0)} = \frac{F(\lambda_{ex1}, \lambda_{em1})}{F(\lambda_{ex2}, \lambda_{em1})} \quad 7$$

The above formalisms are also valid for the method that was recently described by Xenogen Corp. (26).

Sinaasappel *et al.* used two excitation and two emission wavelengths (28). Using excitation on and off an absorption peak of the marker, the red marker fluorescence was divided by the green autofluorescence (where the marker fluorescence is minimal). Subsequently, this red/green ratio was divided by a red/green ratio for the second excitation wavelength that was chosen to have low marker fluorescence,

$$Q_{Sinaasappel} = \frac{F(\lambda_{ex1}, \lambda_{em1})}{F(\lambda_{ex1}, \lambda_{em2})} \cdot \frac{F(\lambda_{ex2}, \lambda_{em2})}{F(\lambda_{ex2}, \lambda_{em1})} \quad 8$$

Saarnak *et al.* used one excitation and two emission wavelengths (29). The red marker fluorescence was divided by the green autofluorescence, similar to Profio *et al.* Subsequently, this was divided the same red/green ratio measured in tissue prior to marker administration ($C_m = 0$). Unlike the other methods evaluated here, this requires that the images are acquired, before and after marker administration on the same tissue site under identical geometry. The assumption was then made that the optical properties and autofluorescence may vary spatially, but remain constant over the time interval between image acquisitions,

$$Q_{Saarnak} = \frac{F(\lambda_{ex1}, \lambda_{em1})}{F(\lambda_{ex1}, \lambda_{em2})} \cdot \frac{F_{(C_i=0)}(\lambda_{ex1}, \lambda_{em2})}{F_{(C_i=0)}(\lambda_{ex1}, \lambda_{em1})} \quad 9$$

As these methods are based on continuous wave excitation they are inherently unable to extract information about changes in fluorescence quantum yield or lifetime.

Evaluation of quantification performance

We evaluated the correction performance of these different methods by mathematically describing the fluorescence signal, defining standard input parameters and introducing variations around these standard values. For this, one parameter was varied one at a time, with the other parameters fixed at their standard value. As a measure of the quantification or correction performance we defined the factor CP as the change in the corrected signal due to the introduced variations relative to the signal with the standard input parameters,

$CP = \frac{Q(\text{varied})}{Q(\text{standard})}$. For the purposes of inter-comparing the methods, we

calculated a Signal Change index, SC , as the maximum over the minimum correction

performance, $SC_{parameter} = \frac{|CP(\text{max})|}{|CP(\text{min})|}$. Here a value of 1.00 indicates perfect correction,

while larger values indicate imperfections. Additionally, the total signal change, TSC , was

defined as the product of the signal changes due to the individual parameters, at fixed target fluorophore concentration.

Mathematical description for fluorescence emission

The fluorescence generated at the tissue surface was described with analytical solutions to the diffusion equation. The formalism applied here was based on the time-independent, 1-D, broad-beam, homogeneous-medium case, which were correlated with Monte Carlo simulations for fluorescence generated at the tissue surface (30). This solution was modified by adding dimensionless functions γ and η that describe the influence of geometry on the excitation irradiance and the collection efficiency of the photodetector, respectively, and have values between 0 and 1. Further, we represented the fluorophores present in tissue as two groups and assumed that their absorption coefficients are proportional to the concentration. The first group is the fluorescent marker of interest, assumed to have known concentration, C_m [M], and fluorescence yield, H [$\text{cm}^{-1}\cdot\text{M}^{-1}$], at the excitation-emission wavelength pair $(\lambda_{ex}, \lambda_{em})$. H is the product of the fluorescence quantum yield and the molar extinction coefficient. The second group, tissue autofluorophores, have concentration C_a and fluorescence yield $A(\lambda_{ex}, \lambda_{em})$. Hence, the detected fluorescence signal, $F(\lambda_{ex}, \lambda_{em})$ in [$\text{mW}\cdot\text{cm}^{-2}$] is given by,

$$F(\lambda_{ex}, \lambda_{em}) = \left[\frac{I(\lambda_{ex}) \eta \gamma [C_m H(\lambda_{ex}, \lambda_{em}) + C_a A(\lambda_{ex}, \lambda_{em})]}{D(\lambda_{em}) [\mu'_t{}^2(\lambda_{ex}) - \mu_{ef}{}^2(\lambda_{em})]} \right] \cdot \left[\left(\frac{1 + 1.82 D(\lambda_{em}) \mu'_t(\lambda_{ex})}{1 + 1.82 D(\lambda_{em}) \mu_{ef}(\lambda_{em})} \right) - 1 \right] \quad 10$$

The excitation irradiance at excitation wavelength λ_{ex} [nm] is given by $I(\lambda_{ex})$ [$\text{mW}\cdot\text{m}^{-2}$]. $D(\lambda_{em})$ is the optical diffusion coefficient of the tissue at wavelength λ_{em} , given by $D(\lambda_{em}) = [3\mu'_t(\lambda_{em})]^{-1}$, where $\mu'_t(\lambda_{em})$ [cm^{-1}] is the linear attenuation coefficient given by $\mu'_t(\lambda_{em}) = \mu'_s(\lambda_{em}) + \mu_a^{total}(\lambda_{em})$. $\mu'_s(\lambda_{em})$ is the reduced scattering coefficient and $\mu_a^{total}(\lambda_{em})$ is the absorption coefficient of the tissue fluorophores (marker plus auto), so that $\mu_a^{total}(\lambda_{ex}) = \mu_a^{tissue}(\lambda_{ex}) + \mu_a^{fluorophores}(\lambda_{ex})$. The effective attenuation coefficient $\mu_{ef}(\lambda_{em})$ is given by, $\mu_{ef}(\lambda_{em}) = \sqrt{3\mu_a^{total}(\lambda_{em}) [\mu_a^{total}(\lambda_{em}) + \mu'_s(\lambda_{em})]}$. Further, the absorption of the tissue was considered much larger than that of the fluorophores ($\mu_a^{tissue} \gg \mu_a^{fluorophores}$), so that $\mu_a^{fluorophores}$ was chosen negligible in calculating $D(\lambda_{em})$, $\mu'_t(\lambda_{ex})$ and $\mu_{ef}(\lambda_{em})$.

Standard values for the input parameters

The following standard values were assigned, I : 100 mWcm^{-2} , γ and η : 1.00 [-]. C_m and C_a : 0.01 [M]. $H(\lambda_{ex}, \lambda_{em})$, and $A(\lambda_{ex}, \lambda_{em})$ are listed in Table 2. Their relative magnitude was estimated based on the fluorescence emission spectra shown in Fig. 1a.

The optical properties of human skin were calculated using the model of Svaasand *et al*, (31) providing average values for the epidermal and dermal layers. Parameters that dominate the absorption of human skin, μ_a^{skin} [cm^{-1}] in the visible to near-infrared wavelength range are blood volume (B), blood oxygenation (StO_2) and melanin content (M),

$$\mu_a^{skin}(\lambda, B, StO_2, M) = \mu_a^{blood}(\lambda, B, StO_2) + \mu_a^{melanin}(\lambda, M) + \mu_a^{unpigment} \quad 11$$

, where μ_a^{blood} is the absorption coefficient of blood,

$$\mu_a^{blood}(\lambda, B, StO_2) = B [StO_2 \cdot \mu_a^{HbO_2}(\lambda) + (1 - StO_2) \cdot \mu_a^{Hb}(\lambda)] \quad 12$$

B was assigned a standard value of 1% (31). $StO_2 = 100\%$ (32). The absorption coefficients for oxygenated, $\mu_a^{HbO_2}(\lambda)$, and de-oxygenated, $\mu_a^{Hb}(\lambda)$, hemoglobin were also obtained from literature values (33). The absorption coefficient of melanin $\mu_a^{melanin}$ was calculated by,

$$\mu_a^{melanin}(\lambda, M) = M \left[\frac{694}{\lambda} \right]^4 \quad 13$$

, with $M = 3 \text{ cm}^{-1}$, representative of Caucasian skin (31). The term μ_a^{unpig} , represents unpigmented tissue without blood or melanin and was assumed to be wavelength independent and equal to 0.3 cm^{-1} (31).

The reduced scattering coefficient of skin was calculated with (31),

$$\mu_s^{skin}(\lambda) = [29 \cdot 10^4 (\lambda^{-1}) + 1055 \cdot B] \cdot [1 - (0.62 + 29 \cdot 10^{-5} \cdot \lambda)] \quad 14$$

Fig. 2 shows the modeled values for the absorption spectra of deoxy- and oxygenated blood ($B=1\%$), the absorption of oxygenated Caucasian skin containing, and of the scattering coefficient of human skin.

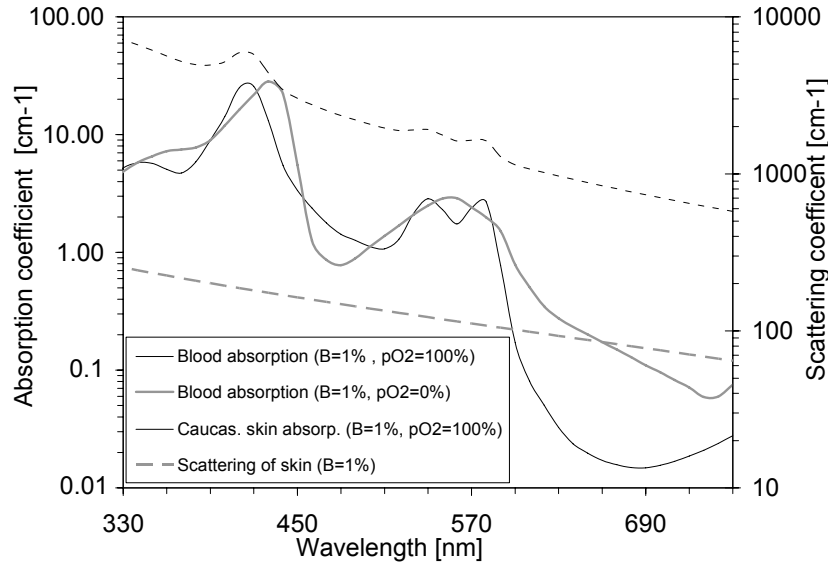


Fig. 2 Modeled absorption coefficient: for deoxygenated (grey line) and oxygenated (solid line) blood, Caucasian oxygenated skin (dashed), and the reduced scattering coefficient of skin (grey dashed). The blood volume $B = 1\%$.

Variations in the standard input parameters

The parameters were varied in the following ranges I : 30-100 mWcm^{-2} , γ and η : 0.3-1, C_a : 0.001-0.01 M. These were chosen rather arbitrarily, as literature values are not widely available. The fluorescence yields were assumed constant for each specific excitation-emission wavelength pair. The scaling factors a , β and κ were also fixed, as these were based on a single measurements on a control tissue site. B was varied in the 0.1-10% range, (31, 34) StO_2 was varied in the range of 10-100%, based on ref. (32) These ranges are representative of normal and tumor tissues. M was varied over 0.3-30 cm^{-1} , encompassing the vales reported for Caucasian, Asian and African skin (31). The reduced scattering coefficient was varied by a factor of 10 above the standard values, based on reported values for normal and tumor tissues (35).

Table 2. Modeled fluorescence yields used in the different quantification methods.
A: autofluorescence yield, H: marker fluorescence yield.

Correction Method	Excitation, emission wavelength pair [nm]	Fluorescence yield [a.u]
Uncorrected	H 405,630	16
	A 405,630	2
Profio <i>et al.</i>	A 410,562	4
	H 410, 690	8
Montan <i>et al.</i>	A 337, 488	6
	A 337, 600	1
	H 337, 630	2
Baumgartner <i>et al.</i>	H 407, 630	16
	H 470, 630	2
	A 407, 630	2
	A 470, 630	2
Sinaasappel <i>et al.</i>	A 405, 550	4
	H 405, 630	16
	H 435, 550	4
	H 435, 630	2
Saarnak <i>et al.</i>	H410, 652	16
	A410, 652	2
	A 410, 510	4

Results

Quantification performance and signal change due to individual parameters

The relative signal changes were plotted against variations in the input parameters, as shown in Fig. 3. The corresponding maximum signal changes are listed in Table 3. These results demonstrate that variations in I , η and γ could be entirely corrected ($SC = 1.00$) using the ratiometric methods of Profio *et al.* and Montan *et al.* However, these methods vary with the autofluorescence level and tissue optical properties. Conversely, variations in autofluorescence can be entirely corrected using the subtraction method of Baumgartner *et al.*, but this varies with I , η and γ and the tissue optical properties. The method of Sinaasappel *et al.* entirely corrects for variations in I , η , γ and also substantially corrects for variations in tissue optical properties and auto-fluorescence. The method described by Saarnak *et al.* corrects for all parameters evaluated here.

Total Signal Change

The total signal change, TSC , is listed in Table 3 for the different methods. In the ratiometric methods the largest contribution is due to a dependence on autofluorescence, followed by blood content. In the subtraction method of Baumgartner *et al.* the largest contributions are from variations in tissue scattering, followed in decreasing order by I , η , γ , melanin content and blood content.

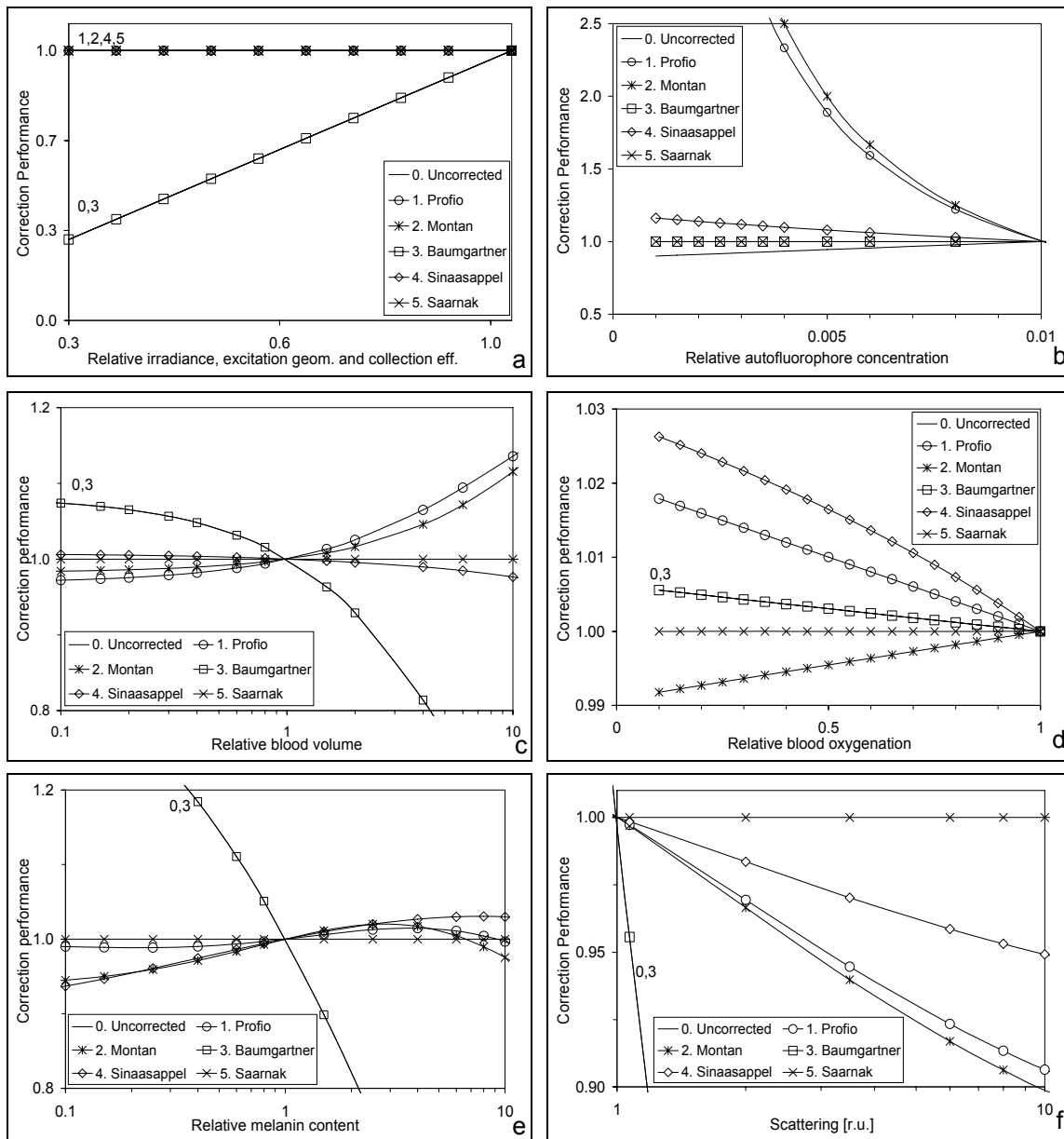


Fig. 3 Correction performance vs. (a) Irradiance, excitation geometry and collection efficiency, (b) autofluorescence, (c) blood volume, (d) blood oxygenation, (e) melanin content, and (f) tissue scattering.

Discussion

Model Calculations

We here demonstrated that use of analytical solutions and models provide an understanding of the major parameters that contribute to the *in vivo* fluorescence signal and is a relatively simple and efficient approach to evaluate the quantification performance objectively.

Due to the model assumptions, the results obtained here are valid if the fluorescent layer is exposed at the tissue surface and is optically thick relative to the penetration depth of

the excitation light. A guideline for this thickness may be found in studies of diffuse reflectance (here indicative of the excitation light), where the signal was found unchanged when the tissue was thicker than ~ 12 effective penetration depths (36). For UV excitation light, typical penetration depths of $\sim 0.1-0.3$ mm (35) have been reported for various biological tissues, in which case the fluorescent layer should be $\sim \geq 1-3$ mm thick. Hence, this model has relevance in a large number of clinical applications where the lesions are exposed to the tissue surface and are up to several mm in depth, such as early lesion detection in dermatology and endoscopy, as well as image-guided surgical resection.

A porphyrin was used as the model maker, however the results and conclusions obtained here will be generic to near-infrared fluorescent markers with respect to variations in irradiance, excitation-geometry, collection efficiency, and even autofluorescence, so long as the relative contribution to the raw uncorrected fluorescence signal falls within the ranges used here. With respect to blood and melanin absorption, tissue- oxygenation and scattering, the performance can further improve when carefully selecting the marker and their excitation and emission wavelengths towards the near-infrared wavelength range (37), where tissue absorption and scattering decrease, this is part of our ongoing research.

Table 3. *The Signal Changes and the Total Signal Change equal to product of the signal changes due to the individual parameters*

Correction Method	Total Signal Change	Signal Change due to variations in individual parameters					
		I, γ, η	C_a	B	StO_2	M	μ'_s
Uncorrected <i>et al</i>	1.72×10^3	3.33	1.11	1.82	1.01	3.50	6.51
Profio (a) <i>et al</i>	1.18×10^1	1.00	9.00	1.17	1.02	1.01	1.10
Baumgartner <i>et al</i>	1.55×10^3	3.33	1.00	1.82	1.01	3.50	6.51
Montan <i>et al</i>	1.31×10^1	1.00	10.0	1.14	1.01	1.03	1.11
Sinaasappel <i>et al</i>	1.42	1.00	1.16	1.03	1.03	1.10	1.05
Saarnak <i>et al</i>	1.00	1.00	1.00	1.00	1.00	1.00	1.00

Signal changes due to individual parameters

The results obtained here indicate that the subtraction method of Baumgartner *et al.* entirely corrected for variations in autofluorescence. The trade-off is a remaining dependence on variations in irradiance, excitation geometry, detection efficiency and tissue optical properties, since the subtraction does not cancel out any of these factors.

The methods of Profio *et al.*, Montan *et al.*, Sinaasappel *et al.* and Saarnak *et al.* make use of ratiometry and completely corrected for variations in irradiance, excitation geometry and detection efficiency, as these parameters cancel out in taking the ratio. This can be particularly useful in applications such as endoscopy, where these variations occur frequently and are not easily controlled. However, the trade-off for is a greater dependence on variations in the autofluorescence than even the uncorrected fluorescence signal itself, due to the large autofluorescence contribution in the denominator. The exception is the ratiometric method of Saarnak *et al.*, which has the same contribution of autofluorescence in both numerator and denominator. In these ratiometric methods the main reason for dependencies on tissue optical properties is the difference in optical properties between numerator and denominator. Correction for tissue optics is achieved in the method of Saarnak *et al.*, through use of an image set without marker in the denominator. In the

Sinaasappel method it is largely achieved by using an image set at a different fluorescence yield in the denominator.

Total quantification performance

The total signal change listed in table 3 demonstrates that use of any of the methods gave improvement over the uncorrected signal. At fixed marker concentration, the uncorrected signal can change by a large factor (1.72×10^3) as a result of the variations in excitation irradiance, excitation geometry, collection efficiency, auto-fluorescence, blood volume, blood oxygenation, melanin content and tissue scattering.

The method of Saarnak *et al.* demonstrated the best quantification performance, as it depends only on the concentration of the fluorescent maker. This method is based on image acquisition before and after marker administration and it requires these subsequent images to be taken on the same tissue site under identical geometry. Hence, the assumption is made that the optical properties and autofluorescence may change spatially within the image, but remain constant over the time interval between image acquisitions. This could be useful in any Application where these conditions could be met include lesion detection in dermatology and pre-clinical research where, before and after administration of the marker, the tissue of interest can be re-located and the geometry can be controlled, as is the case for the device reported by Xenogen Corp. (26).

For many clinical applications, however, these conditions can not easily be met, e.g. in endoscopic screening, image-guided surgical resection or monitoring treatment response, as it may not be feasible to control the geometry and/or re-locate the tissue area of interest. The assumption that autofluorescence and tissue optical properties remain constant over the administration time of the marker may also not be valid since these can vary with treatment or surgery. In these cases the method of Sinaasappel *et al.*, which does have such restrictive conditions could be used. This method demonstrated the best correction in cases where the geometry is not well controlled, correcting fully for variations in irradiance, excitation geometry and collection efficiency. Due to relatively small dependence on mainly autofluorescence the Total Signal Change was 1.42, which can be interpreted as an uncertainty of $\sim \pm 20\%$. This should be acceptable in many applications. In the other methods the Total Signal Change was more than a factor of 10, which makes them unsuitable for any application where absolute or even relative quantification of the fluorescence signal is important.

Kircher *et al.* recently adapted the method of Profio *et al.* by replacing the autofluorescence with the fluorescence of a second marker (22, 23). The variations in concentration of this second marker are not well established currently. However, if these are $< \pm 5\%$, the TSC of this method would also be in the ~ 1.4 range, making it a suitable quantification method.

Hence, use of these methods can substantially aid *in vivo* fluorescence quantification over use of the raw fluorescence signal. As these can be computed and displayed in real-time they are of particular interest for applications where direct feedback is critical as endoscopic screening and image-guided surgery.

The use of existing-, and the development of novel quantification methods based on continuous wave excitation and multi spectral image acquisition should therefore be further explored as these offer simple and efficient means for *in vivo* fluorescence quantification in real-time.

Acknowledgements

This work was funded by NIH grant CA-43892. A. Bogaards was also supported in part by the Muzzo Fund of the Princess Margaret Hospital Foundation and the Dutch Technology Foundation, grant number AGN 3413 and the European Commission, Contract number BMH4-CT97-2260.

References

1. Sullivan DC and Ferrari M (2004). Nanotechnology and tumor imaging: seizing an opportunity. *Mol Imaging*. **3**:364-9.
2. Wagnieres G (2003). Lung cancer imaging with fluorescence endoscopy. In *Handbook of biomedical fluorescence*. M. Mycek and B.W. Pogue, Eds. Marcel Dekker Inc., New York. pp. 361-396.
3. DaCosta RS, Wilson BC, and Marcon NE (2000). Light-induced fluorescence endoscopy of the gastrointestinal tract. *Gastrointestinal Endoscopy*. **10**:1-33.
4. de Veld DC, Witjes MJ, Sterenborg HJ, and Roodenburg JL (2005). The status of in vivo autofluorescence spectroscopy and imaging for oral oncology. *Oral Oncol*. **41**:117-31.
5. Aalders MC, Sterenborg HJCM, and van der Vange N (2004). Fluorescein angiography for the detection of metastases of ovarian tumor in the abdominal cavity, a feasibility pilot. *Lasers Surg Med*. **35**:349-53.
6. Stummer W, Gotz C, Hassan A, Heimann A, and Kempfski O (1993). Kinetics of Photofrin II in perifocal brain edema. *Neurosurg*. **33**:1075-81; discussion 1081-2.
7. Ntziachristos V, Ripoll J, Wang LV, and Weissleder R (2005). Looking and listening to light: the evolution of whole-body photonic imaging. *Nat Biotechnol*. **23**:313-20.
8. Cherry SR (2004). In vivo molecular and genomic imaging: new challenges for imaging physics. *Phys Med Biol*. **49**:R13-48.
9. Choy G, Choyke P, and Libutti SK (2003). Current advances in molecular imaging: noninvasive in vivo bioluminescent and fluorescent optical imaging in cancer research. *Mol Imaging*. **2**:303-12.
10. Sokolov K, Aaron J, Hsu B, Nida D, Gillenwater A, Follen M, MacAulay C, Adler-Storthz K, Korgel B, Descour M, Pasqualini R, Arap W, Lam W, and Richards-Kortum R (2003). Optical systems for in vivo molecular imaging of cancer. *Technol Cancer Res Treat*. **2**:491-504.
11. Bogaards A, Aalders MC, Zeyl CC, de Blok S, Dannecker C, Hillemanns P, Stepp H, and Sterenborg HJ (2002). Localization and staging of cervical intraepithelial neoplasia using double ratio fluorescence imaging. *J Biomed Opt*. **7**:215-20.
12. Kumar AT, Skoch J, Bacskai BJ, Boas DA, and Dunn AK (2005). Fluorescence-lifetime-based tomography for turbid media. *Opt Lett*. **30**:3347-9.
13. Roy R, Godavarty A, and Sevick-Muraca EM (2003). Fluorescence-enhanced optical tomography using referenced measurements of heterogeneous media. *IEEE Trans Med Imaging*. **22**:824-36.
14. Mansfield JR, Gossage KW, Hoyt CC, and Levenson RM (2005). Autofluorescence removal, multiplexing, and automated analysis methods for in-vivo fluorescence imaging. *J Biomed Opt*. **10**:41207.
15. Gao X, Cui Y, Levenson RM, Chung LW, and Nie S (2004). In vivo cancer targeting and imaging with semiconductor quantum dots. *Nat Biotechnol*. **22**:969-76.
16. Graves EE, Yessayan D, Turner G, Weissleder R, and Ntziachristos V (2005). Validation of in vivo fluorochrome concentrations measured using fluorescence molecular tomography. *J Biomed Opt*. **10**:44019.

17. Ntziachristos V, Schellenberger EA, Ripoll J, Yessayan D, Graves E, Bogdanov A, Jr., Josephson L, and Weissleder R (2004). Visualization of antitumor treatment by means of fluorescence molecular tomography with an annexin V-Cy5.5 conjugate. *Proc Natl Acad Sci U S A*. **101**:12294-9.
18. Graves EE, Ripoll J, Weissleder R, and Ntziachristos V (2003). A submillimeter resolution fluorescence molecular imaging system for small animal imaging. *Med Phys*. **30**:901-11.
19. Flejou JF (2005). Barrett's oesophagus: from metaplasia to dysplasia and cancer. *Gut*. **54 Suppl 1**:i6-12.
20. Profio A (1984). Laser excited fluorescence of hematoporphyrinderivative for diagnosis of cancer. *IEEE Quant Electron*. **QE20**:1502-1507.
21. Nakayama A, Bianco AC, Zhang CY, Lowell BB, and Frangioni JV (2003). Quantitation of brown adipose tissue perfusion in transgenic mice using near-infrared fluorescence imaging. *Mol Imaging*. **2**:37-49.
22. Kircher MF, Weissleder R, and Josephson L (2004). A dual fluorochrome probe for imaging proteases. *Bioconjug Chem*. **15**:242-8.
23. Kircher MF, Josephson L, and Weissleder R (2002). Ratio imaging of enzyme activity using dual wavelength optical reporters. *Mol Imaging*. **1**:89-95.
24. Baumgartner R, Fisslinger H, Jocham D, Lenz H, Ruprecht L, Stepp H, and Unsold E (1987). A fluorescence imaging device for endoscopic detection of early stage cancer--instrumental and experimental studies. *Photochem Photobiol*. **46**:759-63.
25. Xenogen Corp. , <http://www.xenogen.com/wt/page/publications>.
26. Troy T, Jekic-McMullen D, Sambucetti L, and Rice B (2004). Quantitative comparison of the sensitivity of detection of fluorescent and bioluminescent reporters in animal models. *Mol Imaging*. **3**:9-23.
27. Montan S, Svanberg K, and Svanberg S (1985). Multicolor imaging an contrast enhancement in cancer-tumor localization using laser-induced fluorescence in hematoporphyrin-derivative-bearing tissue. *Optics Letters*. **10**:56-58.
28. Sinaasappel M and Sterenborg HJCM (1993). Quantification of the hematoporphyrin derivative by fluorescence measurement using dual-wavelength excitation and dual-wavelength detection. *Appl Opt*. **32**:541-548.
29. Saarnak AE, Rodrigues T, Schwartz J, Moore AL, van Gemert MJC, Thompson S, and Sterenborg HJCM (1998). Influence of tumour depth, blood absorption and autofluorescence on measurement of exogenous fluorophores in tissue. *Lasers in Med Sci*. **13**:22-31.
30. Farrell TJ and Patterson MS (2003). Diffusion modeling of fluorescence in tissue. In *Handbook of biomedical fluorescence*. M. Mycek and B.W. Pogue, Eds. Marcel Dekker, Inc., New York. pp. 29-60.
31. Svaasand LO, Norvang LT, Fiskerstrand EJ, Stopps EKS, Berrns MW, and Nelson JS (1995). Tissue parameters determining the visual appearance of normal skin and port-wine stain. *Lasers in Med Sci*. **10**:55-65.
32. Amelink A, Sterenborg HJ, Bard MP, and Burgers SA (2004). In vivo measurement of the local optical properties of tissue by use of differential path-length spectroscopy. *Opt Lett*. **29**:1087-9.
33. Prahl S <http://omlc.ogi.edu/spectra/hemoglobin/index.html>.
34. van Veen RL, Sterenborg HJ, Marinelli AW, and Menke-Pluymers M (2004). Intraoperatively assessed optical properties of malignant and healthy breast tissue used to determine the optimum wavelength of contrast for optical mammography. *J Biomed Opt*. **9**:1129-36.
35. Cheong W-F (1995). Appendix to chapter 8: Summary of optical properties. In *Optical-Thermal Response of Laser-Irradiated Tissue*. A.J. Welch and M.J.C. van Gemert, Eds. Plenum Press, New York. pp. 275-303.
36. Wilson BC and Jacques SL (1990). Optical reflectance and transmittance of tissues: principles and applications. *IEEE J Quant Electron*. **26**:2186-2198.

37. Lim YT, Kim S, Nakayama A, Stott NE, Bawendi MG, and Frangioni JV (2003). Selection of quantum dot wavelengths for biomedical assays and imaging. *Mol Imaging*. **2**:50-64.
38. Wilson BC, Weersink RA, and Lilge L (2003). Fluorescence in Photodynamic Therapy Dosimetry. In *Handbook of biomedical fluorescence*. M. Mycek and B.W. Pogue, Eds. Marcel Dekker, Inc., New York. pp. 529-561.

Chapter 7

In vivo quantification of fluorescent molecular markers in real-time by ratio imaging for diagnostic screening and image-guided surgery

A Bogaards^{1,2}
HJCM Sterenberg²
J Trachtenberg³
BC Wilson¹
L Lilge¹

University Health Network, Division of Biophysics and Bioimaging¹, The Prostate Centre³ Toronto, M5G2MG, Ontario, Canada

²Erasmus University Medical Center, Center for Optical Diagnostics and Therapy, Department of Radiotherapy, Rotterdam, POB 2040, 3000 CA Rotterdam, The Netherlands

Manuscript in progress

Abstract

Future applications of 'molecular diagnostic screening' and 'molecular image-guided surgery' will demand images of molecular markers with high resolution and high throughput ($\sim \geq 30$ frames/sec). MRI, SPECT, PET, optical fluorescence tomography, hyper-spectral fluorescence imaging and bioluminescence imaging do not offer such high frame rates. 2D optical fluorescence imaging can provide surface images with high resolution and high throughput. The ability to accurately quantify the fluorescence *in vivo* is critical to extract functional information of the disease state, however few methods are available.

Here, a ratiometric 2D quantification method is introduced. Through mathematical modeling the performance was evaluated using optical properties that resembled biological tissues with the fluorescent marker Protoporphyrin IX. Experimentally the performance was evaluated in optical phantoms with different optical properties employing a prototype imaging system. The clinical feasibility of real-time, image-guided surgery was demonstrated in patients undergoing prostatectomy.

Discussed are the reasons why the introduced method leads to an increased quantification performance followed by modifications so it can be applied to novel fluorescent molecular markers as phthalocyanine 4 and dual-fluorescent markers. These offer additional advantages as these can provide a linear response to marker concentration and further minimize the dependence on autofluorescence and optical properties, as demonstrated through modeling.

Introduction

Recent advances in genomics, proteomics and nanotechnology have enabled the engineering of nanoparticles that comprise a targeting moiety (such as antibodies, antibody fragments or peptides) conjugated to a marker ligand (1). This marker can have ferromagnetic, radioactive, echogenic, fluorescent or bioluminescent properties such that it can be visualized with the appropriate imaging device (magnetic resonance imaging (MRI), single-photon computed tomography (SPECT), positron emission tomography (PET), ultrasound or optical imaging, respectively) (2).

Not only can imaging of these particles be used for early detection of cancer, excitingly, it can also yield functional information on a molecular level, about the invasiveness, progression and treatment response of the disease (3, 4). This information, directly available to the clinician during 'molecular diagnostic screening' or 'molecular image-guided surgery', has the potential to improve clinical decision making and hence could ultimately improve diagnostic accuracy and outcome. To illustrate this, in breast cancer over expression of the human epidermal growth factor receptor 2 (HER-2) was shown to be associated with (a) the presence of disease, (b) involvement of auxiliary lymph nodes (c) grade 3 tumors (d) resistance or benefit of specific adjuvant treatments and (e) poor prognosis (5). Hence, if it were possible to visualize and quantify HER-2 *during* surgical resection, this information may then be used (a) to enable more complete surgical resection, (b) as a decision criterion for lymph node resection, as direct assessment of (c) tumor grade and (d) for the rational selection of adjuvant treatments, to improve overall prognosis (e).

Both applications of diagnostic screening and image-guided surgery demand high throughput, high resolution images of, in most cases, the tissue surface, with real-time display of $\sim \geq 30$ frames/sec. MRI, SPECT, PET, optical fluorescence tomography, hyper-spectral fluorescence imaging and bioluminescence imaging do currently not offer such high frame rates due to the complexity of tomographic image acquisition and reconstruction (6), acquisition and unmixing of hyper-spectral data cubes (7, 8), or low bioluminescence photon budget (9). By contrast, 2D ultrasound and 2D optical fluorescence imaging do offer high

throughput imaging, whereas ultrasound typically offers B-scan images representing a section through the tissue and optical fluorescence imaging offers tissue surface images, at high resolution with relatively low technological complexity and significantly lower cost (3).

Hence, the currently available imaging modality that could meet the demands of ‘molecular diagnostic screening’ and ‘molecular image-guided surgery’ is optical fluorescence imaging, since this can provide surface images at high throughput and high resolution and low cost.

However, the ability to accurately quantify the *in vivo* fluorescence is critical to extract functional information of the disease state. (2). This, is a major challenge, because the *in vivo* fluorescence depends on many parameters other than the concentration of the fluorescent marker. Examples are variations in the tissue-to-detector geometry, autofluorescence and tissue optical properties, so that the raw fluorescence image can be subject to several artifacts that compromise accurate quantification (7, 9, 10, 11).

Several 2D fluorescence image quantification methods have been suggested in the literature that are based on multi-spectral image acquisition and subsequent image processing that employ subtractions and ratios. These are able to quantify fluorescence generated at the tissue surface. This is useful in endoscopic applications and, in most cases, for image-guided surgery, since various early tumors arise relatively superficially, in intra-epithelial layers at depths of a few hundred microns (12), while tumor surfaces are exposed during surgical resection. We recently evaluated the quantification performance of these methods and demonstrated that it is possible to correct 2D images for large variations in geometry, autofluorescence and unknown tissue optical properties. A method was identified that is well suited for applications as endoscopic screening or image-guided surgery. The variation in the output signal of this method was $< \pm 20\%$ as compared to orders of magnitude for the raw fluorescence, so that it can substantially aid in quantification (13).

There are certain disadvantages to this method. The majority of this variation is caused by a remaining dependence on variations in autofluorescence. Therefore, the detection systems requires a high sensitivity and dynamic range as it requires measurement of marker fluorescence and of only autofluorescence, which typically differ by an order of magnitude in signal strength. Further, it has a non-linear response to the marker concentration and reaches a plateau at higher concentrations.

Therefore, it would be advantageous to develop novel quantification methods that are not dependent on variations in autofluorescence, do not require separate measurements of autofluorescence, and have a linear response to the concentration of the fluorescent marker over a wide range of concentrations. Such methods should also be applicable to different fluorescent markers. For experimental and clinical verification of these methods, prototype fluorescence imaging systems will need to be developed that can process and display the images in real-time, as these are currently non-existent.

To address this need, here, a ratiometric quantification method is introduced. The performance was evaluated employing the mathematical model described previously (13). Optical properties used resembled biological tissues with the fluorescent marker Protoporphyrin IX (PpIX). We choose this marker as it is used clinically (14, 15) and will therefore likely form the baseline minimal signal strength that may be anticipated with novel molecular fluorescent markers. For experimental evaluation a prototype clinical fluorescence imaging system was developed that can process and display the images in real-time. Using this device the performance was evaluated in optical phantoms with different optical properties. The clinical feasibility of real-time, image-guided surgery was demonstrated in patients undergoing radical prostatectomy.

The reasons why this method leads to an increased quantification performance are discussed. Further, modifications of this method are presented so it can be used for NIR excitation and detection of phthalocyanine 4 (16), and, applied to novel dual-fluorescent markers (17, 18). These offer additional advantages as they can be conjugated to various targeting moieties, provide a linear response to marker concentration and further minimize the dependence on autofluorescence, as demonstrated through modeling.

Materials and Methods

Model Calculations

In a similar fashion as described before (13), the correction performance was evaluated by describing the method analytically using mathematical descriptions for fluorescence emission from turbid media, defining standard input parameters and introducing variations around these standard values. For this, one parameter was varied at a time, with the other parameters fixed at their standard value. As a measure of the quantification or correction performance the factor, CP , was defined as the change in the corrected signal due to the introduced variations relative to the signal with the standard input parameters. The Signal Change index, $SC_{parameter}$, was calculated as the maximum divided by the minimum correction performance and the total signal change, SC_{total} , was defined as the product of the signal changes due to the individual parameters, at fixed target fluorophore concentration. An SC_{total} of 1.50 can be interpreted as variation in output signal of $\leq \pm 25\%$. MATLAB® (The MathWorks Inc., US) was used for modeling and the code is available upon request.

The fluorescence and diffuse reflectance were described as $F(\lambda_{ex}, \lambda_{em})$ and $R(\lambda_{ex})$ [$\text{mW}\cdot\text{cm}^{-2}$], where λ_{ex} and λ_{em} stand for the excitation and emission wavelengths [nm], respectively as summarized in Table 1.

Table 1. Chosen excitation and emission wavelengths for methods and marker

Method	Marker	λ_{ex1}	λ_{ex2}	λ_{em1}
Q_{Raw}	PpIX	406		630
Q_1	PpIX	406	436	630
Q_2	PC4	686	650	710
Q_3	Dual1	620		700
Q_3	Dual2	730		800
Q_4	Dual1	620	640	700
Q_4	Dual2	730	750	800

The raw fluorescence signal, Q_{Raw} , uses a single excitation wavelength in the ultra violet (UV) to blue range and a single emission wavelength in the far red to near-infrared (NIR) range and is described as,

$$Q_{Raw} = F(\lambda_{ex1}, \lambda_{em1}) \quad 1$$

The ratiometric method introduced here, Q_i , employs two excitation and two emission wavelengths. Using the first excitation wavelength at an absorption maximum of the fluorescent marker, the red marker fluorescence was divided by diffusely reflected excitation light. Subsequently, this fluorescence/reflectance ratio is divided by a

fluorescence/reflectance ratio excited at the second excitation wavelength at an absorption minimum of the marker,

$$Q_1 = \frac{F(\lambda_{ex1}, \lambda_{em1})}{R(\lambda_{ex1})} \cdot \frac{R(\lambda_{ex2})}{F(\lambda_{ex2}, \lambda_{em1})} \quad 2$$

Protoporphyrin IX (PpIX) was used as the model fluorescent marker and the excitation and emission spectra are shown schematically in Fig. 2. Both the PpIX fluorescence and the tissue autofluorescence, were based on previous measurements in human subjects (19).

The fluorescence and diffuse reflectance emitted at the tissue surface was described by analytical solutions to the diffusion equation. These solutions were similar to those used in our previous study (13), differing only in that the formalisms used here are valid for excitation in the entire UV-NIR wavelength range. These formalisms have been validated and have demonstrated similar accuracy as compared to Monte Carlo modeling (20),

$$\begin{aligned} R(\lambda_{ex}) &= \eta\gamma[V + W] \\ F(\lambda_{ex}, \lambda_{em}) &= \eta\gamma[X + Y + Z] \end{aligned} \quad 3$$

where,

$$\begin{aligned} V &= -W \frac{1 + 1.82D(\lambda_{ex})\mu_{eff}(\lambda_{ex})}{1 + 1.82D(\lambda_{ex})\mu_{eff}(\lambda_{ex})}, \quad W = -\frac{\mu_s'(\lambda_{ex})I(\lambda_{ex})}{D(\lambda_{ex})} \cdot \frac{1}{\mu_t'^2(\lambda_{ex}) - \mu_{eff}^2(\lambda_{ex})} \\ X &= -Y \frac{1 + 1.82D(\lambda_{em})\mu_{eff}(\lambda_{ex})}{1 + 1.82D(\lambda_{em})\mu_{eff}(\lambda_{em})} - Z \frac{1 + 1.82D(\lambda_{em})\mu_t'(\lambda_{ex})}{1 + 1.82D(\lambda_{em})\mu_{eff}(\lambda_{em})} \end{aligned} \quad 4$$

$$Y = -\frac{-V[C_m M(\lambda_{ex}, \lambda_{em}) + C_a A(\lambda_{ex}, \lambda_{em})]}{D(\lambda_{em})[\mu_{eff}^2(\lambda_{ex}) - \mu_{eff}^2(\lambda_{em})]}, \quad Z = \frac{[W + I(\lambda_{ex})][C_m M(\lambda_{ex}, \lambda_{em}) + C_a A(\lambda_{ex}, \lambda_{em})]}{D(\lambda_{em})[\mu_t'^2(\lambda_{ex}) - \mu_{eff}^2(\lambda_{em})]}$$

The dimensionless functions, γ and η include the influence of geometry on the excitation irradiance and the collection efficiency of the photo detector, respectively. C_m and C_a stand for the fluorescent marker and auto fluorophores concentrations [M], with fluorescence yields, $M(\lambda_{ex}, \lambda_{em})$ and $A(\lambda_{ex}, \lambda_{em})$ [$\text{cm}^{-1} \cdot \text{M}^{-1}$], respectively. The excitation irradiance is given by $I(\lambda_{ex})$ [$\text{mW} \cdot \text{m}^{-2}$]. $D(\lambda)$ is the optical diffusion coefficient, $D(\lambda) = [3\mu_t'(\lambda)]^{-1}$, where $\mu_t'(\lambda)$ [cm^{-1}] is given by $\mu_t'(\lambda) = \mu_s'(\lambda) + \mu_a^{total}(\lambda)$, $\mu_s'(\lambda)$ is the reduced scattering coefficient and $\mu_a^{total}(\lambda)$ is the absorption coefficient of the tissue fluorophores (target plus auto), so that $\mu_a^{total}(\lambda) = \mu_a^{tissue}(\lambda) + \mu_a^{fluorophores}(\lambda)$. The effective attenuation coefficient $\mu_{eff}(\lambda)$ is given by, $\mu_{eff}(\lambda) = \sqrt{3\mu_a^{total}(\lambda)[\mu_a^{total}(\lambda) + \mu_s'(\lambda)]}$. The absorption of the tissue was considered much larger than that of the fluorescent marker plus auto fluorophores, ($\mu_a^{tissue} \gg \mu_a^{marker + autofluor}$), so that $\mu_a^{marker + autofluor}$ was negligible in calculating $D(\lambda)$, $\mu_t'(\lambda)$ and $\mu_{eff}(\lambda)$.

The standard values for optical properties of biological tissues were determined using the model by Svaasand *et al.* (21). According to this the parameters that dominate absorption

of human skin in the visible to near-infrared wavelength range are blood volume, blood oxygenation and melanin content.

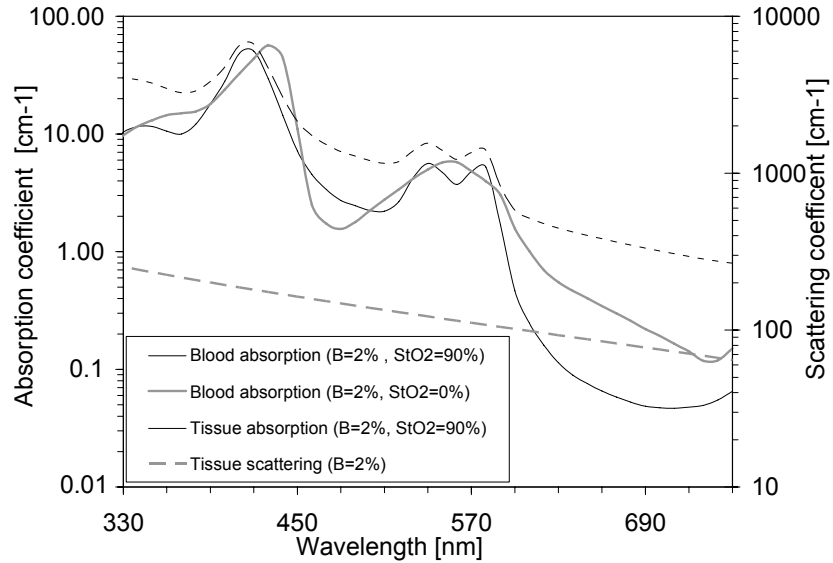


Fig. 1 Modeled absorption coefficient: for deoxygenated (grey line) and 90% oxygenated (solid line) blood, tissue (dashed), and the reduced scattering coefficient of tissue (grey dashed). The blood volume $B = 2\%$.

Since most tissues but skin do not contain melanin we here modified this model by decreasing the melanin content by a factor of 3 from that of Caucasian skin (@694nm), so that it here represents unknown absorbers. Hence, this modified model produces optical properties that are generally more representative of tissues that do not contain melanin (22) and at 630 nm were in the range of brain white matter (23). Fig. 1 shows the modeled values for the absorption of deoxy- and 90% oxygenated blood (standard), the tissue absorption with oxygenated blood, and the tissue scattering coefficient.

Table 2. Modeled fluorescence yields used in the different quantification methods.

M : marker fluorescence yield, A : autofluorescence yield

Marker	$\lambda_{ex}, \lambda_{em}$ [nm]	M [a.u]	A [a.u]
PpIX	406, 630	16	2
	436, 630	4	1.8
PC4	656, 710	4	0.2
	686, 710	16	0.18
DF	620, 700	16	0.22
	640, 700	4	0.20
	730, 800	16	0.15
	750, 800	4	0.13

The standard values for fluorescence yields $M(\lambda_{ex}, \lambda_{em})$ and $A(\lambda_{ex}, \lambda_{em})$ are listed in Table 2. These were assumed constant. Their relative magnitudes were estimated based on the excitation and emission spectra shown in Fig. 2. The standard values for the remaining parameters and the range over which they were varied are listed in Table 3. Listed values for

I , γ , η and C_a were chosen rather arbitrarily, as literature values are not widely available, however ranges for B , StO_2 and μ'_s span reported values for normal and cancerous tissues.

Table 3. Parameter standard values and the ranges over which they were varied

Parameter	Standard	Range	Unit	Ref.
I	100	30-100	mWcm ⁻²	(13)
γ, η	1.0	0.3-1.0	r.u.	(13)
C_m	0.01	fixed	M	-
C_a	0.01	0.002-0.02	M	(13)
B	2	1-10	%	(27)
StO_2	90	30-90	%	(27)
μ'_s	1.0	0.1-1.0	r.u.	(22)

Optical Phantoms

Experimental performance evaluation was conducted in tissue equivalent phantoms with Intralipid-20% as scattering media and Evans Blue as absorber. These were prepared with 3 different sets of μ_a and μ'_s at 630nm. Values are listed in Table 4 and fall within ranges used above for modeling. In these experiments I , γ and η were kept constant. PpIX (Sigma-Aldrich, Canada) was used as target fluorophore. Because of the hydrophobic nature of PpIX, prior to use the phantoms were shaken continuously for 72h to allow PpIX to bind to the lipids. The raw fluorescence and the signal output of Q_i were determined over a PpIX concentration range of 0.01-10 μ g/ml. Also, the lower detection limit of PpIX was investigated.

Table 4. Phantom optical properties at 630 nm.

Phantom	μ'_s [cm ⁻¹]	μ_a [cm ⁻¹]
1	15	0.25
2	30	0.5
3	60	1

Optical imaging was performed with a newly developed prototype fluorescence imaging system that was designed for clinical use. This is based around a 3-CCD compact surgical camera (DXC-C33, Sony, Canada). Multi-spectral images are acquired using the blue, green and red channels. The sensitivity towards the NIR can be extended by replacing the standard NIR cut-off filter. This camera features a frame rate of 30 frames/sec (NTSC), 796 x 494 pixels and 8 bit dynamic range. A standard clinical laparoscope with a liquid light guide coupled to the excitation light source is serving as excitation and entrance optics. A custom-made long-pass 500nm filter is placed between the camera and laparoscope. This purposely leaks a small fraction (10^{-4}) of the UV/blue excitation light (Chroma, US) for measurement of the diffuse reflectance. The custom-made excitation light source is a 300W Xeon arc lamp (Cermax, Perkin Elmer, US). A filter wheel containing 2 excitation filters (wavelengths listed in Table 1) spins at a frequency so that subsequent frames are excited with alternating wavelengths. The excitation irradiance with the filters is ~ 50 mW.cm⁻², at a typical working distance of 2 cm. The digital video output is captured by a computer (Intel, Pentium 4) and can be displayed on the monitors in the operating room for visualization to the surgeon, hence allowing surgical guidance. Image processing is performed with custom made software

(Hytek Automation, Waterloo, ON, Canada) that is based on LabVIEW™ (National Instruments, US).

A general problem with correction methods is that the structural/anatomical information is mostly lost. This is problematic when the images are used to guide biopsies or resect tumors. To alleviate this problem, the software allows to superimpose/overlay the corrected image on the raw fluorescence images in real-time, providing both structural information for orientation and functional information.

Clinical feasibility

Quantitative fluorescence imaging employing Q_i was performed in patients with prostate cancer undergoing radical prostatectomy. Approval for this study was obtained from the research ethics board of the University Health Network and patients agreed to participation by signing a consent form. This study is ongoing and to date 6 patients have been enrolled, hence the results obtained here are preliminary in nature and serve the purpose only of demonstrating clinical feasibility. To induce PpIX, 20 mg/kg 5-aminolevulinic acid (ALA) was administered orally in 50ml of orange juice 5-6 h prior to fluorescence imaging. We investigated feasibility of using Q_i in real time for image-guided surgery using the above described prototype imaging device.

Results

Model caclulations

The signal change due variations in one parameter, $SC_{parameter}$ and the total signal change, SC_{total} , due to variations in all parameters are listed in Table 5.

Table 5. The signal change due to variations in the individual parameters, $SC_{parameter}$, and the total signal change, SC_{total} for each method and each marker. γ : excitation geometry, η : collection efficiency, I : Irradiance, C_a : Autofluorescence, B : Blood volume, StO_2 : Oxygenation, μ_s' : Scattering, (Indep.: Independent by definition).

Method	Marker	Linear	$SC_{I,\gamma,\eta}$	SC_{C_a}	SC_B	SC_{StO_2}	$SC_{\mu_s'}$	SC_{total}
Q_{Raw}	PpIX	☑	3.33	1.22	4.47	1.07	1.14	245
Q_1	PpIX	☒	Indep.	1.23	1.03	1.17	1.07	1.59
Q_2	PpIX	☒	Indep.	1.24	1.21	1.77	1.12	2.97
Q_1	PC4	☒	Indep.	1.08	1.01	1.01	1.02	1.12
Q_3	Dual	☑	Indep.	1.07	1.05	1.05	1.04	1.23
Q_4	Dual	☑	Indep.	Indep.	1.02	1.05	1.04	1.11

Optical phantoms

In the tissue phantoms increasing signal was observed with increasing PpIX concentration for both the raw fluorescence and method Q_1 as shown in Fig. 3. The raw fluorescence signals in Fig. 3a demonstrate a large deviation in response between the 3 phantoms. At a PpIX concentration of 1.25 μ g/mg the maximum difference between phantom 1 and 3 is ~200%, confirming the need for correction methods. Fig. 3b shows the signal according to Q_i with obvious decreased deviation between the response curves. At 1.25 μ g/mg the maximum difference has decreased 10-fold to ~20%. At lower PpIX concentrations a plateau was reached that we interpreted as the lower detection limit as

indicated by the dashed lines in Fig. 3a. This plateau was not determined by camera noise, but by the autofluorescence of the phantom, as confirmed by switching off the excitation light.

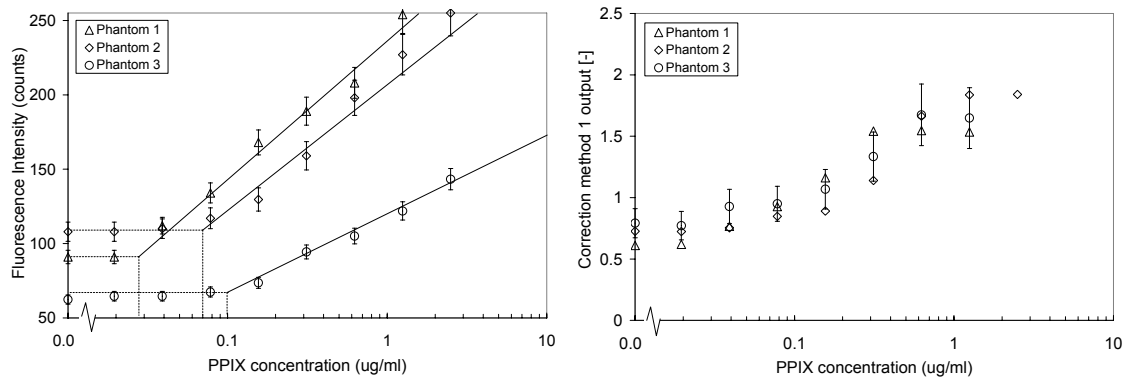


Fig 3. (a). raw fluorescence intensity vs. PpIX concentration for the 3 phantoms listed in Table 1. These have a large variation in response due to the different optical properties of these phantoms. The difference between phantom 1 and 3 at $1.25\mu\text{g/ml}$ PpIX is $\sim 200\%$. The lower detection limit of PpIX is indicated by the dashed lines. (b) The same data set as shown in (a) but now corrected according to Q_1 , note that the deviation between the response curves has decreased in (b) vs. (a) as the 3 separate curves of (a) have collapsed to one universal response curve, the difference between phantom 1 and 3 at $1.25\mu\text{g/ml}$ PpIX has decreased by a factor of 10 to $\sim 20\%$.

Clinical Feasibility

Intraoperatively, the capsule of the prostate also showed a green autofluorescence with small amounts of diffusely reflected UV/blue excitation light. Various areas with red fluorescence were found on the prostate capsule and surgical bed. A typical example is shown in Fig. 4. The device was able to compute, display and store method Q_1 in real time (30 frames/sec) without dropping frames.

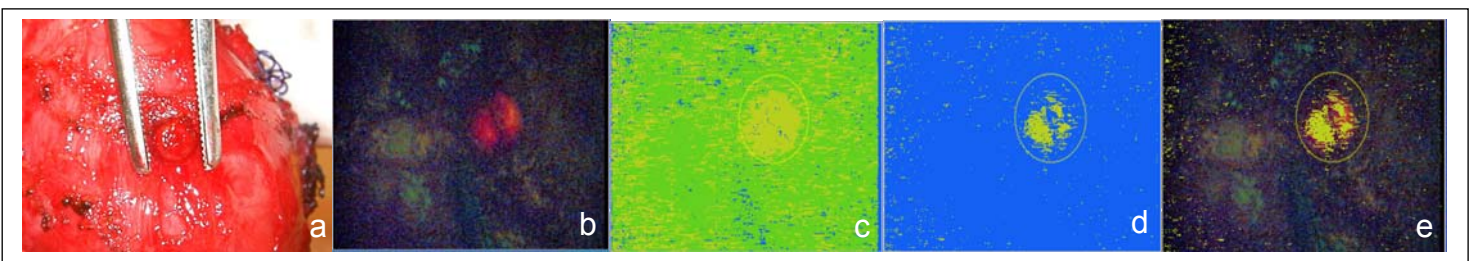


Fig. 4 (a) A white light image of the prostate capsule with forceps around a nodule. (b) The raw unprocessed raw fluorescence image showing small amounts of blue reflectance, green autofluorescence of the prostate capsule and bright red fluorescence of the nodule. (c) The same fluorescence image now made quantitative through image processing according to method Q_1 . As can be observed most of the anatomical/structural information is lost. To alleviate this problem this image is thresholded (blue = 0 intensity) as shown in (d) and overlaid on the raw fluorescence image so that the resulting (e) image contains both structural/anatomical information as well as functional quantitative information.

Discussion

Model Calculations

Method Q_1 demonstrated a quantification performance of $SC_{total} = 1.59$, which can be interpreted as a variation in the output signal of $\sim < \pm 30\%$. This is an improvement of more than 2 orders of magnitude as compared to the raw fluorescence ($SD_{total} = 245$) and in a similar performance range compared to the method by Sinaasappel *et al.* ($SD_{total} = 1.42$) (13). The advantage of Q_1 over this method is that less sensitive detectors with a lower dynamic range can be employed as it measures diffuse reflectance instead of autofluorescence.

The key to the high performance of Q_1 is the ratio that cancels out variations in irradiance, excitation geometry and collection efficiency. A small fraction of autofluorescence plus large fraction of marker fluorescence present in both numerator and denominator minimizes the dependence on variations in autofluorescence. Correction for optical properties is achieved by representing these equally in the numerator and denominator by combining fluorescence and reflectance. To demonstrate the effect of the reflectance term in Q_1 we also modeled the performance without it. We referred to this as Q_2 and the results are listed in Table 5. Q_2 had a decreased performance ($SC_{total} = 2.97$) as compared to Q_1 ($SC_{total} = 1.59$) demonstrating that use of the reflectance term minimizes the dependency on optical properties.

Optical phantoms

The quantification performance of Q_1 was evaluated experimentally in tissue equivalent phantoms employing a prototype fluorescence imaging system that was able to compute, display and store Q_1 in real-time. The results demonstrated that the response curve of the raw fluorescence *vs.* marker concentration was different for each of 3 phantoms confirming the need to correct for variations in optical properties. Employing Q_1 minimized this difference in the response by 10-fold, resulting in a more universal response curve demonstrating the ability of this method to correct for variations in tissue optical properties.

Clinical feasibility

We investigated the clinical feasibility of using Q_1 and the here developed prototype for image-guided surgery. Intraoperatively, six patients with prostate cancer undergoing radical prostatectomy were examined after ALA-induced PpIX administration with the purpose to detect fluorescence on the prostate capsule. Pathology and PpIX extraction data are not available at present as this trial is currently ongoing. However, the preliminary clinical results obtained here demonstrated that the device was capable of detecting diffuse reflectance, auto- as well as marker (PpIX) fluorescence, and can compute and display Q_1 in real-time (30frames/sec). As an additional feature the correction method can be overlaid on the raw uncorrected fluorescence image, in real time, essentially combining the structural anatomical information with the functional quantitative information.

Modifications

We choose PpIX as marker because it is currently in clinical use (14). Recently reported results of a Phase III trial in 270 patients demonstrated that fluorescence image guided resection of malignant gliomas doubled the 6 month progression free survival over resection under white light (15). Hence, PpIX fluorescence will likely form the baseline minimal signal strength that may be anticipated with novel molecular fluorescent markers.

Method Q_1 is modified below so it can be applied to such novel markers and the performance is evaluated through modeling as above.

The excitation and emission wavelengths used are listed in Table 1. Fluorescence yields are listed in Table 2 and were estimated from marker absorption and emission spectra available in the literature (16-18) and schematically shown in Fig. 2.

Method Q_1 can be used with markers that absorb and emit in the NIR range as phthalocyanine 4 (PC4) (16). Due to the decreased autofluorescence, blood absorption and scattering in the NIR the performance, further improved to $SC_{total} = 1.12$, as listed in Table 5.

As method Q_1 is based on a ratio on the maxima and minima of the absorption spectra, the response to the marker concentration is non-linear and reaches a plateau at higher concentrations, similar to the method by Sinaasappel *et al.* (24). Therefore, the concentration range that can be determined is limited and hence it would be beneficial to modify Q_1 such that it would have linear response to marker concentration. This can be achieved by using Q_1 in combination with recently reported dual fluorescent markers (17, 18). These are two markers with different absorption and emission spectra conjugated to a single targeting moiety, as shown in Fig 2. The fluorescence of one marker can vary to yield functional disease information, whereas the fluorescence of a second marker is used as reference and assumed constant. Placing their signal in the numerator and denominator of Q_1 respectively is referred to as Q_3 , the performance is $SC_{total} = 1.23$ as listed in Table 5 is in a similar range as compared to Q_1 with PC4, but has the additional advantage of a linear response to marker concentration.

Q_3 is dependent on variations in autofluorescence. This can be subtracted using the subtraction method of Baumgartner *et al.* (13, 25) (now widely used by Xenogen Corp. (26)), in both numerator and denominator, so that the method Q_4 is independent on variations

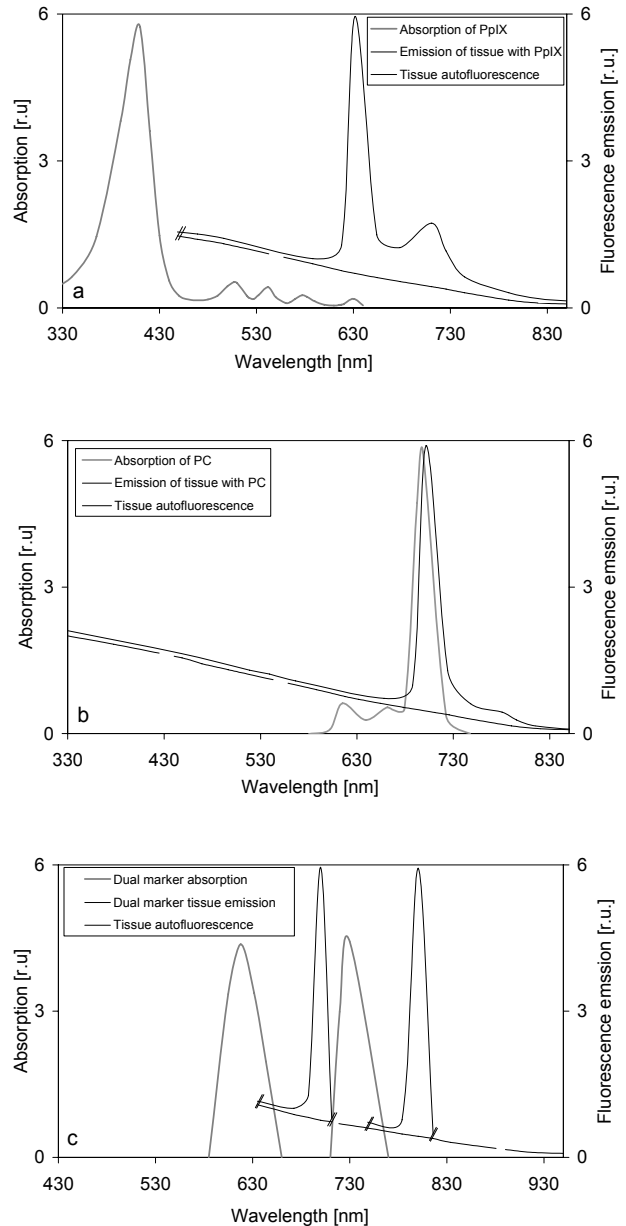


Fig. 2 Schematic excitation (grey line) and emission (black line) spectra of tissues containing the marker (a) Protoporphyrin IX (PpIX), (b) Phthalocyanine 4 (PC4) and (c) a Dual fluorescent marker (DM). The dashed line shows the tissue auto fluorescence.

in autofluorescence and the performance further improves to $SC_{total} = 1.11$. Details regarding modeling for this method can be found in ref. (13).

Note that, for fluorescence quantification with optimum accuracy, the fluorescent layer should be exposed to the tissue surface and should be thick relative to the penetration depth of light (13). Hence, UV/blue excitation light should be used for quantification of fluorescence in small lesions of a few mm in depth whereas far red/NIR light excitation can be used for thicker lesions. This because the effective penetration depth of UV *vs.* NIR light changes from the sub-millimeter range to several millimeters (22).

Conclusions

The modeling and optical phantom experiments demonstrated that the method introduced here substantially aids in the *in vivo* quantification performance over use of raw fluorescence signal. Due to its relative simplicity we also demonstrated it can be acquired, computed and displayed in real-time (30 frames/sec). The clinical feasibility of this was shown by using this method intra-operatively during radical prostatectomy of patients with prostate cancer.

Several modifications of this method are discussed so it can be used with NIR markers as phthalocyanine 4 (16) or with dual-fluorescent markers (17, 18). These offer additional advantages as they can be conjugated to various targeting moieties, provide a linear response to marker concentration and further minimize the dependence on autofluorescence, as demonstrated through modeling.

These methods could be of value for future clinical applications of molecular imaging, in particular diagnostic screening and image-guided surgery where real-time feedback and accurate quantification will be required to reveal functional disease information.

Hence, initial steps towards establishing the core methods and imaging technology needed for clinical *in vivo* real-time molecular imaging are presented. Major challenges remain in that future work should be directed towards experimental and clinical validation of this method for specific applications.

Acknowledgements

Development of methods and instrumentation in this investigation was supported by grant CA 43892 DHHS/NIH/NCI. The clinical trial in prostate was supported by NCIC/CPCRI IDEA grant # 014438. A. Bogaards was also supported in part by the Muzzo Fund of the Princess Margaret Hospital Foundation, the Dutch Technology Foundation, grant number AGN 3413 and the European commission, Contract number BMH4-CT97-2260. DUSA Pharmaceuticals NY kindly donated ALA.

References

1. Sullivan DC and Ferrari M (2004). Nanotechnology and tumor imaging: seizing an opportunity. *Mol Imaging*. **3**:364-9.
2. Cherry SR (2004). In vivo molecular and genomic imaging: new challenges for imaging physics. *Phys Med Biol*. **49**:R13-48.
3. Sokolov K, Aaron J, Hsu B, Nida D, Gillenwater A, Follen M, MacAulay C, Adler-Storthz K, Korgel B, Descour M, Pasqualini R, Arap W, Lam W, and Richards-Kortum R (2003). Optical systems for in vivo molecular imaging of cancer. *Technol Cancer Res Treat*. **2**:491-504.
4. Ntziachristos V, Schellenberger EA, Ripoll J, Yessayan D, Graves E, Bogdanov A, Jr., Josephson L, and Weissleder R (2004). Visualization of antitumor treatment by means of fluorescence molecular tomography with an annexin V-Cy5.5 conjugate. *Proc Natl Acad Sci U S A*. **101**:12294-9.
5. Brenton DJ, Carey LA, Ahmed AA, and Caldas C (2005). Molecular classification and molecular forecasting of breast cancer: ready for clinical application? *J Clin Oncol*. **23**:7350-7360.
6. Graves EE, Ripoll J, Weissleder R, and Ntziachristos V (2003). A submillimeter resolution fluorescence molecular imaging system for small animal imaging. *Med Phys*. **30**:901-11.
7. Mansfield JR, Gossage KW, Hoyt CC, and Levenson RM (2005). Autofluorescence removal, multiplexing, and automated analysis methods for in-vivo fluorescence imaging. *J Biomed Opt*. **10**:41207.
8. Gao X, Cui Y, Levenson RM, Chung LW, and Nie S (2004). In vivo cancer targeting and imaging with semiconductor quantum dots. *Nat Biotechnol*. **22**:969-76.
9. Troy T, Jekic-McMullen D, Sambucetti L, and Rice B (2004). Quantitative comparison of the sensitivity of detection of fluorescent and bioluminescent reporters in animal models. *Mol Imaging*. **3**:9-23.
10. Lim YT, Kim S, Nakayama A, Stott NE, Bawendi MG, and Frangioni JV (2003). Selection of quantum dot wavelengths for biomedical assays and imaging. *Mol Imaging*. **2**:50-64.
11. Bogaards A, Aalders MC, Zeyl CC, de Blok S, Dannecker C, Hillemanns P, Stepp H, and Sterenborg HJ (2002). Localization and staging of cervical intraepithelial neoplasia using double ratio fluorescence imaging. *J Biomed Opt*. **7**:215-20.
12. Flejou JF (2005). Barrett's oesophagus: from metaplasia to dysplasia and cancer. *Gut*. **54 Suppl 1**:i6-12.
13. Bogaards A, Sterenborg HJCM, and Wilson BC (2006). In vivo quantification of fluorescent molecular markers in real-time: a modeling study to evaluate the performance of five existing methods. *J Biomed Opt*. submitted.
14. Kelty CJ, Brown NJ, Reed MWR, and Ackroyd R (2002). The use of 5-aminolaevulinic acid as a photosensitiser in photodynamic therapy and photodiagnosis. *Photochem Photobiol Sci*. **3**:149-224.
15. Stummer W, Pichlmeier U, Meinel T, Wiestler OD, Zanella F, Reulen HJ, and group FtA-Gs (2006). Fluorescence-guided surgery with 5-aminolevulinic acid for resection of malignant glioma: a randomised controlled multicentre phase III trial. *Lancet Oncol*. **7**:392-401.

16. Li H, Marotta DE, Kim S, Busch TM, Wileyto EP, and Zheng G (2005). High payload delivery of optical imaging and photodynamic therapy agents to tumors using phthalocyanine-reconstituted low-density lipoprotein nanoparticles. *J Biomed Opt.* **10**:41203.
17. Kircher MF, Weissleder R, and Josephson L (2004). A dual fluorochrome probe for imaging proteases. *Bioconjug Chem.* **15**:242-8.
18. Kircher MF, Josephson L, and Weissleder R (2002). Ratio imaging of enzyme activity using dual wavelength optical reporters. *Mol Imaging.* **1**:89-95.
19. Wilson BC, Weersink RA, and Lilge L (2003). Fluorescence in Photodynamic Therapy Dosimetry. In *Handbook of biomedical fluorescence*. M. Mycek and B.W. Pogue, Eds. Marcel Dekker, Inc., New York. pp. 529-561.
20. Farrell TJ and Patterson MS (2003). Diffusion modeling of fluorescence in tissue. In *Handbook of biomedical fluorescence*. M. Mycek and B.W. Pogue, Eds. Marcel Dekker, Inc., New York. pp. 29-60.
21. Svaasand LO, Norvang LT, Fiskerstrand EJ, Stopps EKS, Berns MW, and Nelson JS (1995). Tissue parameters determining the visual appearance of normal skin and port-wine stain. *Lasers in Med Sci.* **10**:55-65.
22. Cheong W-F (1995). Appendix to chapter 8: Summary of optical properties. In *Optical-Thermal Response of Laser-Irradiated Tissue*. A.J. Welch and M.J.C. van Gemert, Eds. Plenum Press, New York. pp. 275-303.
23. Yavari N, Dam JS, Antonsson J, Wardell K, and Andersson-Engels S (2005). In vitro measurements of optical properties of porcine brain using a novel compact device. *Med Biol Eng Comput.* **43**:658-66.
24. Sinaasappel M and Sterenborg HJCM (1993). Quantification of the hematoporphyrin derivative by fluorescence measurement using dual-wavelength excitation and dual-wavelength detection. *Appl Opt.* **32**:541-548.
25. Baumgartner R, Fisslinger H, Jocham D, Lenz H, Ruprecht L, Stepp H, and Unsold E (1987). A fluorescence imaging device for endoscopic detection of early stage cancer--instrumental and experimental studies. *Photochem Photobiol.* **46**:759-63.
26. Choy G, Choyke P, and Libutti SK (2003). Current advances in molecular imaging: noninvasive in vivo bioluminescent and fluorescent optical imaging in cancer research. *Mol Imaging.* **2**:303-12.
27. van Veen RL, Sterenborg HJ, Marinelli AW, and Menke-Pluymers M (2004). Intraoperatively assessed optical properties of malignant and healthy breast tissue used to determine the optimum wavelength of contrast for optical mammography. *J Biomed Opt.* **9**:1129-36.

Chapter 8

Summary / Samenvatting

Summary

Fluorescent molecules, hereafter referred to as fluorophores, can be excited by illumination with light and subsequently can de-excite into the ground state through, amongst others possibilities, emission of fluorescence. In case the fluorophore is selectively taken up by the cancer and not by surrounding normal tissues the fluorescence may thus be used for the detection and localization of cancers.

The research described in this thesis focuses on the development of methods and technology for real-time *in vivo* fluorescence imaging for cancer detection and image-guided surgical tumor resection. Subsequently, the introduced methods and technology are evaluated through modelling studies and validated with pre-clinical experiments and clinical trials in patients.

After a general introduction in **Chapter 1**, **Chapter 2** describes the development of a fluorescence imaging device for the detection of superficial cancer based on the Double Ratio technique. In practical use this device resembles an operation microscope and can be used in a clinical environment. This device acquires 4 different fluorescence images excited at two wavelengths each detected at two wavelengths. From these images it calculates, displays and stores Double Ratio images at a maximum speed of 1Hz. The Double Ratio image gives the distribution of the fluorophore amount present in tissue and is not affected by local variations in tissue optics, i.e. tissue absorption and tissue scattering. The validity of the technique was confirmed here by *ex vivo* tissue equivalent phantom experiments using hematoporphyrin and *in vivo* experiments on normal pigmented moles on Caucasian human skin using aminolevulinic acid (ALA) induced protoporphyrin IX (PpIX) as the fluorophore of interest.

In **Chapter 3** we investigated if the device described in Chapter 2 could be used as an imaging technique for the diagnoses of cervical intraepithelial neoplasia (CIN) in patients. For this purpose we performed a clinical trial, enrolling 38 patients. PpIX was induced by topical application of ALA, 16 of 38 patients were colposcopically selected for biopsy. Of these 16 patients fluorescence images were taken and 19 sites were biopsied and the disease was staged histopathologically. Fluorescence imaging of the cervix was cumbersome but feasible. In 4 cases strongly localized fluorescent hotspots were observed at the location where the disease was colposcopically visible. In the other cases the fluorescence showed a more diffuse multi-focal image. The value of the DR determined at the site of biopsy correlated in a statistically significant way with the histopathologically determined stage of the disease (Spearman rank correlation, $r = 0.881$, $p < 0.001$ (confidence interval 0.7044 - 0.9552)). The results indicate that not only detection of CIN was possible but, interestingly, also suggests that non-invasive staging of CIN using this technique appears feasible.

The hypothesis of the study described in **Chapter 4** is that fluorescence image-guided brain tumor resection can assist neurosurgeons by visualizing tumor margins that merge imperceptibly into normal brain tissue and, hence, are difficult to identify. To test this hypothesis we performed a pre-clinical study in which we compared residual tumor, determined by histopathology, after white light resection (WLR) using an operating

microscope versus additional fluorescence guided resection (FGR). For this, we used a rabbit model with intracranial VX2 tumor. Using a fluorescence imaging system we detected the fluorescence of ALA induced PpIX at 4 h before surgery. The results demonstrated that using FGR in addition to WLR significantly decreased the amount of residual tumor post resection by a factor 16 from $32\% \pm 38\%$ to $2.0\% \pm 3.5\%$ of the initial tumor volume. Based on these results we concluded that adjuvant FGR significantly decreases residual tumor and enabled consistent resection completeness for all cases.

Fluorescence-guided resection (FGR) and photodynamic therapy (PDT) have previously been investigated separately with the objectives, respectively, of increasing the extent of tumour resection and of selectively destroying residual tumour post resection. Both techniques have demonstrated trends towards improved survival, pre-clinically and clinically. In **Chapter 5** we hypothesize that combining these techniques will further delay tumour re-growth. In order to demonstrate technical feasibility of this approach, we used the same model as described under chapter 4, the rabbit with intracranial VX2 tumor. An operating microscope was used for white light imaging and the fluorescence imaging device described in Chapter 4 was used for FGR. PDT treatment light was applied by intracranially-implanted light emitting diodes (LED). The fluorescent photosensitizer used for both FGR and PDT was ALA-induced PpIX. For PDT, ALA (100mg/kg) and low light doses (15 and 30J) were administered over extended periods, which we refer to as metronomic PDT (mPDT).

18 tumour bearing rabbits were divided equally into 3 groups: controls (no resection); FGR; and FGR followed by mPDT. Histological whole brain sections (H&E stain) showed primary and recurrent tumours. No bacteriological infections were found by Gram staining. Selective tumour cell death through mPDT-induced apoptosis was demonstrated by TUNEL stain. These results demonstrate that the combined treatment is technically feasible and this model is a candidate to evaluate it. Further optimization of mPDT treatment parameters (drug/light dose rates) is required to improve survival.

More recent research is shifting the focus towards novel fluorescent markers that use active targeting strategies. Recent advances in nanotechnology and increasing knowledge of genes and proteins associated with cancers has enabled the engineering of nanoparticles that comprise a targeting moiety (e.g. antibodies, antibody fragments, peptides) conjugated to a fluorescent marker. These particles hold promise to have an increased, more stable spectral intensity and improved tumor specificity compared with passive-targeting fluorescent markers. In addition to providing information about the presence or absence of disease, as was typically the case for passive-targeting markers, active-targeting markers can also yield functional disease information about physiological and molecular processes that relate to the invasiveness, progression and treatment response of the disease

The ability to accurately quantify the *in vivo* measured marker fluorescence is critical to unravel functional disease information. However, quantification of optically measured fluorescence signals is a major challenge because the measured signals are strongly influenced by various secondary parameters. Over the last 2 decades several methods have been reported for quantification of passive-targeting fluorescent markers. These methods may be applied to imaging of novel, more tumor specific, active-targeting fluorescent markers. However, an objective comparison of these methods has not been reported.

Therefore, in **Chapter 6**, we evaluate the performance of quantification methods for surface imaging that use continuous wave excitation (since these can be computed in real-

time and thus be used for diagnostic screening and image guided surgery). Each method was described by an analytical solution to the diffusion equation and the input parameters, irradiance, excitation geometry, collection efficiency, autofluorescence, melanin content, blood content, blood oxygenation and tissue scattering were varied over a range that can be expected during *in vivo* imaging, using optical properties resembling human skin containing a porphyrin-like target fluorophore.

The uncorrected fluorescence signal changed by more than 3 orders of magnitude. The method of Saarnak *et al.* did not change and hence corrects entirely, but requires a constant geometry before and after administration of the fluorescent molecule. The method of Sinaasappel *et al.* resulted in a maximum uncertainty of $\pm 20\%$ in the fluorescence signal. Hence, these methods can aid in more accurate real-time quantification of active-targeting fluorescent markers.

As described in Chapter 6 a major challenge is accurate quantification of the *in vivo* fluorescence signal in real-time. To address this problem, in **Chapter 7**, a ratiometric quantification method is introduced. Through mathematical modeling the performance was evaluated using optical properties that resembled biological tissues with the fluorescent marker Protoporphyrin IX. Experimentally the performance was evaluated in optical phantoms with different optical properties employing a prototype fluorescence imaging system. The clinical feasibility of real-time, image-guided surgery was demonstrated in patients undergoing prostatectomy.

The modeling and optical phantom experiments demonstrated that this method substantially aids in the *in vivo* quantification performance over the use of existing ratiometric methods. We also demonstrated that this method can be acquired, computed and displayed in real-time (30 frames/sec) in patients undergoing radical prostatectomy.

Discussed are the reasons why the introduced method leads to an increased quantification performance followed by modifications so it can be applied to novel fluorescent molecular markers as phthalocyanine 4 and dual-fluorescent markers. These offer additional advantages as these can provide a linear response to marker concentration and further minimize the dependence on autofluorescence and optical properties, as demonstrated through modeling.

Hence, we made initial steps towards establishing the core methods and imaging technology needed for clinical *in vivo* real-time fluorescence molecular imaging. Major challenges remain in that future work should be directed towards experimental and clinical validation of these methods for specific clinical applications.

Samenvatting

Fluorescerende moleculen, hierna fluoroforen genoemd, kunnen door bestraling met licht in een geëxciteerde toestand gebracht worden, waarna ze terug kunnen vallen in de grondtoestand via onder andere emissie van fluorescentie. Indien de fluorofoor selectief opgenomen wordt door kankercellen, en niet door omliggend normaal weefsel, zou detectie van de fluorescentie dus gebruikt kunnen worden voor kankerdetectie.

Dit proefschrift richt zich op de ontwikkeling van momenteel niet aanwezige methodes en technieken voor *in vivo* kwantitatieve beeldvorming van de fluorescentie voor kankerdetectie en resectie van tumoren. De geïntroduceerde methodes en technieken worden vervolgens geëvalueerd met modelstudies en gevalideerd met pre-klinische experimenten en met klinisch onderzoek in patiënten.

Na een algemene introductie in **Hoofdstuk 1** beschrijft **Hoofdstuk 2** de ontwikkeling van een fluorescentiebeeldvormingssysteem voor de detectie van oppervlakkige tumoren gebaseerd op de Dubbele Ratio-methode. In de praktijk lijkt dit systeem op een operatiemicroscoop en kan gebruikt worden in een klinische omgeving. Het systeem detecteert vier verschillende fluorescentiebeelden, geëxciteerd en gedetecteerd met twee verschillende golflengtes licht. Gebaseerd op deze beelden wordt het Dubbele Ratio-beeld berekend en weergegeven, met een maximum beeldfrequentie van 1 Hz. Het Dubbele Ratio-beeld geeft de distributie van de fluorofoor in weefsel weer en is onafhankelijk van lokale variaties in de weefseloptica, d.w.z. weefselabsorptie en -verstrooiing. De geldigheid van de methode was eerder bevestigd door *i) ex vivo* experimenten in weefselsimulerende fantomen, gebruik makend van de fluorescentiemarker hematoporphyrine-derivaat, en *ii) in vivo* experimenten in mensen met gepigmenteerde moedervlekken op een lichte huid. Daarbij werd de marker protoporphyrine IX (PpIX) gebruikt, die werd aangemaakt door topicale toediening, oftewel via de huid, van aminolevulinezuur (ALA).

In **Hoofdstuk 3** onderzoeken we of het systeem beschreven in Hoofdstuk 2 gebruikt zou kunnen worden voor de diagnose van cervicale intraepitheliale neoplasia (CIN), oftewel voorstadia van baarmoederhalskanker, in patiënten. Hiervoor is een klinische onderzoek uitgevoerd in 38 patiënten. PpIX werd ingebracht door topicale toediening van ALA. Met behulp van een colposcopie (kijkonderzoek) werden 16 van de 38 patiënten geselecteerd voor biopsie. Uit die 16 patiënten werden 19 biopten (stukjes weefsel) genomen, waarvan werd bepaald in welk stadium van kwaadaardigheid (maligniteit) ze verkeerden door middel van microscopisch onderzoek (histopathologie). Fluorescentiebeeldvorming was niet eenvoudig maar wel haalbaar. In vier patiënten observeerden we sterk gelokaliseerde fluorescentie op een locatie waar de maligniteit zichtbaar was met colposcopie. In de andere gevallen gaf het fluorescentiebeeld een meer diffuus en multifocaal beeld weer. De grootte van het Dubbele Ratio-sigitaal zoals bepaald op de locatie van het biopt correleerde met de graad van de maligniteit zoals bepaald door histopathologie. Deze correlatie was significant (Spearman rank correlatie, $r = 0.881$, $p < 0.001$ (zekerheidsinterval 0.7044-0.9552)). Deze resultaten demonstreren dat niet alleen detectie van een kwaadaardige afwijking mogelijk is met deze methode, maar dat ook het graderen van de maligniteit haalbaar lijkt.

De hypothese van het werk beschreven in **Hoofdstuk 4** is dat fluorescentiebeeldvorming de neurochirurg tijdens tumorresectie kan helpen bij het visualiseren van tumorgrenzen. De tumoren dringen namelijk onzichtbaar door in het normale hersenweefsel, waardoor ze moeilijk te identificeren zijn. De hypothese is getest door het uitvoeren van een pre-klinische studie. Daarbij bepaalden we met histopathologie het tumorresidu na resectie onder wit licht met een operatiemicroscop en vergeleken dat met het tumorresidu na witlichtresectie gevolgd door fluorescentie-geassisteerde tumorresectie (FGR). Hiervoor gebruikten we een konijnmodel met intracraniale VX2-tumor. Met een fluorescentiebeeldvormingssysteem exciteerden en detecteerden we de fluorescentie van PpIX, die aangemaakt was na toediening van ALA vier uur voor de tumorresectie. De resultaten laten zien dat, gebruik makend van FGR na de witlichtresectie, het tumorresidu dat achterblijft na resectie significant afneemt met een factor 16, namelijk van $32\% \pm 38\%$ naar $2.0\% \pm 3.5\%$ van het initiële tumorvolume. Gebaseerd op deze resultaten concluderen wij dat FGR leidt tot een significante afname van het tumorresidu.

Fluorescentie-geassisteerde resectie (FGR) en fotodynamische therapie (PDT) zijn eerder apart onderzocht met als doel respectievelijk een kleiner tumorresidu en het selectief vernietigen van tumorresidu. De pre-klinische en klinische resultaten van beide technieken hebben, apart van elkaar, trends laten zien die wijzen op een verbeterde prognose. In **Hoofdstuk 5** introduceren we de hypothese dat het combineren van deze technieken leidt tot het verder vertragen van teruggroei van de tumor. Om de haalbaarheid van deze combinatie aan te tonen, maakten wij gebruik van hetzelfde model als beschreven in Hoofdstuk 4, namelijk het konijnmodel met intracraniale VX2-tumor. Een operatiemicroscop werd gebruikt voor resectie onder wit licht en hetzelfde systeem als beschreven onder Hoofdstuk 4 werd gebruikt voor FGR. De lichtdosis benodigd voor PDT werd toegediend met behulp van lichtgevende diodes (LEDs). De lichtgevoelige stof gebruikt voor FGR en PDT was PpIX, geïnduceerd door ALA. Voor PDT werden ALA (100 mg/kg) en lage lichtdoses (15 en 30 J) toegediend gedurende lange periodes. We refereren hiernaar als metronomische PDT (mPDT). Achttien tumordragende dieren werden gelijkelijk verdeeld over drie groepen: een controlegroep (geen resectie), FGR, en FGR gevolgd door mPDT.

Histologie van complete secties van het brein (H&E) toonden primaire en teruggroeiende tumoren aan. Met Gram-kleuring werden geen bacteriologische infecties aangetoond. Selectieve dood van tumorcellen werd gedemonstreerd met behulp van confocale microscopie en TUNEL-kleuring. Deze resultaten tonen aan dat de gecombineerde behandeling technisch haalbaar is en dat dit diermodel een kandidaat is voor evaluatie van de combinatiebehandeling. Verdere optimalisatie van de mPDT behandelingsparameters is nodig om de prognose te verbeteren.

Meer recent onderzoek richt zich op nieuwe fluorescentiemarkers die gebruik maken van actief-doelzoekende strategieën. Recente vooruitgang in de nanotechnologie en een toenemende kennis van genen en eiwitten die geassocieerd worden met kanker hebben er toe geleid dat nanodeeltjes gemaakt kunnen worden die bestaan uit een doelzoekend deel (bijv. antilichamen, antilichaamfragmenten, peptides) gebonden aan een fluorescerende marker. Deze deeltjes beloven een toegenomen, meer stabiele spectrale intensiteit en verbeterde tumorselectiviteit vergeleken met passief-doelzoekende markers.

Behalve informatie over de aanwezigheid van kanker, zoals meestal het geval voor passief-doelgerichte markers, kunnen actief-doelgerichte markers ook informatie op

functioneel moleculair niveau geven over de gradering van de ziekte, ziektemechanismen, de prognose van de patiënt en de behandelingsrespons. Om dit soort functionele informatie te kunnen achterhalen is het kwantificeren van het *in vivo* fluorescentiesignaal essentieel. Accurate kwantificatie van *in vivo* gemetenfluorescentie vormt echter een uitdaging, omdat het gemeten signaal sterk afhangt van diverse secundaire parameters. In de laatste 20 jaar zijn verschillende correctiemethodes gerapporteerd voor de beeldvorming van passief-gerichte fluoroforen. Deze methodes kunnen wellicht ook gebruikt worden voor het kwantificeren van actief-gerichte fluoroforen. Een objectieve vergelijking van deze methodes is echter nog niet gerapporteerd.

Daarom evalueren we in **Hoofdstuk 6** de kwantificeringsprestaties van methodes die geschikt zijn voor oppervlakkige beeldvorming en die gebruik maken van continue excitatie. We beschreven elke methode met een analytische oplossing van de diffusietheorie. De invoerparameters: irradiantie, excitatiegeometrie, collectie-efficiëntie, autofluorescentie, de hoeveelheid melanine, bloedvolume, bloedoxygenatie en de weefselverstrooiing, werden gevarieerd over een bereik zoals dat verwacht kan worden tijdens *in vivo* beeldvorming. We maakten daarbij gebruik van de optische eigenschappen van menselijke huid die een porfyrine-achtige fluorofoor bevatte.

Het ongecorrigeerde fluorescentiesignaal veranderde meer dan drie ordes van grootte. Met de methode van Saarnak *et al.* veranderde het fluorescentiesignaal niet en was de correctie dus compleet, maar deze methode vereist een identieke geometrie voor en na toediening van de fluorofoor. De methode van Sinaasappel *et al.* resulteerde in een onzekerheid in het fluorescentiesignaal van maximaal $\pm 20\%$.

Deze methodes kunnen dus gebruikt worden voor verbetering van de kwantificatienauwkeurigheid van nieuwe actief-gerichte fluoroforen.

Zoals beschreven in Hoofdstuk 6 vormt accurate *in vivo* kwantificatie van het gemeten fluorescentiesignaal een uitdaging. Om dit probleem aan te pakken wordt in **Hoofdstuk 7** een kwantificatie methode geïntroduceerd. De kwantificatieprestaties werden geëvalueerd door te modelleren gebruik makend van optische eigenschappen die overeenkwamen met biologisch weefsel, en de fluorescerende marker protoporphyrine IX.

De kwantificatieprestatie werd experimenteel geëvalueerd in optische fantomen met een prototype fluorescentiebeeldvormingssysteem. Dit apparaat kan de methode berekenen en weergeven met directe terugkoppeling. De klinische haalbaarheid van het gebruik van deze methode en prototype voor beeldvorming-geassisteerde chirurgie werd onderzocht in patiënten met prostaatkanker.

In de discussie wordt besproken waarom deze methode leidt tot een verbetering in the kwantificatieprestatie. Ook worden modificaties gepresenteerd zodat deze methode toegepast kan worden met nieuwe actief-doelgerichte markers zoals phthalocyanine 4 en dubbel-fluorescerende markers. De toegevoegde waarde hiervan is dat deze een lineaire response hebben ten opzichte van de marker concentratie en de invloed van autofluorescentie en optische eigenschappen minimaliseren. Dit werd gedemonstreerd door te modelleren.

Concluderend hebben we de eerste stappen gezet in de ontwikkeling van basismethodes en beeldvormingstechnologie die vereist zijn voor klinische *in vivo* moleculaire beeldvorming. De grote uitdaging waarop toekomstig werk zich zou moeten richten is het experimenteel en klinisch valideren van de hier geïntroduceerde methodes en technieken.

Chapter 9

General Discussion

General Discussion

Over the course of this PhD research several significant advances have been made in the field of optical fluorescence imaging for biomedical applications.

Optical imaging of fluorescent markers will likely soon have an impact on clinical practice. This primarily because a European group recently completed a multi-centre Phase III trial in 270 patients. Here fluorescence-image guidance was investigated for the resection of malignant gliomas, using the fluorescent marker PpIX. Their results demonstrated that patients allocated to fluorescence guidance had double the 6-month progression free survival rates as compared to those allocated to white light (41.0% [32.8-49.2] *vs* 21.1% [14.0-28.2]; difference between groups 19.9% [9.1-30.7], $p=0.0003$, Z test) (1). These results may be strong enough to warrant the first regulatory approval of fluorescence guided resection in oncology in the near future.

Further, the interest in optical imaging of fluorescent markers *in vivo* has tremendously increased. What less than 10 years ago was a relatively small research field, is now a very rapidly evolving field (2). What spiked this interest are recent advances in nanotechnology and increasing knowledge of genes and proteins associated with cancers. This combination has led to the development of engineered nanoparticles that comprises a fluorescent marker and a targeting moiety. Such active-targeting fluorescent markers hold promise to have an increased more stable spectral intensity and improved tumor specificity over previous passive-targeting makers (3). At the fluorescent marker end, various strongly fluorescent organic dyes have been synthesized (4, 5) as well as nanocrystals that have a high spectral intensity and allow tuning of the emission wavelength (6). Further, various ‘smart’ fluorescent markers have been developed. Some markers can be switched on in the presence of an enzyme (7), while others are self-illuminating and do not require external excitation light (8). Onto the same targeting moiety, there is also potential for combining fluorescent markers with MR-, PET-, SPECT- and US sensitive (nano)particles for multi-modality imaging (9). As for the targeting moiety, an increasing amount of molecular markers continue to be reported on almost a daily basis. Hence, the combinations of fluorescent markers and targeting moieties seem to offer endless new opportunities that are currently largely unexplored.

Besides yielding information about the presence or absence of disease (as was typically the case for passive-targeting fluorescent markers) various active-targeting markers also allow real-time *in vivo* monitoring of disease progression, response to treatment and reveal information about the stage of the disease, disease mechanisms and various prognostic factors (10). The ability to measure functional disease information *in vivo*, in real-time is quite revolutionary. Prior to the availability of these markers it was simply not feasible to measure such information *in vivo* and could only be approximated by *ex vivo* techniques.

As this field is yet only in its infancy, it is not clear what implications these advances will have long-term. It is, however, highly anticipated that an *in vivo* imaging of receptor-targeted-fluorescent markers will find wide application in drug discovery, immunology, cancer research and clinical practice (3).

For this to happen, one challenge is that these advances in active-targeting fluorescent markers will need to be matched by appropriate imaging methods and technologies designed optimally for specific applications. In this thesis we have made significant contributions to this challenge. Specifically, we have investigated existing and developed novel methods for *in vivo* quantification of fluorescent markers in real-time. This is of value as fluorescence quantification is critical to yield reliable functional disease information. Evaluation of the quantification performance was performed through mathematical modeling and via *in vivo* preclinical models. The feasibility of using these methods for diagnostic screening and surgical guidance was demonstrated in patients during clinical pilot studies.

Throughout this thesis we have shown that the quantification methods introduced here significantly improve the fluorescence image quantification over the current state of the art. Hence, these methods may find acceptance in those applications where *in vivo* real-time fluorescence quantification is critical, as diagnostic screening and image-guided surgery.

Ongoing clinical trials with the methods and technology developed herein will, a) validate the utility of fluorescence imaging in tumor detection and guided surgery, b) determine the efficacy and possible limitations of current fluorescent markers, and c) establish the core imaging hardware/software technology platform and algorithms needed for clinical *in vivo* fluorescent molecular imaging.

Imagine all the possibilities of fluorescence imaging and one comes to realize that there is an exciting and brightly fluorescing future ahead of us !

References

1. W. Stummer, U. Pichlmeier, T. Meinel, O. D. Wiestler, F. Zanella, H. J. Reulen, F. t. A.-G. s. group, "Fluorescence-guided surgery with 5-aminolevulinic acid for resection of malignant glioma: a randomised controlled multicentre phase III trial," *Lancet Oncol* **7**(5), 392-401 (2006).
2. V. Ntziachristos, J. Ripoll, L. V. Wang, R. Weissleder, "Looking and listening to light: the evolution of whole-body photonic imaging," *Nat Biotechnol* **23**(3), 313-20 (2005).
3. D. C. Sullivan, M. Ferrari, "Nanotechnology and tumor imaging: seizing an opportunity," *Mol Imaging* **3**(4), 364-9 (2004).
4. A. Nakayama, F. del Monte, R. J. Hajjar, J. V. Frangioni, "Functional near-infrared fluorescence imaging for cardiac surgery and targeted gene therapy," *Mol Imaging* **1**(4), 365-77 (2002).
5. A. Zaheer, R. E. Lenkinski, A. Mahmood, A. G. Jones, L. C. Cantley, J. V. Frangioni, "In vivo near-infrared fluorescence imaging of osteoblastic activity," *Nat Biotechnol* **19**(12), 1148-54 (2001).
6. W. C. Chan, D. J. Maxwell, X. Gao, R. E. Bailey, M. Han, S. Nie, "Luminescent quantum dots for multiplexed biological detection and imaging," *Curr Opin Biotechnol* **13**(1), 40-6 (2002).
7. R. Weissleder, C. H. Tung, U. Mahmood, A. Bogdanov, Jr., "In vivo imaging of tumors with protease-activated near-infrared fluorescent probes," *Nat Biotechnol* **17**(4), 375-8 (1999).
8. M. K. So, C. Xu, A. M. Loening, S. S. Gambhir, J. Rao, "Self-illuminating quantum dot conjugates for in vivo imaging," *Nat Biotechnol* **24**(3), 339-43 (2006).
9. S. R. Cherry, "In vivo molecular and genomic imaging: new challenges for imaging physics," *Phys Med Biol* **49**(3), R13-48 (2004).
10. K. Sokolov, J. Aaron, B. Hsu, D. Nida, A. Gillenwater, M. Follen, C. MacAulay, K. Adler-Storthz, B. Korgel, M. Descour and others, "Optical systems for in vivo molecular imaging of cancer," *Technol Cancer Res Treat* **2**(6), 491-504 (2003).

Curriculum Vitae

Arjen Bogaards was born on May 28th 1974 in Goes, the Netherlands.

Arjen Bogaards studied Applied Physics at the Rijswijk Institute of Technology in Rijswijk, the Netherlands. In 1997 he obtained a Bachelors degree in Engineering Physics with a major in Photonics. The graduation research for this took place at the National Institute of Water and Atmospheric Research (NIWA) in Lauder, New Zealand under supervision of Dr. R. McKenzie. The thesis title was “Development of entrance optics for Solar UV measurements”.¹ In 1998 he worked for IBM Global Services in the Netherlands as an IT Specialist. Aiming to persue a more meaningful career, in 1999 Arjen started his scientific research by joining the Photodynamic Therapy and Optical Spectroscopy programme at the Erasmus Medical Centre in Rotterdam, the Netherlands under supervision of Dr. Ir. H.J.C.M. Sterenborg. Here, he researched optical imaging of fluorescent markers with the purpose of *in vivo* cancer detection. During this research a prototype imaging system was developed and was taken from the bench top to the clinic and the results are described in this thesis. An opportunity arose in 2001 in Toronto, Canada within the Department of Medical Biophysics at the University of Toronto under supervision of Prof. Dr. B.C. Wilson where he continued this research. In this period Arjen also became more involved in researching Photodynamic Therapy (PDT) as an experimental treatment for cancer. Recently, Arjen was hired by Steba and Negma, a Biotechnology and Pharmaceutical company, respectively, whom intend to commercialize PDT for the treatement of prostate cancer and other indications.² In his new role as Chief Technology Officer (CTO), Arjen aims to push PDT into clinical practice over the next five years.

¹Partly available through: <http://www.niwascience.co.nz/rc/instruments/lauder/ptfe>

²More information can be found on: <http://www.prostatepdt.com>

Scientific output

Peer reviewed publications

1. Bogaards A, Aalders MC, Jongen AJL, Dekker E, and Sterenborg HJCM (2001) "Double ratio fluorescence imaging for the detection of early superficial cancers." *Rev Sci Instrum.* **72**: 3956-3961.
2. Bogaards A, Aalders MC, Zeyl CC, de Blok S, Dannecker C, Hillemanns P, Stepp H, Sterenborg HJCM (2002) "Localization and staging of cervical intraepithelial neoplasia using double ratio fluorescence imaging." *J Biomed Opt.* **7**:215-20.
3. Bogaards A, Varma A, Collens SP, Lin A, Giles A, Yang VX, Bilbao JM, Lilge LD, Muller PJ, Wilson BC. (2004) "Increased brain tumor resection using fluorescence image guidance in a preclinical model." *Lasers Surg Med.* **35**:181-90.
4. Bogaards A, Varma A, Zhang K, Zach D, Bisland SK, Moriyama EH, Lilge L, Muller PJ and Wilson BC (2005) "Fluorescence image-guided brain tumour resection with adjuvant metronomic photodynamic therapy: pre-clinical model and technology development" *Photochem Photobiol Sci.* **4**: 438-42.
5. Bisland SK, Lilge L, Lin A, Rusnov R, Bogaards A, Wilson BC. (2004) "Metronomic Photodynamic Therapy as a New Paradigm for Photodynamic Therapy: Rationale and Preclinical Evaluation of Technical Feasibility for Treating Malignant Brain Tumors." *Photochem Photobiol.* **80**:22-30.
6. Siewerdsen JH, Moseley DJ, Burch S, Bisland SK, Bogaards A, Wilson BC, Jaffray DA. (2005) "Volume CT with a flat-panel detector on a mobile, isocentric C-arm: pre-clinical investigation in guidance of minimally invasive surgery." *Med Phys.* **32**:241-54.
7. Weersink R, Bogaards A, Gertner M, Davidson SRH, Zhang K, Netchev G, Trachtenberg J, Wilson BC (2005) "Techniques for delivery and monitoring of TOOKAD (WST09)-mediated photodynamic therapy of the prostate: Clinical experience and practicalities" *J. Photochem Photobiol B: Biol.* **79**:211-22.
8. Burch S, Bogaards A, Siewerdsen JH, Moseley DJ, Yee A, Finkelstein J, Weersink RA, Wilson BC, Bisland SK (2005) "Photodynamic therapy for the treatment of metastatic lesions in bone: Studies in rat and porcine models" *J Biomed Optics.* **10**:1-13.
9. Burch S, Bisland SK, Bogaards A, Yee AJM, Whyne CM, Finkelstein JA, Wilson BC (2005) "Photodynamic therapy for the treatment of vertebral metastases in a rat model of human breast carcinoma" *J Orthop Res.* **23**:995-1003.
10. Pinthus JH, Bogaards A, Weersink R, Wilson BC Trachtenberg J (2005) "Photodynamic Therapy for urological malignancies: past to current approaches" *J Urolog.* **175**:1201-1207.
11. Haider MA, Davidson SRH, Kale AV Weersink RA, Evans AJ, Toi A, Gertner M, Bogaards A, Wilson BC, Trachtenberg (2006) "Photodynamic therapy of Localized Recurrence of Prostate Cancer after Radiation using TOOKAD (WST09): MRI Assessment of Therapeutic Response" *Radiology*, *accepted*.
12. Bogaards A, Sterenborg HJCM, Wilson BC (2006) "In vivo quantification of fluorescent molecular markers in real-time: a modeling study to evaluate the performance of five existing methods" *J. Biomed Optics*. *submitted 2006*.
13. Bogaards A, Sterenborg HJCM, Trachtenberg J, Wilson BC, Lilge L (2006) "In vivo quantification of fluorescent molecular markers in real-time by ratio imaging for diagnostic screening and image-guided surgery" *Manuscript in progress 2006*.

Conference Proceedings

1. Bogaards A, Jongen AJ, Dekker E, van den Akker H, Sterenborg HJCM (2000) "Design and performance of a real-time double-ratio fluorescence imaging system for the detection of early cancers" *Proc. SPIE* Vol. 3917, p.2-8.
2. Muller PJ, Wilson BC, Lilge L, Yang VX, Varma A, Bogaards A, Hetzel FW, Chen Q, Fullagar F, Fenstermaker R, Selker R, Abrams J (2003) "Clinical studies of photodynamic therapy for malignant brain tumors: Karnofsky score and neurological score in patients with recurrent gliomas treated with Photofrin PDT" *Proc. SPIE*, Vol. 4612 p40-47.
3. Wilson BC, Bisland SK, Bogaards A, Lin A, Moriyama EH, Zhang K, Lilge L (2003) "Metronomic photodynamic therapy (mPDT): concepts and technical feasibility in brain tumor" *Proc. SPIE* Vol. 4952 p23-31.
4. Moriyama EH, Bisland SK, Lin A, Bogaards A, Lilge L, Wilson BC (2003) "Bioluminescence monitoring of photodynamic therapy response of rat gliosarcoma in vitro and in vivo" *Proc. SPIE*, Vol. 4952 p76-81.
5. Bogaards A, Varma A, Lilge L, Muller PJ, Wilson BC (2003) "Fluorescence-guided resection of intracranial VX2 tumor in a preclinical model using 5-aminolevulinic acid (ALA): preliminary results" *Proc. SPIE*, Vol. 4952 p91-96.
6. Muller PJ, Wilson BC, Lilge L, Varma A, Bogaards A, Fullagar T, Fenstermaker R, Selker R, Abrams J (2003) "Clinical studies of photodynamic therapy for malignant brain tumors: facial nerve palsy after temporal fossa photoillumination" *Proc. SPIE*, Vol. 4952 p97-103.
7. Bisland SK, Lothar L, Lin A, Bogaards A, Wilson BC (2003) "Metronomic photodynamic therapy (mPDT) -- headlights to lead the way forward: technical feasibility and rationale in brain tumor" *Proc. SPIE*, Vol. 5260 p342-351.
8. Burch S, Bisland SK, Siewerdsen J, Bogaards A, Moseley D, Yee A, Finkelstein J, Wilson BC (2004) "Photodynamic therapy for the treatment of metastatic lesions in bone: studies in rat and porcine models" *Proc. SPIE*, Vol. 5315 p76-87.
9. Weersink RA, Bogaards A, Gertner M, Davidson SR, Zhang K, Netchev G, Trachtenberg J, Wilson BC (2004) "Optical delivery and monitoring of photodynamic therapy of prostate cancer" *Proc. SPIE*, Vol. 5578, p117-127.
10. Weersink RA, Bogaards A, Gertner M, Davidson SR, Zhang K, Netchev G, Trachtenberg J, Wilson BC (2005) "Techniques for delivery and monitoring of TOOKAD(WST09)-mediated photodynamic therapy of the prostate: clinical experience and practicalities" *Proc. SPIE*, Vol. 5689, p112-122.

Conference Presentations

1. Bogaards A, Jongen AJ, Dekker E, van den Akker JH, Sterenborg HJCM “Design and performance of a real-time double-ratio fluorescence imaging system for the detection of early cancers” SPIE Photonics West, Jan 2000, San Jose, California, USA, Oral presentation.
2. Bogaards A, Aalders MC, Zeyl CC, de Blok S, Dannecker C, Hillemanns P, Stepp H, Sterenborg HJCM (2002) “Localization and staging of cervical intraepithelial neoplasia using double ratio fluorescence imaging. EUROPTO, July 2000, Amsterdam, The Netherlands, Oral presentation
3. Bogaards A, Varma A, Collens SP, Lin A, Giles A, Yang VX, Bilbao JM, Lilge L, Muller PJ, Wilson BC. “Increased brain tumor resection using fluorescence image guidance in a preclinical model: preliminary results” OPTO Canada 2002, May 2002, Ottawa, Ontario, Canada. Oral presentation.
4. Bogaards A, Varma A, Collens SP, Lin A, Giles A, Yang VX, Bilbao JM, Lilge L, Muller PJ, Wilson BC. “Increased brain tumor resection using fluorescence image guidance in a preclinical model: preliminary results” Gordon Research Conference on Lasers in Medicine and Biology, July 2002, New Hampshire, USA. Poster Presentation.
5. Bogaards A, Aalders MC, Zeyl CC, de Blok S, Dannecker C, Hillemanns P, Stepp H, Sterenborg HJCM (2002) “Localization and staging of cervical intraepithelial neoplasia using double ratio fluorescence imaging.” Gordon Research Conference on Lasers in Medicine and Biology, July 2002, New Hampshire, USA. Poster Presentation.
6. Bogaards A, Varma A, Zhang K, Zach D, Bisland SK, Moriyama EH, Lilge L, Muller PJ and Wilson BC “Fluorescence image-guided brain tumour resection with adjuvant metronomic photodynamic therapy in a preclinical model: preliminary results” SPIE Photonics North, May 2003, Montreal, Canada. Oral presentation
7. Bogaards A, Varma A, Zhang K, Zach D, Bisland SK, Moriyama EH, Lilge L, Muller PJ and Wilson BC “Fluorescence image-guided brain tumour resection with adjuvant metronomic photodynamic therapy in a preclinical model: preliminary results” European Society for Photobiology (ESP) 10th Annual Meeting, September 2003, Vienna, Austria. Poster presentation.
8. Bogaards A, Gertner MR, Weersink RA, Davidson S, Haider MA, McCluskey SA, Aprikian AG, Elhilali MM, Trachtenberg J and Wilson BC “Photodynamic Therapy with Tookad (WST09) for Recurrent Prostate Cancer: Initial results of a Phase I/II trial in 34 patients” Gordon Research Conference on Lasers in Medicine and Biology, July 2004, New Hampshire, USA. Poster Presentation.
9. Bogaards A, Varma A, Zhang K, Zach D, Bisland SK, Moriyama EH, Lilge L, Muller PJ and Wilson BC “Preclinical feasibility of metronomic photodynamic therapy using aminolevulinic acid induced protoporphyrin IX in a rabbit brain tumor model”, 10th World Congress of the International Photodynamic Association IPA 2005, Munich, Germany, Poster presentation P03.06.
10. Bogaards A, Sterenborg HJCM, Wilson BC “*In vivo* molecular optical imaging of fluorescent probes: an evaluation of steady-state methods for image artifact correction and image quantification” SPIE Photonics North, September 2005, Toronto, Ontario, Canada, Oral presentation.

Awards / Honours

- Canadian Back Institute Award, 2003 Kennedy Visiting Professorship Day, Division of Orthopaedic Surgery, University of Toronto "PDT for the treatment of spinal metastasis; preclinical study" Burch S, Bisland SK, Bogaards A, Whyne CM, Yang B, Yee AJM, Finkelstein J, Wilson BC. 2003.
- Best Paper Award: "Evaluation of spinal metastases in a preclinical rat model of human breast carcinoma" Burch S, Bisland SK, Bogaards A, Whyne CM, Yang B, Yee AJM, Finkelstein J, Wilson BC. International Society for the Study of the Lumbar Spine, Annual Meeting (Medtronic Sofamor Danek), Porto, Portugal, May 30 to June 5, 2004.
- Best Paper Award: "Use of photodynamic therapy to treat vertebral metastases in rat and porcine models" University Health Network Research Day. Burch S, Bisland SK, Bogaards A, Whyne CM, Yang B, Yee AJM, Finkelstein J, Wilson BC. Toronto, Ontario, Canada, October 2004.
- Gordon Research Conference - Lasers in Medicine and Biology: Student Poster Award, Value: \$500 "Photodynamic Therapy with Tookad (WST09) for Recurrent Prostate Cancer: Initial results of a Phase I/II trial in 34 patients" Bogaards A, Gertner MR, Weersink RA, Davidson S, Haider MA, McCluskey SA, Aprikian AG, Elhilali MM, Trachtenberg J and Wilson BC, New Hampshire, USA, July 2004.

Acknowledgements / Dankwoord

As they say, life is not about the destination, but about the journey. Well, let me tell you, this turned out to be quite the journey. Along the way I was fortunate to meet and work with many wonderful people with great minds. Your surroundings proved to be fertile grounds that allowed me to learn and grow.

Let me begin with the two key persons in this. Assoc.Prof.Dr.Ir. H.J.C.M. Sterenborg and Prof.Dr. B.C. Wilson. Both of you have given me chance and opportunity without any reason to do so. Dick, you guided me over the years and in doing so you were always fair, always critical and never compromised quality. Importantly, I could always depend on you no matter the distance between us. Integrity is one of the essential things I learned from you. Brian, scientifically you gave me the freedom to do anything I wanted to do, and, you allowed me to make mistakes. This hands-off approach is perhaps the most important thing I learned from you as it quickly made me learn and become independent. Dick and Brian, I thoroughly enjoyed our discussions, working with you and getting to know you. Hereby, I would like to sincerely thank both of you.

Drs. AJL. Jongen. Armand, thank you for continuing to be involved and for dedicating evenings and weekends, even after you left.

Dr.ing. MCG Aalders. Maurice, I have good memories of you and I driving a home build prototype through Europe, in a minivan, to conduct a clinical pilot study, thank you.

Dr. A. Varma. Abhay, I enjoyed working with you and would like to thank you for all your insights in neurosurgery and for the days you sacrificed towards our pre-clinical studies.

Dr. PJ. Muller. Paul, it was very interesting to discuss and prepare grant applications with you, I found your continuous efforts admirable. It was my pleasure to work with you.

Prof.Dr. J. Trachtenberg. John, your never ending enthusiasm is contagious. I found it very refreshing to hear a surgeon's perspective. Working with you was a pleasure.

Assoc.prof.Dr. L. Lilge. Lothar, your advice often helped to re-focus my efforts whenever I was struggling with a manuscript. Thank you for being a mentor and a friend.

Drs. K. Menzies and Drs. R.L. DaCosta. Keir and Ralph, I enjoyed our visits to the 'library', even during late hours and I appreciate the friendship that evolved.

To the entire groups of Dr. Sterenborg and Dr. Wilson and in particular: Dominique, Robert, Riëtte, Angelique, Diana, Arjen, David, Kristina, George, Kai, Anoja, Annie, Robert, Mark(x3), Eduardo, Paul and Augusto. It was my pleasure working with you and getting to know you. I look forward to continuing to see you at different conferences.

There are numerous other people I met and worked with whom are not specifically stated here. Nevertheless, I appreciate your efforts and I would like to thank all of you.

This journey would have been impossible without the strong support from the 'base-camp' as I would like to call it. Let me thank our families whom have been and continue to be there for us, for which I am very grateful. Also, I want to thank all our friends for their ongoing support which means a lot to me.

Last but not least, my dearest Yons, over the years of this PhD research you were my girlfriend, fiancée, and now my wife and the mother of our two wonderful children, Tim and Eva. From the bottom of my heart: Thank you, for staying by my side throughout these years no matter what, for always being supportive of what I do and for being the sunshine in my life.

Thank you.

Arjen